THERMAL EFFECTS ON SKEWED HIGHWAY BRIDGES INCLUDING BEARING ORIENTATION

Prepared for

American Iron and Steel Institute

Troy T. Tindal

and

Chai H. Yoo

Highway Research Center
Auburn University
Auburn University, Alabama

May 1998

Acknowledgments

The investigation which led to the results presented herein was supported jointly through fellowship from the American Iron and Steel Institute and by the Highway Research Center at Auburn University.

Disclaimer

EXECUTIVE SUMMARY

An investigation is conducted to characterize and quantify external effects in composite steel highway bridges under thermal loading, the primary objectives being: 1.) to evaluate the relative influences of geometric parameters on the resulting displacements and restraint forces that develop at the bearings through parametric studies, 2.) to compare the performance of the traditional method of bearing orientation and improved radial schemes of bearing orientation, 3.) to develop empirical equations to predict bearing displacements and restraint forces likely to occur under extreme environmental conditions, and 4.) to provide sample data for a comparison of the thermal responses of concrete bridges to those of similar steel bridges.

To meet the stated objectives, the basic approach taken is to study the response of finite element models of hypothetical bridges subjected to thermal loading. A literature review is conducted to examine the methods and findings of previous researches. An overview of thermal and thermoelastic analysis as well as current design code provisions are also included. Based on the results of the literature review, a simple but realistic thermal loading is developed for extreme winter and summer conditions. Three cases of bearing orientation, representative of design practice, are adopted. Parametric studies are then conducted. Hypothetical bridges are designed for a range of different span lengths, section depths, widths, and skews. The analysis is conducted using MSC/NASTRAN, a general-purpose three-dimensional finite element code. Finite element models of 121 different bridge configurations are prepared, and each bridge model is tested under all three constraint cases and both winter and summer thermal loading. Variations in structural response with each parameter are plotted, and the relative influence of each parameter is discussed. Design equations to predict the observed displacements and restraint forces at the bearings are then developed by a systematic regression procedure. The applicability of these proposed design equations is demonstrated by example. A brief study is conducted to compare structural responses of concrete and steel bridges.

Skew is determined to exert a great influence on both displacement and restraint force occurring at the bridge bearings. For bridges with sharp skews, the traditional method of bearing orientation may result in bearing forces 4 to 5 times those which would occur for one of the radial bearing orientations. Greater bearing displacements occur for longer span lengths, sharper skews, and greater widths. Greater bearing forces occur for shorter span lengths, greater widths, and shallower sections. As structural response is basically linear with respect to all other parameters besides skew angles, the decision is made to linearize the effect of skew angles rather than to use exponential, hyperbolic, and polynomial terms in the regression function. This is done by employing *ψ-functions*, functions of the skew angle, rather than the skew angle itself as a parameter. These are chosen so that structural response plots linearly against the ψ-function for a particular constraint case. Very strong correlation is achieved through this approach. Root mean square errors for the design equations are within 5% for displacements and 10% for restraint forces. Comparison with concrete bridges reveals that displacements may well be approximated as 75% of those for a similar steel bridge. Bearing forces are consistently higher for concrete bridges, particularly for the radial constraint cases, and cannot be approximated by a constant multiplier.

TABLE OF CONTENTS

CHAPTER 6

CHAPTER 7

CHAPTER 8

APPENDIX A

APPENDIX B

APPENDIX C

APPENDIX D1

APPENDIX D2

LIST OF TABLES

LIST OF FIGURES

CHAPTER 1

INTRODUCTION

1.1 Problem Statement

Highway bridges have traditionally been designed for movement in the longitudinal direction only, as calculated by the elementary mechanics of materials formula $\delta=\alpha L\Delta T$. No allowance is made for the restraint forces which develop at the bearings, under the assumption that they are small enough to be neglected, or that they will be accommodated by restraint of the structure and elastic deformation. This usually works well for straight bridges which run perpendicular across their supports and have small width to length ratios; however, as bridges become wider, or more sharply skewed, this simplified method gives results which are increasingly in error with movements and restraint forces determined by field observations, experimental studies, and more sophisticated analysis. With the increased use of skewed bridge configurations, more recently the trend has become to use a radial bearing alignment for wide and sharply skewed bridges, as these bridges are known to have problems with bearing devices for the traditional method of bearing alignment.

Problems with in-service bridges attributed to thermal effects include spalled concrete around the bearings at the supports, bent and pulled-out anchor bolts, and locked expansion joints due to an uneven gap opening across the width of the bridge. This observed damage to bridge structures suggests that thermal effects deserve more attention in the design process. However, due to the lack of a rational design procedure for thermal movements and restraint forces, an engineer cannot be certain that the structure which he has designed will perform well in service. Consequently, many uneconomical structures result, either from higher initial costs of over design, or more commonly, from higher maintenance costs due to unexpected thermal response.

1.2 Objectives of Research

The theory that describes temperature variation and the resulting movements and stresses in elastic bodies is well developed. Very detailed analyses are possible, incorporating complex geometric configurations and support conditions, as well as any combination of meteorological effects through computer implementation of sophisticated numerical solution techniques. Thereby, structural response to thermal loadings may be determined very accurately, although at a considerable expenditure of time, effort, and computing resources. The purpose of this research is to generalize thermal behavior of composite steel bridges through such rigorous analysis. The primary objectives are as follows:

1.) To evaluate the relative influences of geometric parameters on the resulting displacements and restraint forces that develop at the bearings through parametric studies

2.) To compare the performance of the traditional method of bearing orientation and improved radial schemes of bearing orientation.

3.) To develop empirical equations to predict bearing displacements and restraint forces likely to occur under extreme environmental conditions

4.) To provide sample data for a comparison of the thermal responses of concrete bridges to those of similar steel bridges.

1.3 Research Approach

To meet the stated objectives, the basic approach taken is to study the response of finite element models of hypothetical bridges subjected to thermal loading. The analysis is conducted using MSC/NASTRAN, a general-purpose three-dimensional finite element code. Finite element models of 121 different bridge configurations are tested, and sample results are plotted versus each geometric parameter. A regression analysis is then performed to reduce the finite element data to a set of design equations to predict maximum values of displacement and restraint force at the bridge bearings. Finally, concrete bridge models are prepared and analyzed in the same manner as the steel bridge models for 20 different configurations. Response data obtained from these model runs are compared to expected results for equivalent steel bridges, as determined by the proposed design equations.

CHAPTER 2

LITERATURE REVIEW

2.1 General

As bridge design became more refined, and more complex structures were constructed, the need for better understanding of thermal effects became increasingly evident. In February of 1960, an editorial in the Engineering News Record[27] called for more research in this area. The main issues addressed included:

1.) Thermal effects were responsible for much of the observed damage to bridge structures.

2.) Thermal strains may have values comparable to dead and live load strains.

3.) In some cases, it may be more economical to design a structure to resist thermal strains rather than accommodate them.

Since 1960, thermal effects have been the subject of many researches. The most notable of these are summarized in this chapter, organized by methodology. Within each section, the studies are presented in chronological order.

2.2 Experimental Studies

Zuk[32] pioneered the early research into thermal effects on bridges in the United States. In 1961, he published a rigorous derivation of thermoelastic stresses and deformations of statically determinate composite bridges due to linear temperature gradients. By his method, the slab and beam were initially considered separate and free to deform independently. Strain expressions were derived by elastic theory. To restore composite action interface shears and couples were introduced, and the resulting strains superimposed with the original thermal strains. The magnitudes of the interface forces were then determined from conditions of equal strain and radius of curvature for the beam and the slab at the interface. Actual stresses and deformations could then be established by elementary beam theory. This work was later extended by Zuk[33] to handle temperature gradients as an arbitrary function of depth, and by Berwanger[4] to include the presence of reinforcing bars in the slab.

Zuk[33] conducted a later study with a twofold purpose: to develop empirical equations to predict bridge temperatures and to examine the validity of his theoretical equations for thermal stresses and deformations through experimentation. To obtain data on actual field conditions of a composite steel bridge, the Hardware River Bridge near Charlottesville was instrumented and studied for a year. Twenty-two thermocouples were placed in various locations throughout the bridge. These were wired to a 24-point recorder which automatically scanned and recorded temperatures at all points once an hour. Periodic strain readings were taken manually in the beam and slab at midspan using a 10" strain gage, compensated by an invarient invar bar. The structure was two years old when testing initiated, so essentially all shrinkage had already taken place. All strain readings were taken under dead load and constant moisture conditions.

From the measured temperatures, Zuk developed coefficients for an equation proposed by Barber.[3] On the basis of assuming a sinusoidal effective daily temperature cycle and average values for secondary parameters, the maximum surface temperature in degrees Fahrenheit for normal concrete decks can be approximated by

$$T_m = T_a + 0.018L + 0.667(0.50T_r + 0.054L) \tag{2.1}$$

where T_a = average daily air temperature, T_r = daily range in air temperature, and L = solar radiation received on a horizontal surface (cal/sq cm/day). The corresponding equation for a bridge deck covered with a thin bitumen topping is

$$T_m = T_a + 0.027L + 0.65(0.50T_r + 0.081L) \tag{2.2}$$

The above equations were developed for the Middle Atlantic States, but a method is available to adjust the constants for other regions.[3] The value of L (langleys of solar radiation) may be determined from U.S. Weather Bureau maps. The maximum temperature differential through the slab of a steel-girder bridge was given as

$$\Delta T_m = T_m - T_a \lambda T_r \tag{2.3}$$

where λ = lag factor, varying from about 1/4 in the summer to about 1/2 in the winter. Equation 2.3 gave results within close agreement of measured values.

Complications arose during the test which rendered attempts at reconciling the theoretical and experimentally determined stresses and deformations futile. The two reasons cited for the divergent results were an observed interface slip and appreciable end restraint at the levels of the slab and the bearing. It was determined that a compressive stress of 689 psi across the end of the slab and a bearing force of 15 kips must exist in the actual bridge structure to explain the measured strains. While Zuk was unable to incorporate the effects of creep, slip, and plasticity into his theory, he suggested that it could nevertheless be safely applied to calculate thermal stresses, as the unknown effects mentioned tend to reduce the severity of the induced stresses.

Churchward and Sokal[6] developed a mathematical model to predict temperature distributions in concrete bridges in 1981. The model was based on measured data from an experimental box girder bridge. The bridge was instrumented with thermocouples and measurements were taken continuously for three years. Environmental parameters including ambient temperatures, solar radiation, wind velocity, and hours of sunshine were also recorded.

The temperature profile was composed of two parts in the model. Previous studies indicated that the temperature distribution is negligibly affected by daily changes in atmospheric conditions, and is also independent of depth below approximately 3.28' (1m) depth. This was defined as the base temperature *BT*. The total temperature profile was then the superposition of the differential component *DT(y)* onto the base temperature, where *y* is position along the depth of the section. Good correlation with measured data was obtained with the following relationships:

$$BT = 1.14\,AMAX$$
$$DT(y) = \frac{DTMAX}{10.82\,y + 1} \tag{2.4}$$

where *AMAX* = maximum ambient temperature, *DTMAX* = differential temperature at the top of the section, both in degrees Celsius, and *y* is a position coordinate measured downward from the top of the section in meters. More complex expressions were given for *BT* involving the ambient temperature history as well as expressions for *DTMAX* as a function of solar radiation.

Emanuel and Lewis[10] investigated thermal behavior of integral abutment bridges in 1981. Their objective was to develop correlative experimental-theoretical data on the combined effect of approach slab thrust and thermal loading. This was one of several studies aimed at examining the feasibility of developing rational design criteria for bridges with semi-integral end bents. The scaled model bridge and instrumentation were as follows: Each span was 15' long by 45" wide. The superstructure was composed of three M6X4.4 steel stringers, twenty C4X5.4 diaphragms, and a 1 1/2" thick reinforced concrete deck. Shear studs were provided only in the positive moment zone. The abutment assembly consisted of a 6" X 1/2" steel plate pile cap welded to three 5" X 1/2" X 72" steel bar piles buried 66" in a sandbox of uniform density. The abutment assembly simulated an integral stub abutment with flexible piling. The center pier was constructed similarly of 2" pipe sections. Four 1 1/4" threaded steel tie-rods were used to simulate approach slab thrust on the abutments. The tie-rods were anchored to the abutment caps and pretensioned to a specified force before each load sequence. Infrared reflector heat lamps were used to apply thermal loading to the structure. These were placed in staggered rows 20" above the structure in accordance with the manufactor's recommendations for uniform radiation. Thermistors and electrical resistance strain gages were mounted on the structure in various locations to measure temperatures and strains. Dial gages were used to measure longitudinal deck expansion and vertical deflections at the midspan points.

For each test cycle, the tie-rods (when used) were pretensioned to counteract expected thermal elongation during the test, and all strain gages and dial gages were zeroed. Initial thermistor readings were recorded as reference temperatures. The lab was completely sealed and then the lamps were turned on and adjusted to produce a uniform heat flux on the deck. After approximately ten hours, steady state conditions would be achieved, and all instrument readings were hand recorded. Then the lamps were turned off and instrument readings were repeated after the structure cooled.

The test results fell within a narrow band. The structure did not experience any unsymmetrical or nonreversible movements. Measured deflections were within 15% of theoretical values. With the tie-rods in place, the compressive stress in at the top of the deck ranged from 1.7 to 3.5 times the no-tie-rod condition. The compressive stress in the top of the stringer increased by a factor of approximately 1.4, and the tensile stress at the bottom of the stringer decreased by a factor of approximately 2.3. From these results, it was concluded that the integral abutments have the effect of imposing significant flexural stresses as well as large axial compressive stresses. It was determined that the theoretical procedure was adequate for prediction of abutment-thermal interaction for composite bridges.

Hoffman, McClure, and West[12] conducted an experimental study of a test bridge at the Pennsylvania Transportation Research Facility in 1983. The bridge consisted of two curved, superelevated, prestressed box girders, each consisting of 17 segments. The bridge was instrumented with thermocouples across the bridge section at several locations. Temperatures and vertical deflections at midspan were recorded over 18 daily cycles (midnight to midnight) over a one-year period. Meteorological data was obtained from the Meteorological Observatory at The Pennsylvania State University, five miles from the test site.

An initial investigation found no temperature variation along the length. Curvature was therefore taken to be constant, and was calculated from the measured deflections at midspan. Theoretical curvatures were also calculated from the thermocouple readings, and were found to compare closely to the experimental values. The most extreme measured temperature gradients occurred at 4:00 P.M. These showed rather good agreement with the gradient specified in the New Zealand Specifications.

Numerical examples compared curvatures and stresses induced by modifications of two standard design temperature gradients of vastly different complexity. The New

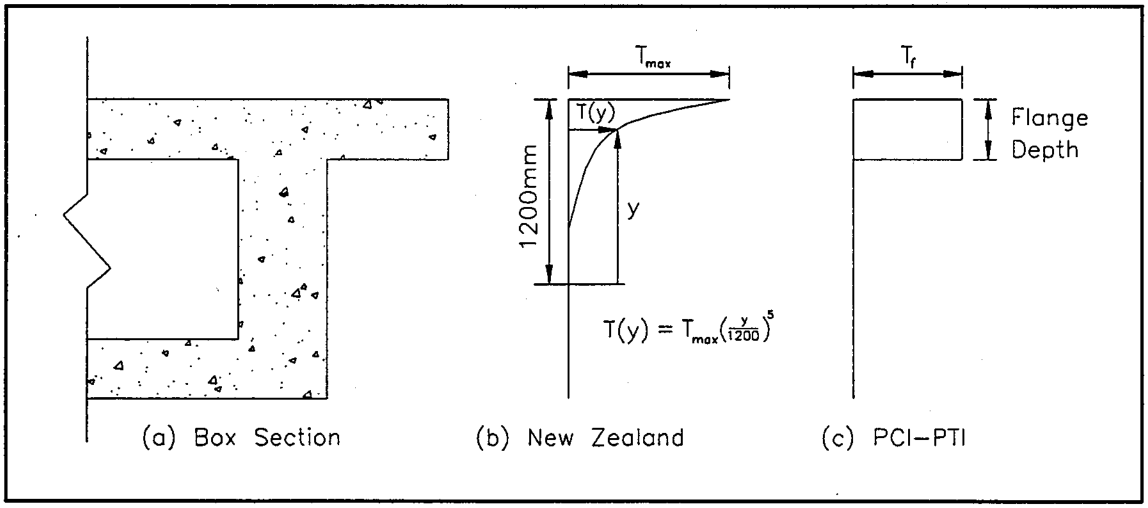

(a) Box Section (b) New Zealand (c) PCI–PTI

Figure 2.1: Modified New Zealand and PCI-PTI Temperature Gradients

Zealand Ministry of Works Specifications prescribes a fifth-order distribution through the upper portion of the section. The *Precast Segmental Box Girder Bridge Manual*,[25] published jointly by the Prestressed Concrete Institute and the Post-Tensioning Institute, prescribes a constant temperature difference which extends through the depth of the flange. These are shown in Figure 2.1. For the New Zealand gradient, T_{max} was taken as 51 °F to conform with field observations. Resulting axial strain, curvature, and stresses were calculated for a simplified section of the test bridge. The value of T_f for the PCI-PTI gradient was taken as 35.8 °F, as this resulted in an axial strain equal to that of the New Zealand gradient, and curvature and stresses were calculated. While curvatures calculated for the two gradients were approximately equal, the stress patterns were markedly different.

2.3 Field Observational Studies

Steward[28] conducted a field study of bridge deck expansion joint movements in 1969. Eighty bridges throughout California were monitored over a three-year period. Expansion joint movements were recorded on an aluminum tube by a sharp steel scribe. These were attached to the barrier rail on each side of an expansion joint. As the joint moved, the scribe traced a mark on the tube. The mark was then measured using a graduated scale with 0.01" divisions and a 10X magnifying glass.

Each of the bridges was considered to be located in one of four climatic regions of California. The average movement per unit length for steel and concrete bridges is given in Table 2.1. The movements observed often varied considerably for different expansion joints on the same bridge. Concrete box girder bridges experienced least

Table 2.1: Steward's Average Expansion Joint Movements Per Unit Length

Region	Steel	Concrete
Coast	0.00041	0.00027
Valley	0.00042	0.00034
Mountain	0.00060	0.00046
Desert	0.00048	0.00041

movements due to temperature fluctuation. This was attributed to the insulating effect of the air trapped inside the box. The types of expansion bearings and the degree of skew were determined to have no significant effect on bridge deck expansion joint movements. Based on the greatest movements and corresponding temperature ranges at each location, average apparent thermal coefficients of expansion of 0.0000065/°F and 0.0000053/°F were recommended for steel and concrete superstructures, respectively.

In 1991, Pentas et al.[22] conducted an investigation into bridge temperatures and temperature distributions of the east approach of US-190 over the Atchafalaya River at Krotz Springs, Louisiana. The spans monitored in the study were constructed of a 7 1/2" thick cast-in-place concrete slab composite with AASHTO Type IV prestressed concrete girders. Rocker bearings and expansion joints were provided at four locations across the ten spans. The bridge was instrumented with four thermocouple arrays. Each array consisted of six thermocouples through the depth of the bridge. These were monitored once per month for an alternating 12- or 24-hour period for two years.

Maximum and minimum values of slab and girder temperature as well as ambient temperature were plotted versus time. The maximum average girder temperature was found to closely follow the ambient temperature, though with a phase shift. The maximum average slab temperatures followed a similar trend, but at higher temperatures solar radiation was found to magnify the slab temperatures in a somewhat linear manner. The following relationship was suggested to predict maximum average slab temperatures T_s from ambient temperature T_a:

$$\begin{aligned} T_s &= T_a && \text{for } T_a \leq 70°F \\ T_s &= 2T_a - 70 && \text{for } T_a > 70°F \end{aligned} \tag{2.5}$$

Pentas also developed a vertical temperature profile based on his observations. His goal was to propose a temperature gradient that was representative of actual measured data, but that was simpler than those proposed by others, and would be easy to use as thermal loading for structural analysis. Temperatures at three points through the depth of the section are given by the following equations:

$$\begin{aligned} T_1 &= 0.095 + 0.832T_a + 0.004T_a^2 && \textit{top of deck} \\ T_2 &= 6.630 + 0.648T_a + 0.005T_a^2 && \textit{deck-girder junction} \\ T_3 &= 23.88 + 0.206T_a + 0.006T_a^2 && \textit{mid-depth of girder} \end{aligned} \tag{2.6}$$

The temperature profile is linear between these points and constant below the center of the girder. This model temperature gradient was developed for the Atchafalaya River Bridge of AASHTO Type IV girders, and yields results within 5 to 10% for similar construction of AASHTO Types II and III as well.

A second study by Pentas[23] sought to quantify longitudinal movements in the same bridge. The bridge was instrumented with LVDTs and optical devices. LVDTs were mounted at the end of each girder above and below the neutral axis. A total station theodolite was used to measure the bent sway at expansion joint locations. LVDT readings were recorded once per month along with the thermocouple readings. As the LVDTs were not installed until nine months after the bridge deck was poured, it was assumed that creep and shrinkage effects had dissipated. Therefore, movements observed were caused by thermal effects only. Field monitoring continued through one year of exposure to normal traffic.

While there was a general seasonal repetitiveness of joint movements associated with seasonal temperature trends, the bridge sections exhibited unsymmetrical and nonreversible joint movements. As expected, maximum joint closure occurred on the warmer days of May and June, and maximum joint opening occurred on the colder days of December through February. Maximum movements occurred on different days for each joint, and had different magnitudes as well. Although the bridge sections did not return to their initial positions as temperatures rose and fell, no rigid body translation was detected over time. Comparison of movements observed before and after the bridge was opened to traffic did not indicate any deviation due to the traffic loads.

2.4 Analytical Studies

Hunt and Cooke[13] solved the heat conduction and thermoelastic problems analytically in 1975. One-dimensional finite difference heat conduction equations were developed for a general cross-section with a change in thermal properties somewhere within the depth. The Crank-Nicolson scheme was employed to approximate the temperatures at internal nodes, which has second-order accuracy for incremental steps through the depth as well as through time and is unconditionally stable. The analytical heat conduction procedure was verified through comparison with available experimental data from a study of a concrete box girder bridge. The best comparison occurred at the interior of the section. Poorer comparison occurred near the outer edges of the slab. This was believed to have resulted from the significant transverse heat flow in this zone, which was not accounted for in the one-dimensional analysis. The authors stated that the comparison was overall good and quite adequate for most design purposes.

They also developed a rigorous thermoelastic procedure to calculate thermal stresses. A plain strain solution using Airy's stress function was employed. Cases were solved for free and fixed end conditions. A numerical example was given for a concrete box section. Stress results obtained from this rigorous approach were compared to those obtained from one-dimensional beam theory. Good agreement was observed through the webs, but the beam theory underestimated longitudinal normal stress throughout much of the top flange. Significant transverse normal stresses were also observed from the rigorous solution, which were not accounted for at all by the beam theory approach.

In 1975, Radolli and Green[26] examined thermal effects in concrete bridges. A series of temperature distributions corresponding to maximum temperature gradient was calculated for rectangular sections of varying depths. The calculations were based on a simple iterative finite difference procedure. Maximum values of solar radiation observed in Toronto, Ontario for May through July of 1973 were used in the analysis. The resulting temperature gradients reflected a definite pattern with increasing depth. To evaluate structural response several rectangular, T-, and I-sections were then tested under temperature gradients characteristic of their different depths. Curvature and eigenstresses (self-equilibrating stresses) were calculated based on beam theory.

From the analysis, shallower sections were found to exhibit larger curvatures and higher mean temperatures under given atmospheric conditions. For deeper sections, the moderating effect of the larger semi-insulated interior portion resulted in higher eigenstresses. Surface compressive stresses of 300 psi were calculated for a typical continuous structure under summer conditions. Stresses under winter conditions were approximately -0.70 to -0.80 of summer values.

In 1977, Will, Johnson, and Matlock[31] of the Center for Highway Research at Austin, Texas developed two finite element programs for predicting bridge structural response under thermal loading. The first was a heat conduction program. It employed two-dimensional finite elements to calculate temperature distribution over the cross-section of the bridge. Rather than using prescribed heat flux as boundary conditions (estimated from solar radiation, wind speed, and air temperature), surface temperatures were input directly into the program. The second program was a linear static stress analysis code. It used a three-dimensional assemblage of two-dimensional finite elements to model the structure, and was capable of modeling skewed supports. To verify the analytical results, they conducted a brief study of field movements of two bridges— a three-span continuous, skewed, post-tensioned concrete bridge, and a two-span continuous pedestrian overcrossing with pretensioned beams. Surface temperatures were measured at selected times and input into the heat conduction program. The internal temperature distribution determined by the heat conduction analysis was then input into the stress analysis program, and analytical curvatures were calculated. These compared favorably with slope curvatures determined with a mechanical inclinometer.

Later, Thepchatri, Johnson, and Matlock[29] conducted a series of analytical studies using the aforementioned programs. In these studies, instead of specifying temperatures directly in the heat conduction analysis, diurnal variations in solar radiation, air temperature, and wind speed were chosen to represent extreme winter and summer climatic conditions for the Austin area. The analytical results were again compared to available field test data to verify the calculated temperature distributions, and extremely good correlation was obtained. Having verified the analytical procedures, the researchers preceded to determine thermal effects on three bridges of different sections: a post-tensioned concrete slab bridge, a composite post-tensioned bridge, and a composite steel girder bridge.

Several general conclusions resulted from these studies conducted at the Center for Highway Research. Initial conditions were determined to be inconsequential after heat conduction analysis is conducted for three to five days. The magnitude of thermal stresses in continuous bridges lay between those in a simple span and those in a two-span bridge. The effect of prestressing on thermal stresses was insignificant. When bearing friction was included, the additional forces were small enough to be ignored.

In 1983, Elbadry and Ghali[9] developed a two-dimensional finite element program for transient heat conduction analysis. This program was called FETAB (Finite Element Thermal Analysis of Bridges). The program used two types of elements: a bilinear quadrilateral interior element, and a linear one-dimensional fictitious element to represent the boundary. Galerkin's weighted residual method was employed to calculate nodal temperatures for each time step. Time-varying environmental conditions of air temperature and solar radiation were modeled mathematically by equations with variable coefficients which were input into the program.

The FETAB program was used in a parametric study to determine the relative influence of the orientation of the bridge axis, air temperature extremes, wind speed, and geometry of the cross-section. Variation of curvature with orientation of the bridge axis was found to be insignificant in the spring and summer, but curvature increased by 44% in the winter when the bridge was rotated from East-West to North-South. Increasing the range of ambient air temperature increased the curvature, and to a greater extent the eigenstresses. Higher wind speeds resulted in smaller curvatures and much reduced eigenstresses. The solid slab, cellular slab, and box girder sections tested had nearly identical temperature profiles for equal depths. On the other hand, the temperature distribution varied greatly for different section depths.

Potgieter and Gamble[24] examined the variability of induced temperature gradients in concrete bridges across the United States in 1989. Their objective was to quantify extreme thermal loadings throughout the country, from which design criteria could be developed. A finite difference computer model was developed for one-dimensional heat analysis and verified through field measurements of the Kishwaukee River Bridge near Rockford, Illinois. Although box girder bridges were of primary emphasis in the study, which are known to exhibit transverse as well as vertical temperature gradients, the one-dimensional model was deemed adequate for the study because the interest was in overall structural response to a large number of different climatic conditions. Typical values of maximum and minimum solar radiation, dry bulb and dewpoint temperature, and mean and maximum wind speed were taken from meteorological data from 26 SOLMET stations between the years 1954 and 1972. Extreme days were selected from the months of June and July. Four different bridge sections were tested under the extreme conditions identified at all 26 stations: a 6.56' (2m) structure, a 3.28' (1m) structure, a 1.64' (0.5m), and a 3.28' (1m) structure with an air cavity.

From the heat conduction studies, it was determined that solar radiation and wind speed are the two most dominant parameters affecting thermal gradients in concrete structures. Maximum temperature gradients were obtained for the desert Southwest States. Moderate response was obtained for coastal areas.

A second objective of their study was to generalize the response of typical box girder bridges due to nonlinear temperature gradients. While the wide range of cross-sections used in practice makes it difficult to define a generalized cross-section without using several parameters, Potgieter and Gamble observed that different structures of equal depth exhibited similar responses. Thermally induced curvatures and eigenstresses were computed for 18 existing box girder bridges based on conditions at Brownsville, Texas and Phoenix, Arizona, as these locations realize the lowest and highest temperature gradients, respectively, of the 26 stations tested. The results were then fitted to cubic polynomials. For unsurfaced decks, curvature ϕ and eigenstress at the soffit f are given by the simple expressions

$$\begin{aligned} \phi_6 &= 114 - 33.3D + 3.68D^2 - 0.140D^3 \\ f_6 &= -189 + 3.27D \\ \phi_{15} &= 194 - 54.3D + 5.89D^2 - 0.219D^3 \\ f_{15} &= -304 + 7.96D \end{aligned} \tag{2.7}$$

where D = girder depth in feet, and the subscripts 6 and 15 refer to Brownsville and Phoenix (SOLMET Stations 6 and 15). The authors suggest relationships such as these be provided in the design codes.

Moorty and Roeder[18] conducted an extensive study of thermal effects on skewed and curved bridges in 1992. Heat conduction studies were conducted for typical bridges of three cross-sections: concrete box girder, concrete T-beam, and composite steel I-girder. These sections were modeled with two-dimensional finite elements, and solved using ANSYS, a general-purpose finite element code. Maximum and minimum effective bridge temperatures for each section were calculated at 11 different locations in the United States. These were compared to AASHTO specified temperature ranges. The results indicated that concrete bridges experience mean temperatures which sometimes exceed the AASHTO-recommended range, while mean temperatures for the steel bridges were well within the recommended range.

Structural analysis was conducted on several series of skewed and curved bridges in order to generalize the response to thermal loading. ANSYS was again used to solve the thermoelastic problem. The basic bridge model used in the study was a three-span continuous composite steel bridge with three equal spans. The bearings allowed motion only in the longitudinal direction of the bridge. The skew angle, length, and width were varied. Shell elements were used to model the slab, and beam elements for the girders. A temperature distribution obtained from the heat conduction analysis was applied as loading. Skew was found to totally alter the pattern of displacements, with maximum displacement along the long diagonal. Longitudinal displacement as well as axial forces in the girders increased with increasing skew. Bearing forces increased with increasing width and decreasing length. The same basic bridge model was used in the curved bridge study. Cases were considered for bearings oriented tangentially to the curvature and on a chord from the point of fixity. The structure was modeled in a similar manner, and angle of curvature (L/R), length, and width were varied. Tangential displacements were nearly the same for the two cases of bearing orientation. Bearing forces increased with increasing angle of curvature for tangential bearing orientation.

CHAPTER 3

BACKGROUND AND THEORY

3.1 Temperature Variations

Any structure exposed to the elements is continuously exchanging heat energy with its environment, and therefore experiences temperature fluctuations. Branco[5] categorized the parameters to be considered in the calculation of bridge design temperatures as follows:

- Climatic: solar radiation, air temperature, wind speed, and nebulosity
- Geographical: altitude, latitude
- Time: hour of the day, day of the year
- Geometric: geometry of cross section, bridge orientation, asphalt thickness
- Materials: thermal conductivity, density, specific heat, color

The effect of these factors is to subject the bridge to both a seasonal and a daily temperature cycle. The seasonal cycle is considered the more important of the two, and it is this temperature fluctuation which is specified in the design codes. The daily temperature cycle usually begins with a low temperature being attained just before sunrise. The sun's appearance causes a steady rise in temperature until the daily peak temperature is reached, usually in the mid-afternoon, and then the temperature drops off again. The basic daily temperature cycle can be altered by clouds which may shade the area or release some form of precipitation.

Besides the fluctuation of mean bridge temperature with time, a variety of temperature distributions are possible over the cross-section at any particular instant. A uniform temperature typically exists about an hour after sunrise, when the air temperature has remained nearly constant for several hours. The top of the deck is warmer than the rest of the bridge when the sun shines on its exposed surface. This positive temperature gradient is maximum in the mid-afternoon. A negative gradient occurs when the top surface is cooled rapidly, such as when a rain or snow storm begins or in dropping air temperature and high wind. Steel responds to temperature changes quickly because of its low specific heat and high thermal conductivity. Hence, the temperature of steel components in a bridge structure is usually uniform and equal to the air temperature. Concrete, on the other hand, has a relatively high specific heat and low thermal conductivity; thereby concrete components are susceptible to considerable temperature gradients.

Temperatures within the section may be calculated through thermal analysis. The Poisson heat flow equation which models the transient heat flow is

$$\rho C \frac{\partial T}{\partial t} = k\left(\frac{\partial^2 T}{\partial x^2} + \frac{\partial^2 T}{\partial y^2} + \frac{\partial^2 T}{\partial z^2}\right) \tag{3.1}$$

where ρ = the density of the material, C = the specific heat, and k = the thermal conductivity. T = temperature, t = time, and x, y, and z are Cartesian position coordinates. Several studies have suggested that the above equation be reduced to two dimensions for box girder bridges and one dimension for I-girder bridges.

The boundary conditions associated with Equation 3.1 account for heat transfer at the surface. Figure 3.1 illustrates the meteorological conditions which may be incorporated into the analysis through the boundary conditions. The three principal mechanisms of heat transfer are radiation, convection, and conduction. Radiation is generally considered to be the most important of the three and includes both radiation from the sun and irradiation between the structure and the environment. Conduction and convection also take place at the structure surface. However, because the heat transfer by conduction alone is small, it is difficult to assess. Therefore, it is normal to allow for heat transfer by conduction and convection by assuming a single, combined coefficient

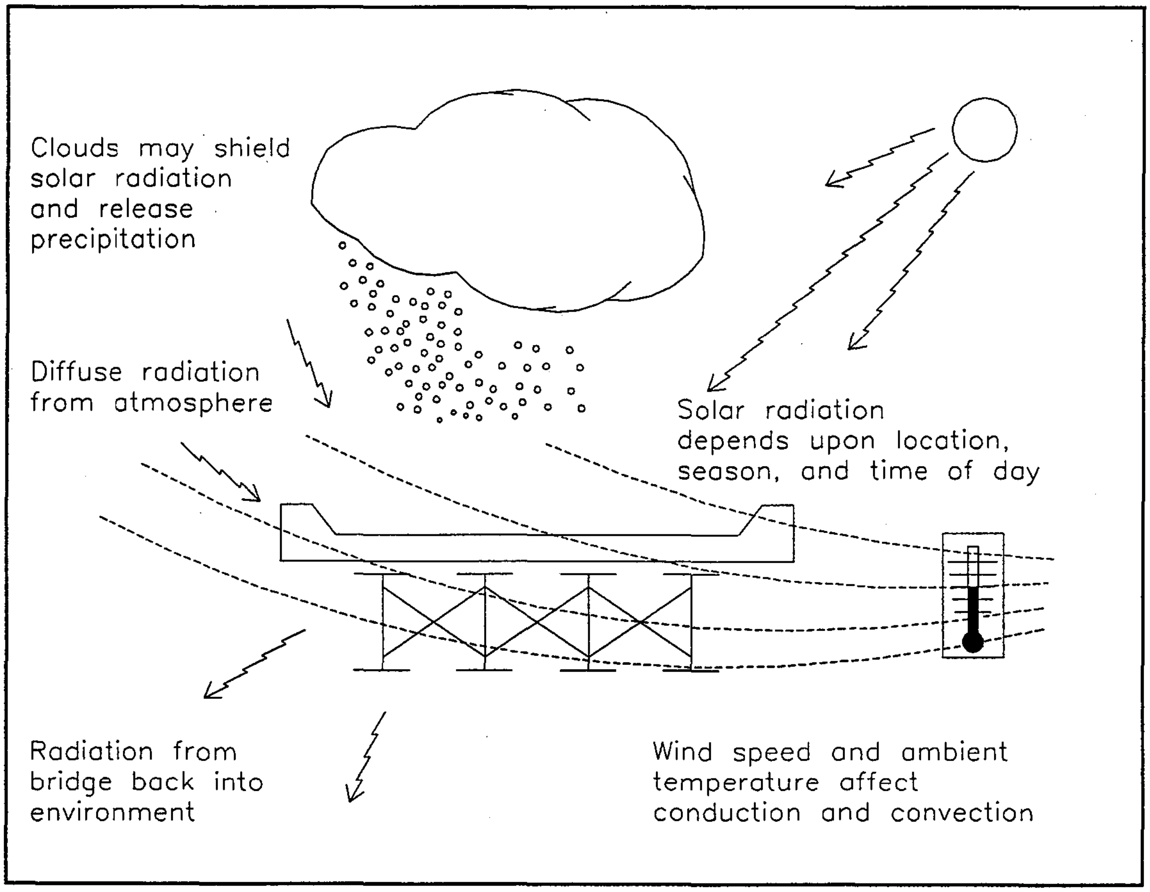

Figure 3.1: Environmental Actions on the Bridge

sensitive to wind velocity, ambient air temperature, and surface temperature. The boundary conditions may be expressed in terms of heat flux (time rate of heat transfer across the boundary) by

$$q_n = q_c + q_r + q_s \tag{3.2}$$

which states that the net outward heat flux must equal the sum of contributions from convection and conduction, irradiation, and solar radiation, respectively. Expanding each of these terms gives

$$q_n = h_c(T-T_a) + \epsilon\sigma(\overline{T^4} - \overline{T_a^4}) - \eta I_n \tag{3.3}$$

in which h_c = coefficient of convective heat transfer, ϵ = emissivity, σ = Stefan-Boltzman constant = 5.67 X 10^{-8} W/($\mathrm{m}^2 \cdot \mathrm{K}^4$), η = absorptivity, and I_n = normal component of heat flux from sun. The subscript a denotes ambient temperature, and the bars are used to distinguish absolute from relative temperatures. Combining the first two terms on the right-hand side of Equation 3.3 with a single heat transfer coefficient which accounts for the effects of conduction, convection, and irradiation reduces the expression to

$$q_n = h(T - T_a) - \eta I_n \tag{3.4}$$

where h = the aforementioned combined heat transfer coefficient, whose value at the top of the deck is given by the empirical formula

$$h = 13.5 + 3.88u \tag{3.5}$$

where u = wind speed at the bridge site in m/s. For other surfaces, the heat transfer coefficient should be taken as 0.45 of its value at the top of the deck. Further, Fourier's law of heat conduction states that the heat flux in any direction n is proportional to the temperature gradient at that point:

$$q_n = -k \frac{dT}{dn} \tag{3.6}$$

The constant of proportionality k is the thermal conductivity of the material. Combining Equation 3.3 and 3.6 gives the boundary conditions as

$$\eta I_n - h(T - T_a) + k \frac{dT}{dn} = 0 \tag{3.7}$$

Many empirical formulas are available for I_n as a sinusoidal function of time, latitude, and hours of sunlight per day, or it may be measured directly.

3.2 Structural Response to Thermal Loading

When an unrestrained homogeneous body undergoes a uniform temperature change, all points within the body move radially from the point of zero movement in proportion to their distance from this point. When there is a variation in temperature throughout the body, the warmer parts tend to expand more than the cooler parts. This thermal bending contributes a second-order effect to overall movements. If thermal deformations are even partially restrained, large forces can develop. Because neither free movement nor complete restraint conditions exist in bridge structures, a combination of both thermal stress and thermal strain generally prevails.

Because movements under temperature change are proportional to distance from the fixed point, longer or wider spans require more consideration. Thermal bending is especially important in acutely skewed or curved spans. For continuous structures, thermal bending may cause significant redistribution of support reactions in both the horizontal and vertical planes. Nonlinear temperature gradients that arise in concrete bridges can induce high tensile stresses near the top of the section that are frequently associated with deck cracking. Thus an accurate analysis of thermal effects on a bridge must include a temperature gradient through the depth of the bridge cross-section.

The general nonlinear temperature gradient through the depth of a homogenous structural member can be decomposed into three components, shown in Figure 3.2. The uniform component T_m is related to the expansion of the neutral axis of the member. The linear gradient ΔT between extreme fibers is related to curvature of the member as explained previously. The nonlinear gradient T_0 is associated with the self-equilibrating stresses, or eigenstresses, which result from the tendency for plane sections to remain

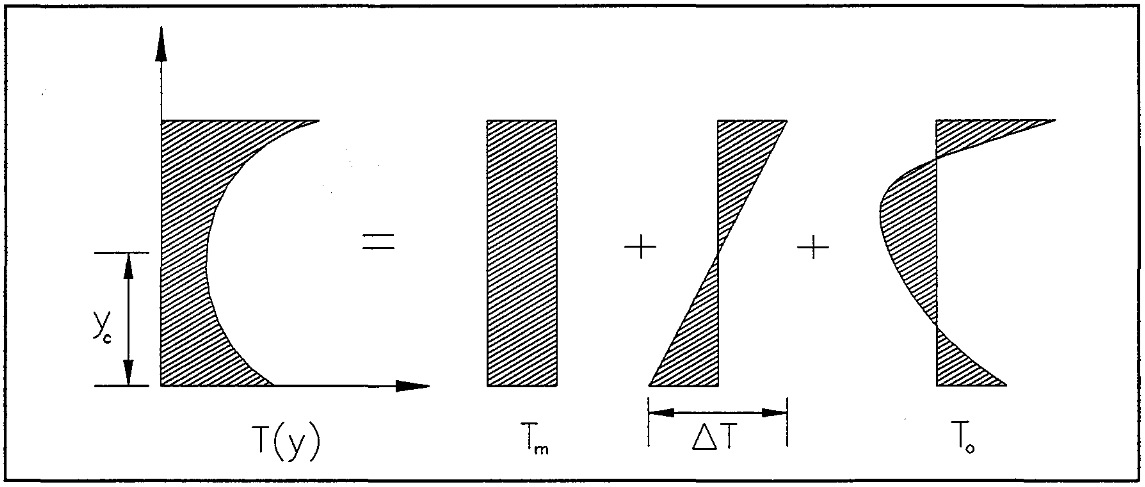

Figure 3.2: Components of the General Nonlinear Temperature Gradient

plane. The nonlinear component does not contribute to deformation, and the resulting stresses are independent of support conditions. These can be extracted from the total temperature distribution by

$$T_m = \frac{1}{A}\int T\,dA \qquad \textit{mean temperature}$$

$$\Delta T = \frac{h}{I}\int T(y-y_c)\,dA \qquad \textit{linear gradient} \tag{3.8}$$

$$T_0 = T - T_m - \frac{y}{h}\Delta T \qquad \textit{nonlinear gradient}$$

where A = area, I = moment of inertia, and h = height of the cross-section, and y_c = centroid location. The structural responses to each of the temperature components of Equation 3.8 are given by

$$\epsilon = \alpha\, T_m \qquad \textit{axial strain}$$

$$\phi = \alpha\frac{\Delta T}{h} \qquad \textit{curvature} \tag{3.9}$$

$$\sigma_0 = E\,\alpha\, T_0 \qquad \textit{self-equilibrating stresses}$$

where α = coefficient of thermal expansion and E = modulus of elasticity. For composite concrete slab on steel girder sections, these responses may be calculated directly as

$$\epsilon = \frac{1}{A}\int \alpha\, T\,dA \qquad \textit{axial strain}$$

$$\phi = \frac{1}{I}\int \alpha\, T(y-y_c)\,dA \qquad \textit{curvature} \tag{3.10}$$

$$\sigma_0 = E\left[\alpha\, T - \epsilon - \phi\,(y-y_c)\right] \qquad \textit{self-equilibrating stresses}$$

where A and I are transformed by the modular ratio. As α changes its value at the interface between the steel and the concrete, the two integrals in Equations 3.10 are actually evaluated by two separate integrations over each portion of the section.

3.3 AASHTO Provisions

The current AASHTO Design Specifications[1] prescribe a maximum range of mean temperature to calculate thermal deformation and force effects from resisting component deformation. These are given in Table 3.1. A cold climate is defined as one in which the average temperature is less than 32°F for 14 or more days per year. The difference between the extended upper or lower bound temperature from Table 3.1 and the base temperature is used in the design of bearings and deck joints.

Table 3.1: AASHTO Design Temperature Ranges

Climate	Steel / Aluminum	Concrete	Wood
Moderate	0°F to 120°F	10°F to 80°F	10°F to 75°F
Cold	-30°F to 120°F	0°F to 80°F	0°F to 75°F

AASHTO has now added a design temperature gradient, as well as procedures to calculate resulting axial expansion, flexural deformation, and internal stress. The positive temperature gradient, shown in Figure 3.3, is bilinear through the depth of the superstructure. For steel bridges, the temperature is taken to be constant below the deck. Table 3.2 specifies values for T_1 and T_2 based on thickness of asphalt wearing surface and location in one of four solar radiation zones:

1. Western States
2. Central States west of the Mississippi River plus Illinois
3. Eastern States plus Hawaii
4. Alaska

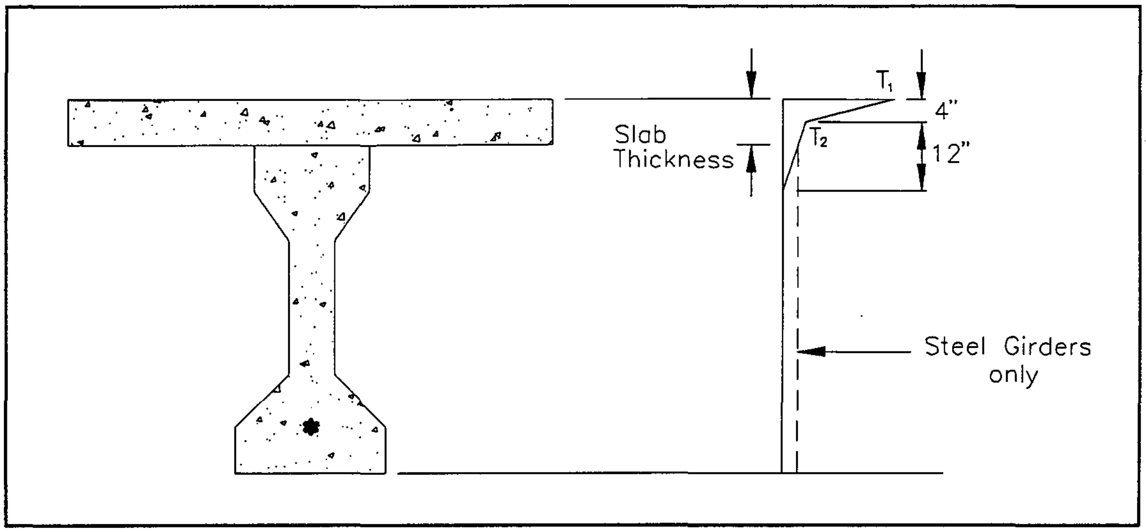

Figure 3.3: AASHTO Design Positive Vertical Temperature Gradient

where asphalt is used, T_1 is the temperature difference at the interface between the asphalt and the deck surface.

Table 3.2: Basis for AASHTO Temperature Gradients

Solar Radiation Zone	Concrete Surface		2-Inch Asphalt		4-Inch Asphalt	
	T_1 (°F)	T_2 (°F)	T_1 (°F)	T_2 (°F)	T_1 (°F)	T_2 (°F)
1	54	14	43	14	31	9
2	46	12	36	12	25	10
3	41	11	33	11	23	11
4	38	9	29	9	22	11

The design negative temperature gradient uses the same profile as the positive gradient. Values of T_1 and T_2 are taken as -0.5 of those specified in Table 3.2.

3.4 Solution by the Finite Element Method

The finite element method is employed to calculate the structural response to thermal loading. This is accomplished by a matrix implementation of the displacement method of structural analysis. The bridge structure is discretized into small elements for which stiffness properties can be closely approximated. Equilibrium equations for each element are then assembled into a structural matrix equation given by

$$\{P\} = [S]\{d\} - \{Q\} \tag{3.11}$$

where $\{P\}$ = structural nodal load vector, $[S]$ = structural stiffness matrix, $\{d\}$ = structural nodal displacement vector, and $\{Q\}$ = work-equivalent nodal load vector. The vector $\{Q\}$ accounts for the effect of loading applied to the element itself, such as surface traction, body force, initial strain or thermal expansion. It is the assemblage of work-equivalent nodal loads $\{q\}$ for each element. For thermal expansion, these are given by

$$\{q_T\} = \int_V [B]^T [C] \{\epsilon_T\}\, dV \tag{3.12}$$

where $[B]$ = strain-displacement matrix, $[C]$ = constitutive matrix, and $\{\epsilon_T\}$ = thermal strain vector. The thermal strains are equal to $\alpha\Delta T$ for normal strain components and zero for shearing strains. The integration region is the volume occupied by the element. Finite element codes have built-in routines for each element in their library to evaluate the integral given by Equation 3.12 numerically.

CHAPTER 4

BRIDGE MODELING

4.1 Hypothetical Bridge Designs

A set of hypothetical bridges was developed to study the effect of various geometric and constraint parameters on the thermal response of composite steel bridges. These bridges were the composite multi-I-girder type. Proportionality among the designs was maintained to the greatest extent possible in order to avoid variation in the response data from sources other than the control parameters manipulated in the study. A typical section and girder elevation are shown in Figures 4.1 and 4.2. Where numerical values are specified, they are standard for all designs.

Bridges were designed for the medium-span range— 80' to 180' at 20' intervals. All were simple spans. For each span length, several depths were considered between a span to depth ratio of 16 to 26. The bridges were designed in accordance with the AASHTO Standard Specifications.[2] Girders were proportioned for moment strength as non-compact sections according to section 10.50.1 *Positive Moment Sections of Composite Beams and Girders* using the HS20-44 truck loading with impact. Web plates were designed with an unsupported depth to thickness ratio of 150, so that transverse stiffeners were required only in high shear zones. Flange plate thickness was

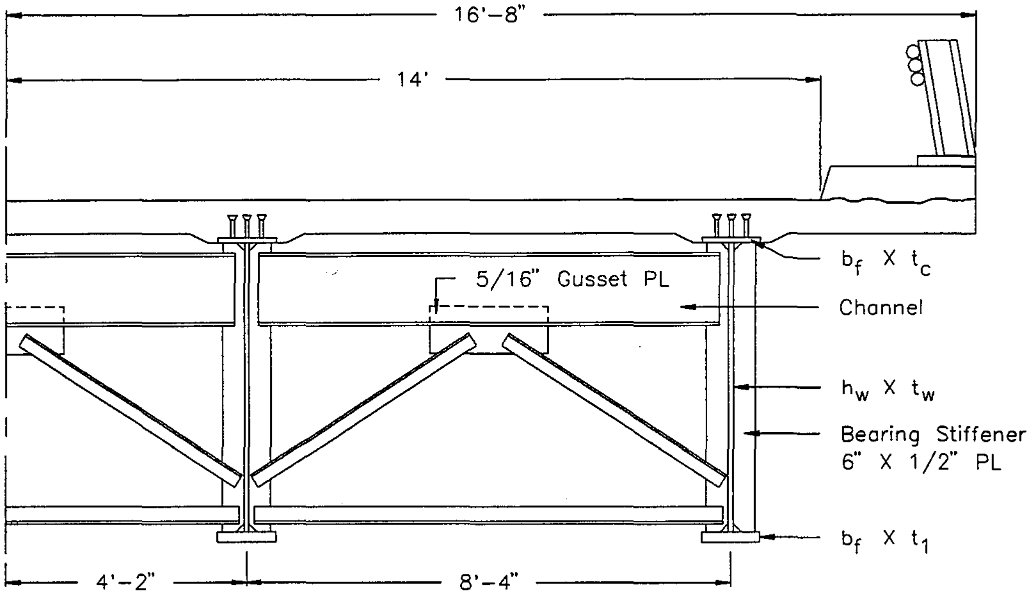

(a) End Frame

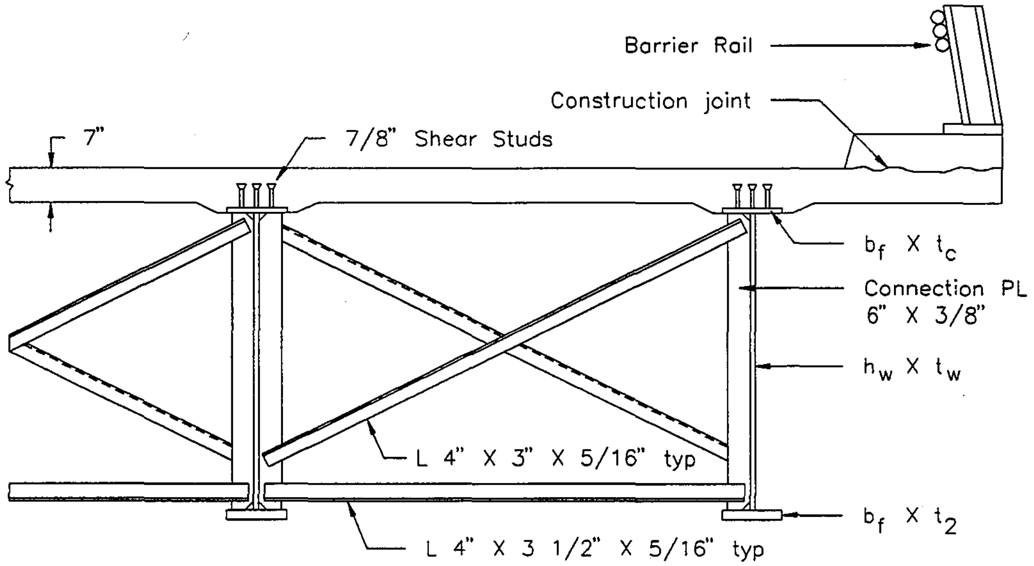

(b) Intermediate Cross Frame

Figure 4.1: One-lane Section of a Typical Bridge Design

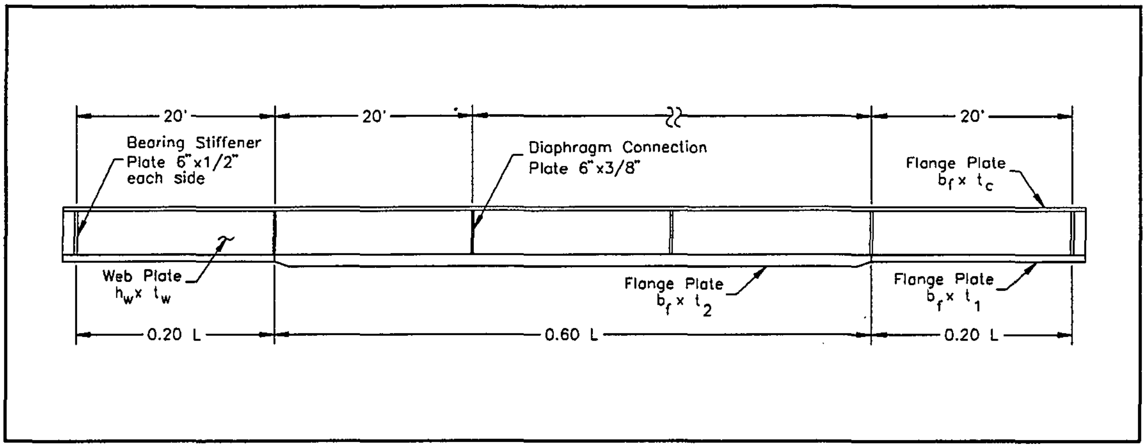

Figure 4.2: Girder Elevation of a Typical Bridge Design

reduced at the girder ends to save material in the lower moment region. Cross-sectional properties of these bridge designs are tabulated in Appendix A.

Details were adapted from examples in the US Steel Design Manual.[30] A constant girder spacing of 8'-4" and a slab thickness of 7" was used throughout. Slab reinforcement was #6 bars at 6 inches each way. Intermediate cross frames were the cross type of rolled angle members. These were spaced at 20' along the span. End frames consisted of a channel header together with rolled angles in an inverted vee. For each bridge design, wider versions were developed by increasing the number of girders at the same spacing. Skewed bridges were developed by altering the angle at which the bridge meets its supports, while maintaining the same span for each girder and the same perpendicular spacing between girders as the corresponding orthogonal bridge. Intermediate cross frames were maintained perpendicular to the girders for all skewed bridges. In order that the girder nodes line up across the width of the bridge, each girder was offset from the perpendicular by an even number of feet N. This was defined as the skewing offset as illustrated in Figure 4.3. The skew angle γ is related to N by

$$\gamma = Tan^{-1}\left(\frac{12N}{100}\right) \tag{4.1}$$

Skew was varied between 0° and 63° using even *N* values from 0 to 16. This approach had the inherent advantage of finer increments of skew angle towards the high end of the range, where structural response changes rapidly with increasing skew.

As the present study is concerned with geometric and constraint parameters rather than material properties, a set of standard material properties was selected and used throughout. Grade 50 bridge steel was selected for the girders, as these steels are in common use for most new bridge superstructures. For the bridge deck, 4000 psi compressive strength concrete was selected as typical of present practice. Physical properties of these materials are tabulated in Table 4.1. The thermal expansivity of reinforced concrete can vary from 0.0000053 to 0.0000065 in/in/°F and depends on mineralogy of aggregate, type of cement, water-cement ratio, concrete age, and amount

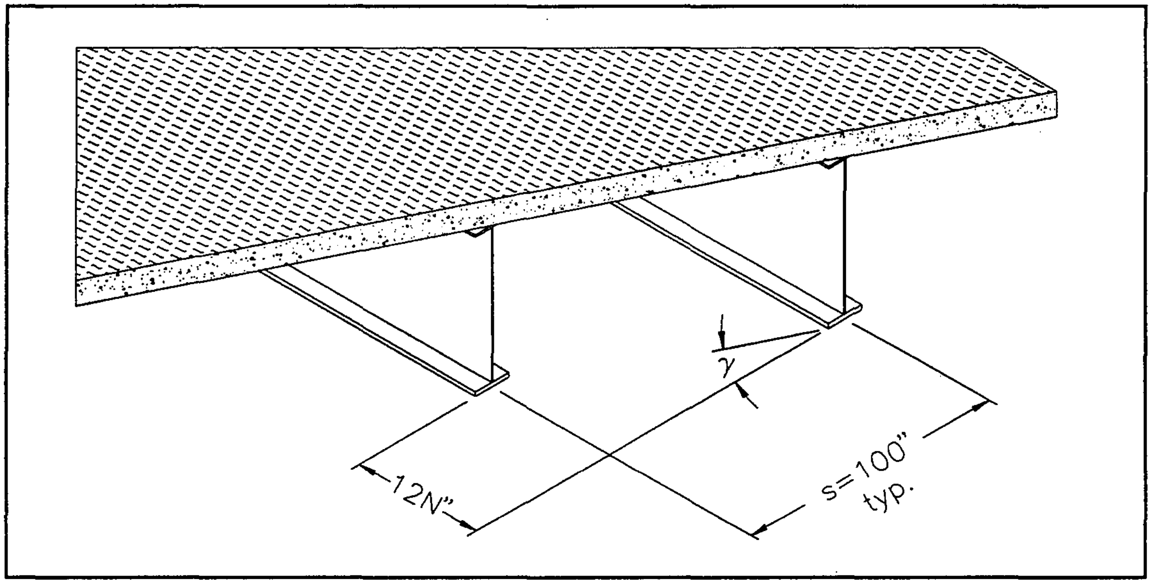

Figure 4.3: Definition of Skewing Offset *N*

Table 4.1: Properties of Steel Bridge Materials

Property	Units	Steel	Concrete
Elastic Modulus	psi	E_s = 29,000,000	E_c^* = 3,600,000
Poisson's Ratio	N/A	ν_s = 0.30	ν_c^{**} = 0.18
Weight Density	lb/ft^3	ρ_s = 490	ρ_c = 150
Thermal Expansivity	in/in/°F	α_s = 0.0000065	α_c = 0.0000060
Yield Strength	psi	F_y = 50,000	--- N/A ---
Compressive Strength	psi	--- N/A ---	f_c' = 4000

of reinforcement.[14] Most codes suggest taking α_c as $6.0\text{x}10^{-6}$. A test bridge was used to measure sensitivity to α_c of the bearing displacements. Results obtained for the extreme values varied less than 4% from those obtained using the suggested value.

4.2 Finite Element Models

Thermal deformations and induced strains, stresses, and reaction forces were calculated by the finite element method. MSC/NASTRAN was used for this purpose. NASTRAN is a powerful finite element code with a large element library capable of three-dimensional analysis of complex structures subjected to many types of loading and arbitrary boundary conditions. As NASTRAN was developed for use in the space program, it also has excellent thermal capabilities. Care was taken to ensure that the models were as accurate as feasible. As the models were relatively large, (50,000 to 120,000 degrees of freedom) they are especially sensitive to ill-conditioning, and a balance must be maintained between model detail and numerical performance.

---

[*] As suggested by ACI Code $E_c = 57{,}000\sqrt{f_c'}$

[**] As suggested by DIN 4227 $\nu_c = \sqrt{f_c'} / 350$

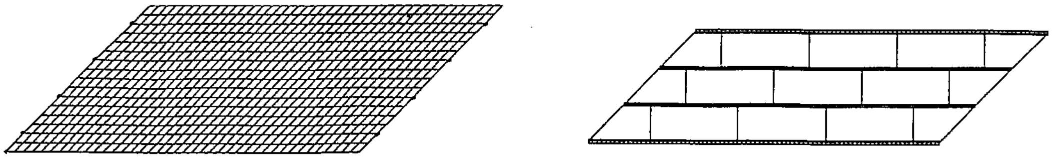

(a) Plan View

(b) Plan View with Slab Removed

(c) Section at End Frame

(d) Section at Intermediate Cross Frame

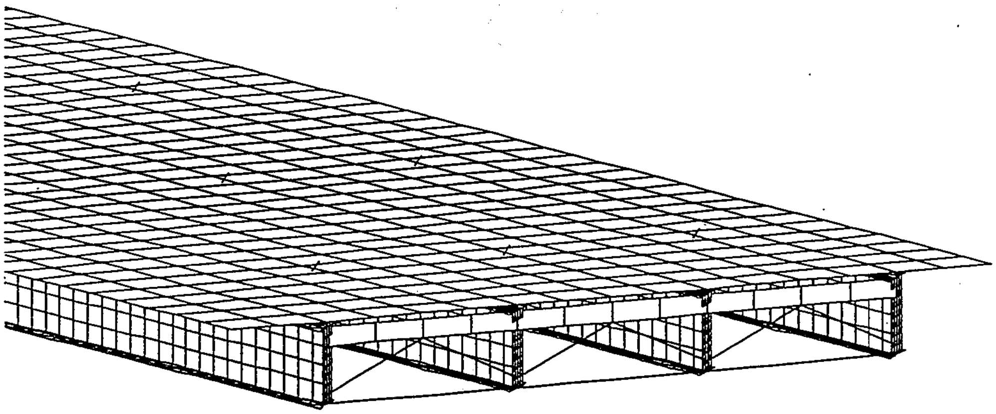

(e) Hidden Line Isometric End View

Figure 4.4: Views of a Typical Finite Element Model

Figure 4.4 shows a typical finite element model. Both the webs and the flanges of the girders were meshed with CQUAD4's, general four-node quadrilateral shell elements. Four elements were used through the depth of the web and across the width of the flanges. Several preliminary runs were made using beam elements to model the flanges. While results were close with a considerable reduction in model size, mesh problems arise at the cross-frame connections. This approach was therefore abandoned. Rolled angle members used in the cross frames were modeled by the CROD, a classic truss element. The channel header of the end frames was modeled as an equivalent plate constructed with CQUAD4's. The slab was also modeled with CQUAD4's at four elements across the girder spacing. The slab was connected to the girders at every node by RBE2's, rigid link elements.

4.3 Model Details

As the bridges used in the study were designed for composite action, the models must simulate this. In mathematical terms, compatibility must be enforced between the girders and the deck. Ideally, the displacement and curvature should be continuous across the girder-slab interface. Figure 4.5 shows three successively accurate means of accomplishing this. Part (a) shows a very crude model in which compatibility is enforced between the girder centroid and the slab middle surface. While this approach is inexpensive, it does not give satisfactory results. Part (b) shows the girder modeled as a true three-dimensional entity composed of surface elements. In this case, compatibility is enforced between the girder top flange and the slab middle surface. This approach gives good results, as the slab thickness is usually small in comparison with the total girder depth. Part (c) shows the slab composed of solid elements. While this approach is truly physically accurate, enforcing compatibility at the interface, it is not worthwhile for two reasons. First, it only yields slightly improved results as compared to part (b) for the increase in model size. Second, in NASTRAN temperatures may only be specified at node locations for solid elements, while a general temperature profile may be defined through the thickness of a surface element. The approach of Figure 4.5(b) was therefore used for all models in this study.

The RBE2 is actually a set of multi-point constraints that enslaves degrees of freedom at the slab nodes to those in the girder. A short investigation was conducted to determine the best implementation of this link. Three test models were run, having complete translational coupling together with no coupling, partial coupling, or complete coupling for rotational degrees of freedom. Results were compared to those obtained from analysis of a model using solid CHEXA elements for the slab. Full coupling gave results in closest agreement, and therefore this approach was adopted.

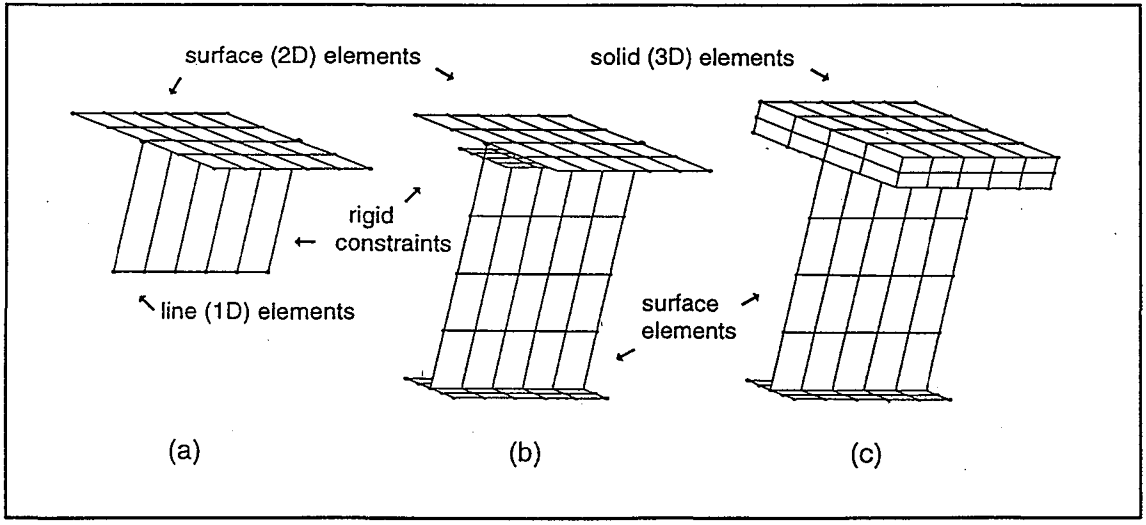

Figure 4.5: Finite Element Models of a Composite Flexural System

An investigation was conducted to assess the effect of shape sensitivity. The two types of element distortion involved in these models were aspect ratio and skew. Moderate aspect ratios are practically unavoidable except for very fine element division. For static analysis, aspect ratios less than 10 are considered suitable.[17] Aspect ratio was maintained at 4 or less, and is therefore not expected to present a problem. Skew is a natural consequence of the geometry of a skewed bridge. Parallelograms are required to model the deck. The CQUAD4 can become excessively stiff for this shape in its in-plane and plate bending modes. Table 4.2 summarizes the result of a brief investigation into the effect of skew on calculated structural responses. Tabulated values represent maximum bearing displacements, maximum bearing forces, and transverse deck stress near the supports. CPU times given for each run are for an IBM 370 series mainframe.

Table 4.2: Shape Sensitivity Study

Skew Angle	Slab Element	Bearing Displacement	Bearing Reaction	Slab Stress	CPU Time
0°	Q4	0.3159"	52,880 lb	240 psi	7.81 min
	Q8	0.3157"	52,360 lb	251 psi	12.04 min
25°	Q4	0.3755"	44,050 lb	215 psi	7.78 min
	Q8	0.3758"	44,010 lb	228 psi	11.94 min
45°	Q4	0.4036"	35,450 lb	154 psi	7.95 min
	Q8	0.4041"	35,350 lb	168 psi	12.33 min
60°	Q4	0.4636"	37,420 lb	61.0 psi	7.95 min
	Q8	0.4657"	37,070 lb	69.9 psi	12.36 min

Two models were run for each skew angle— one with the CQUAD4 slab elements and one with CQUAD8 slab elements. The CQUAD8 element does not lock for the parallelogram shape, because its shape functions are complete through the second order.[17] Comparison of the results. shows excellent performance for the CQUAD4. Displacements are nearly exact to three significant digits, and bearing forces are within 1% for 35% less CPU time.

A final concern during the process of preparing models for analysis which was eluded to earlier is that of numerical integrity of the models. NASTRAN uses the diagonal decay error test to estimate the precision lost to truncation during the stiffness matrix decomposition.[7,21] The decay ratio r_i is the ratio of a diagonal entry in the original stiffness matrix to its corresponding entry in Gauss-reduced form:

$$r_i = \frac{S_{ii}}{U_{ii}} \tag{4.2}$$

where the matrix $[U]$ comes from the triangular decomposition

$$[S] = [L]\,[U] \tag{4.3}$$

in which $[U]$ = upper-triangular Gauss-reduced form of $[S]$, and $[L]$ = unit-lower-triangular matrix of factors used in the elimination. NASTRAN defines MAXRATIO as the largest of the decay ratios. The value of $\log_{10}$ (MAXRATIO) gives an upper bound estimate of the number of significant digits of precision lost. MAXRATIO is recalculated row by row as unknowns are eliminated, and if the equation solver encounters MAXRATIO greater than a preset limit, the solution process will terminate. The causes of large decay ratios are large stiffness differentials, mechanisms within the structure, and inadequate supports. These problems were circumvented by using rigid links (handled internally by additional constraint equations) rather than stiff beam elements for shear studs and by avoiding unnecessary detail, especially at the cross-frames. MAXRATIO was on the order of 10^3 for the models used in this study; thus of 13 significant digits, 3 or 4 may have been lost to truncation, which is well within acceptable limits. Checks were also made to see that computed results agreed with hand calculations for simple load cases and that the structure responded symmetrically to symmetric load cases.

CHAPTER 5

PARAMETRIC STUDIES

5.1 Constraint Cases

In order to examine the effect of bearing placement and orientation, the models were run for the following constraint cases, shown graphically in Figure 5.1:

- Traditional
- Radial from Corner
- Radial from Center

The Traditional constraint case represents the usual method of bearing placement. Fixed bearings are installed across the full width on one end of the bridge (shown as X's in the figure). Partially moveable bearings are installed at the opposite end, which allow expansion in the longitudinal direction only. This the simplest bearing arrangement, and has long been the most commonly used. It has the advantage of redundancy to distribute horizontal forces on the bridge to several bearings, but this redundancy also makes the structure susceptible to large forces that may develop when the bridge expands under thermal loading. To alleviate this problem, more recently the trend has become to allow movement in all directions from a single fixed point, as in the two radial constraint cases. The Radial from Corner constraint case employs a fixed bearing at the first girder at the acute angle, and partially moveable bearings at the other supports, which allow

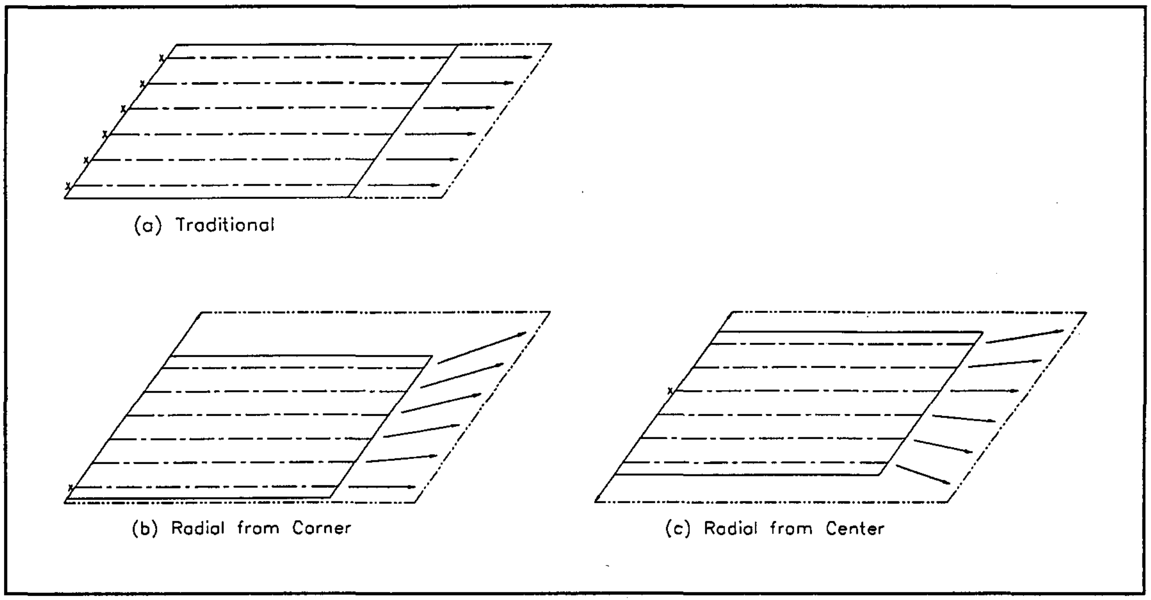

Figure 5.1: Bearing Orientation for Constraint Cases

expansion radially from the fixed bearing. The Radial from Center constraint case is similar except that the fixed bearing is located at the girder halfway across from the obtuse angle. Ideally, both of these cases should be determinate and result in zero restraint forces in the horizontal plane. However, this is no longer the case with a nonuniform temperature gradient through the depth of the bridge, and a section composed of materials with different expansive characteristics. These constraint cases are denoted by the subscripts T, RO, and RM.

5.2 Temperature Loading

The loadings used for all bridges in this study were adapted from the 1994 AASHTO Design Specifications[1] and a 1987 study by Kennedy and Soliman[15]. AASHTO prescribes a temperature range of 0 °F to 120 °F for steel bridges in the moderate climate zone. Assuming a representative setting temperature of 70 °F, this means that the bridge may experience a temperature rise of +50 °F in the summer and a

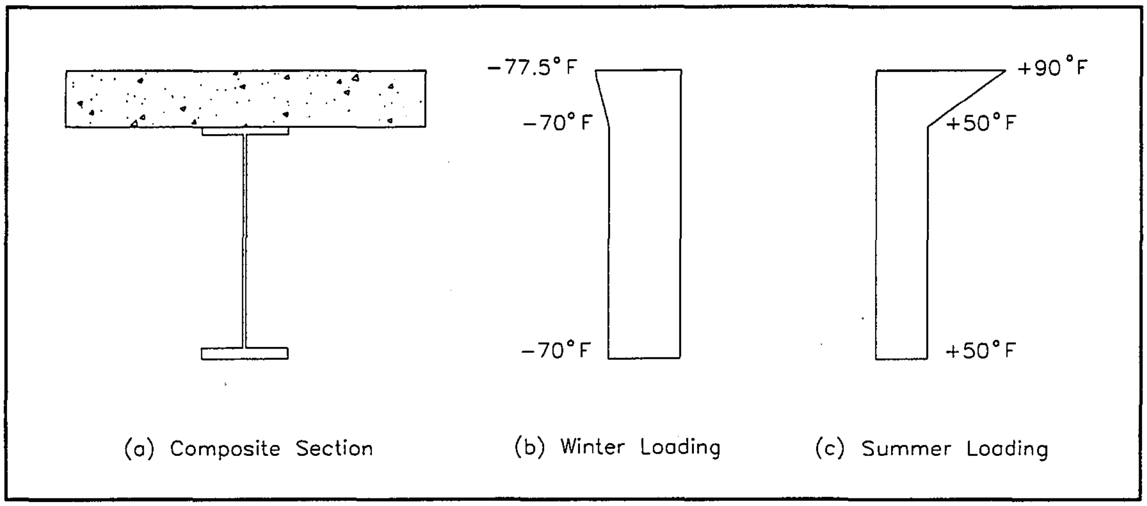

Figure 5.2: Temperature Loading for Steel Bridge Models

temperature fall of -70 °F in the winter. Kennedy and Soliman proposed a simple temperature gradient for composite steel bridges based on a synthesis of several theoretical and experimental studies on prototype bridges. This gradient is linear through the depth of the slab, and uniform through the depth of the steel girder. The magnitude of the temperature gradient ΔT is the differential temperature at the top of the slab relative to the temperature of the girder. The value of $+\Delta T$ for summer conditions is sight-dependent and was suggested as +40 °F for the Middle Atlantic States. The value of $-\Delta T$ for winter conditions was suggested as -7.5 °F for all locations. It is interesting to note that the $+\Delta T$ value suggested by Kennedy and Soliman compares closely to the AASHTO recommended maximum surface temperature T_1 of 41 °F for Solar Radiation Zone 3, which encompasses the entire Eastern United States. The total temperature loadings for winter and summer cases are shown in Figure 5.2. The winter loading was used to determine bearing displacements, and the summer loading to determine restraint forces at the bearings.

5.3 Parameters and Ranges

A survey of parameters which may affect a bridge's thermal response was conducted prior to the numerical investigation. Parameters which were thought to have an important effect or had been used in previous researches include:

- Span Length
- Width (Aspect Ratio)
- Depth (Span to Depth Ratio)
- Skew Angle
- Slab Thickness*
- Girder Spacing*
- Diaphragm Spacing*

Parameters flagged by asterisks were not included because either they are confined within a narrow range by design practice, or are directly related to other parameters, and therefore could not be varied independently. For the parameters which were included, each was tested over its entire range of reasonable values, as tabulated in Table 5.1. The parameters were varied one at a time so that their particular effects could be isolated.

Table 5.1: Ranges of Parameters

L	Span Length	80' - 180'
W/L	Aspect Ratio	0.25 - 1.00
L/D	Span-to-Depth Ratio	16 - 26
γ	Skew Angle from Orthogonal	0° - 63°

Each test on a particular parameter included multiple series which used different values of the other parameters, so that coupling effects between them would be evident. Emphasis was placed on shorter span lengths, as these bridges tend to be more problematic. Appendix B lists parameter values for each of the models.

5.4 Nomenclature

The geometry of each bridge model is defined by four parameters. Codes for these parameter values are combined to form a six-character identifier for each model of the form *LDDGNN*. The significance of each of these codes is explained in Table 5.2.

Table 5.2: Codes for Model Geometric Parameters

Code		Possible Values
L	Span Length	A, B, ..., F
DD	Span to Depth Ratio	16, 17, ..., 26
G	Number of Girders	4, 6, 8, 0
NN	Skewing Offset	00, 02, ..., 16

The first code *L* is an alphabetic character which identifies the span length. The value *A* indicates a span length of 80'. Each successive letter indicates a span length 20' greater. The second code *DD* gives the span to depth ratio to the nearest whole number. This value is calculated based on the total depth of the composite section, not the steel section alone. The third code *G* specifies the number of girders. As the girder spacing is a constant 100", the total width in inches for each model is equal to 100 times the number of girders. A value of $G = 0$ indicates 10 girders, or a total width of 1000", not zero. The last code *NN* represents the two digits of the skewing offset *N* for the model, as explained in Section 4.1. Values of skew corresponding to each value of *N* are tabulated in Table 5.3. This system of nomenclature provides a concise means of identifying parameters for the models used in the studies which follow. The text and chart legends adhere to this system. An *X* is used to indicate that a particular parameter varies over its own range of values. For example, C20808 is a bridge model with a 120' span, a span to

Table 5.3: Skew Angle for Values of *NN*

Skewing Offset	Skew Angle	Nominal Skew
00	0.00°	0°
02	13.50°	13°
04	25.64°	25°
06	35.75°	35°
08	43.83°	45°
10	50.19°	50°
12	55.22°	55°
14	59.24°	60°
16	62.49°	63°

depth ratio of 20, 8 girders, and a 45° skew. C208XX is a series of models, each having the aforementioned span, depth, and width, in which the skew angle varies over its full range of 0° to 63°.

5.5 Effect of the Span Length

Span length is obviously a key parameter affecting bearing displacements under thermal expansion, as the resulting deformation is proportional to original length. Bearing displacements under all three constraint cases are therefore expected to increase with increasing span length. There is no such intuitive expectation of how span length might affect restraint forces at the bearings. Four series of models were tested to investigate the effect of the span length:

▸ XXX400	A four-girder orthogonal series
▸ XXX404	A four-girder, 25° skew series
▸ XXX408	A four-girder, 45° skew series
▸ XXX600	A six-girder orthogonal series

In each case, span length was varied from 80' to 180'. Characteristic section depths were used for each span length.

The effect of span length on the structural response is plotted in Figures 5.3 through 5.5. As expected, bearing displacements increase linearly with increasing span length. Under the Traditional constraint case, displacements for all four series plot as parallel lines. Displacements for the four- and six-girder orthogonal series are coincident. Displacements are on average 0.05" greater for the 25° skew series, and 0.08" greater for the 45° skew series. Under the Radial from Corner constraint case, displacements are visibly affected by width as well as skew, although the effect of width becomes less pronounced for greater span lengths. Displacements are 0.06" greater for the 25° skew series, and 0.13" greater for the 45° skew series. The six-girder series traces a slightly smaller slope than the corresponding four-girder series. Displacements under the Radial from Center constraint case appear very insensitive to anything other that span length, as results for all four series tested vary less than 2%. The greatest displacements under each constraint case are 1.070,1.123, and 1.028, respectively. It is interesting to note that the displacement trends are nearly parallel for all series and all constraint cases, suggesting very little coupling between span length and the other parameters with regard to bearing displacements.

Restraint forces at the bearings generally decrease with increasing span length for all three constraint cases. Perhaps this is because the additional length renders the structure more flexible. All four series exhibit a similar trend under the Traditional constraint case. Skew and length seem uncoupled, as all three four-girder series are nearly parallel. As compared with the orthogonal series, bearing forces are on average 10 kips greater for the 25° skew series and 35 kips greater for the 45° skew series. The irregularity between span lengths of 120' and 140' is probably due to a change in flange plate width (see Appendix A). There is some degree of coupling between width and length, as the six-girder series traces a steeper slope than the corresponding four-girder series. For the two orthogonal series, there is approximately a 20% reduction in bearing force when span length is doubled from 80' to 160'. Bearing forces under the Radial from Corner constraint case seem inversely proportional to span length. Comparing the two orthogonal series, bearing forces for the six-girder series are approximately 3 times those for the four-girder series. Bearing forces for the two skewed series are nearly equal. They trace similar trends to those of the orthogonal series, but at much greater magnitudes. Under the Radial from Center constraint case, all four series plot differently. The two orthogonal series trace similar trends as for the Radial from Corner constraint case, but at 5 times the magnitudes on average. Bearing forces are greatest for the 25° skew series, and show almost no change with increasing span length.

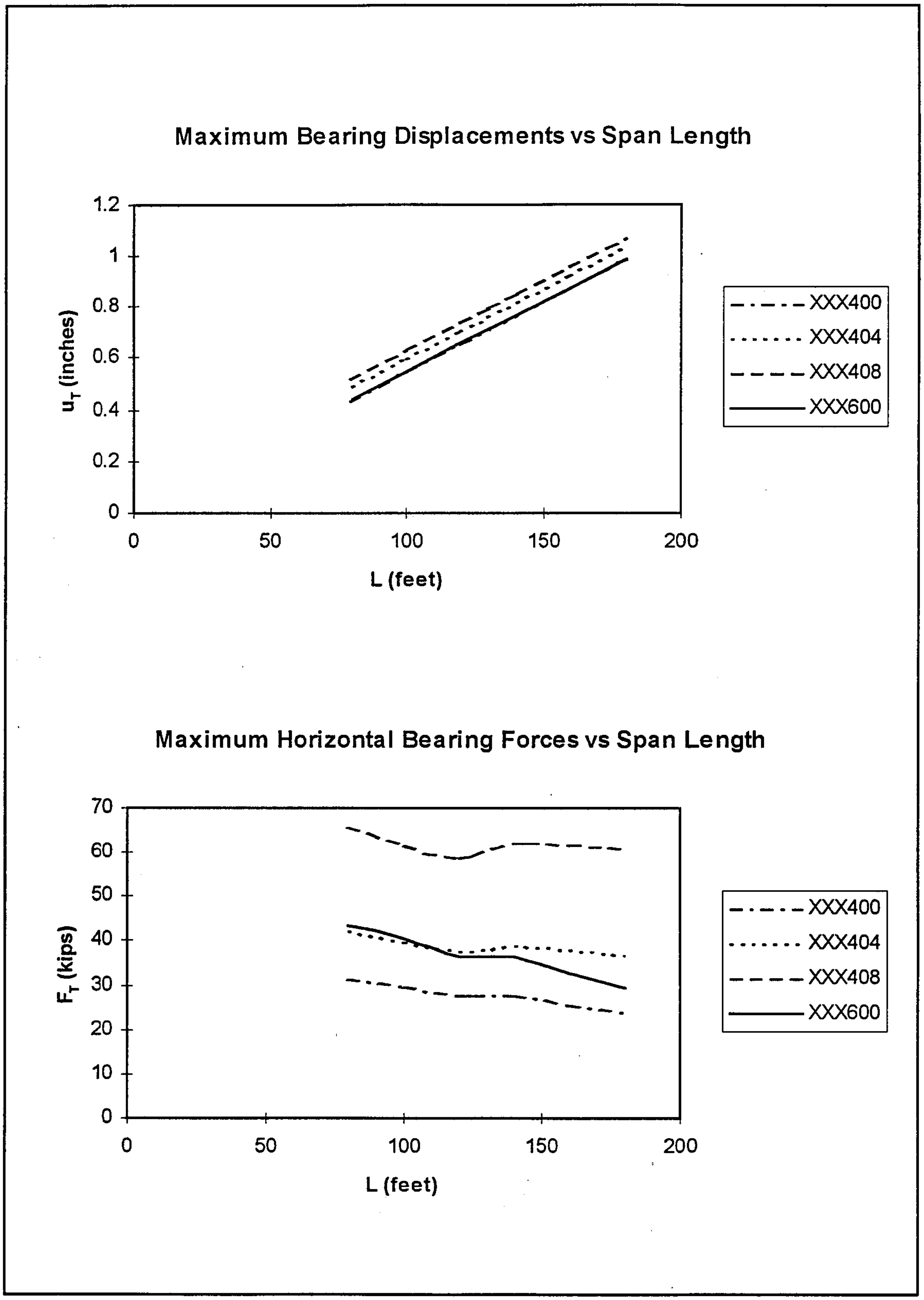

Figure 5.3: Effect of Span Length Under Traditional Constraint Case

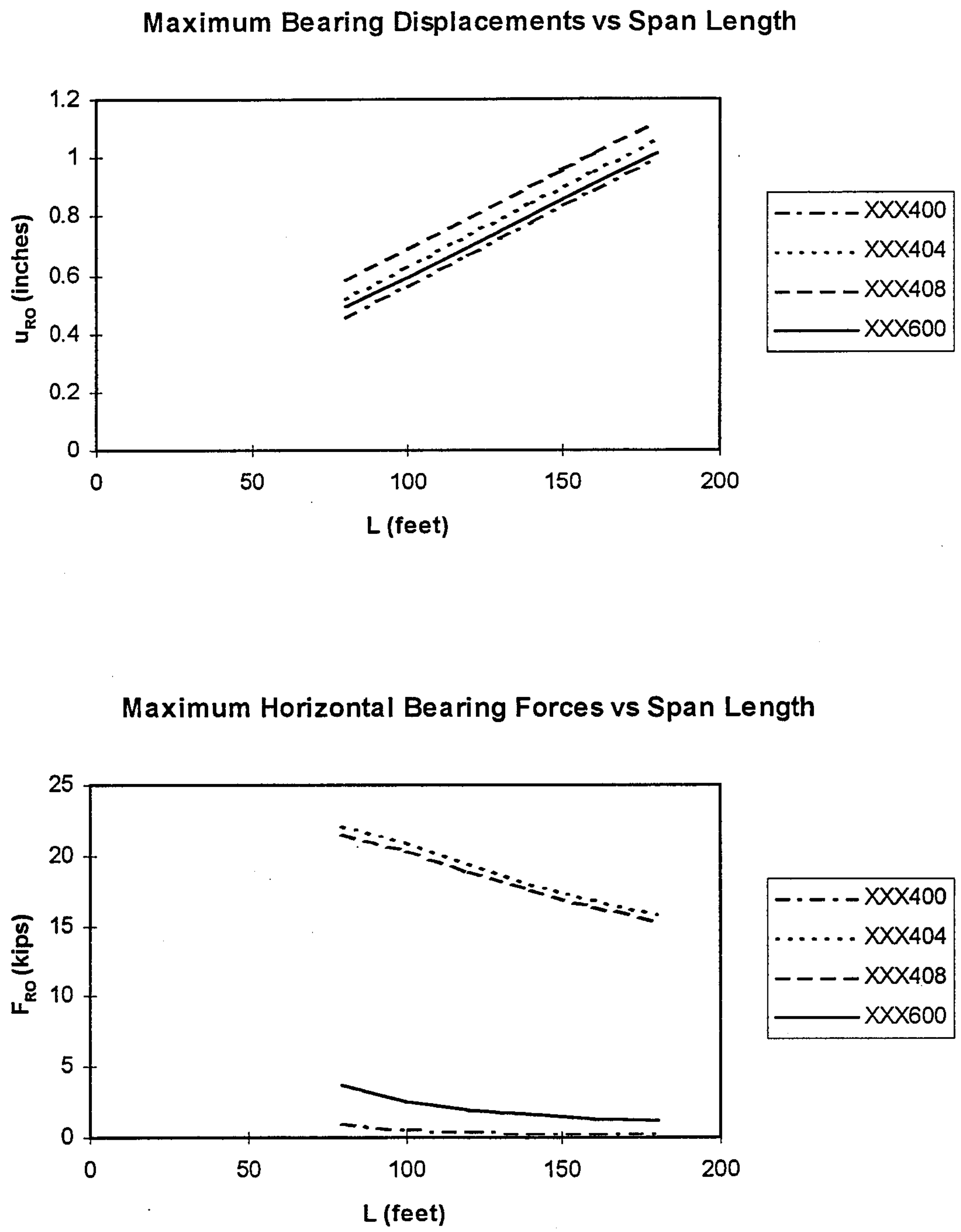

Figure 5.4: Effect of Span Length Under Radial from Corner Constraint Case

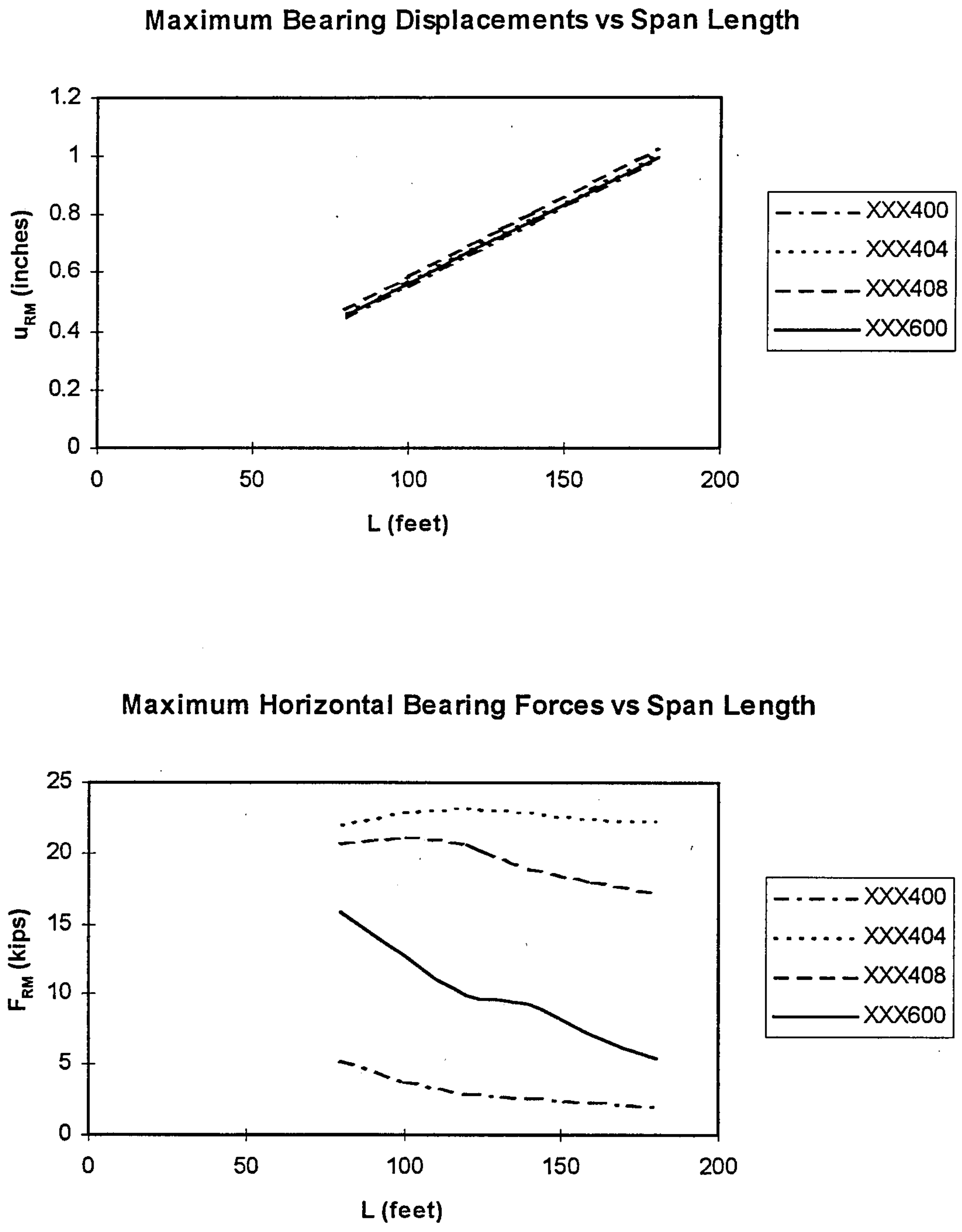

Figure 5.5: Effect of Span Length Under Radial from Center Constraint Case

5.6 Effect of the Skew Angle

Skewed bridges exhibit an altogether different response pattern with regard to both bearing displacements and restraint forces than do orthogonal bridges. This has led to structural distress for many of these bridges, particularly wider ones. The skew parameter used in this study, γ, is defined as the skew angle measured from the orthogonal, i.e. $\gamma = 0°$ for an orthogonal bridge. Five series of models were tested to investigate the effect of the skew angle:

▸ A174XX	An 80' span, four-girder, L/D = 17 series
▸ A178XX	An 80' span, eight-girder, L/D = 17 series
▸ A228XX	An 80' span, eight-girder, L/D = 22 series
▸ B218XX	A 100' span, eight-girder, L/D = 21 series
▸ C208XX	A 120' span, eight-girder, L/D = 20 series

In each case the skew angle was varied from 0° to 63°. While this may not bound the entire range of skew angles encountered in practice, the analysis was limited by the allowable distortion for a quad element.[19]

The effect of skew angle on structural response is plotted in Figures 5.6 through 5.8. Skew is indeed observed to exert a dominant influence for all three constraint cases. Bearing displacements increase linearly under the Traditional constraint case. Under the two radial constraint cases, the displacement trends resemble parabolas with very small upward curvature. Section depth is observed to have no appreciable effect on displacements, as A178XX and A228XX are coincident for all three constraint cases. The eight-girder series are parallel for all span lengths. The four-girder series traces a smaller slope. The greatest displacements under each constraint case are 0.9306, 1.292, and 0.9170, respectively. Again, span length and skew appear uncoupled, as displacement trends with increasing skew are parallel for different span lengths.

Restraint forces at the bearing vary considerably with skew angle. Bearing force trends for all these constraint cases are highly nonlinear and differ markedly from one another. Bearing forces under the Traditional constraint case increase almost linearly until about 50°, where they begin to increase sharply with increasing skew. Comparing the three 80' span series, it is observed that bearing forces increase with increasing width and span to depth ratio for all values of skew angle. Bearing forces diminish with increasing span length for similar span to depth ratios. Under the Radial from Corner constraint case, bearing forces do not continue to rise increase with skew beyond 30°. Instead, they trace a bell-shaped trend with a plateau of maximum values between 20° and 40°. Relative magnitudes are similar to those under the Traditional constraint case— larger bearing forces occur for greater widths, shallower sections, and shorter span lengths. Under the Radial from Center constraint case, bearing force trends are quite irregular, and it is difficult to discern how skew is interrelated with the other parameters. For the skew angles less than 20°, larger bearing forces occur for greater widths, shallower sections, and shorter span lengths, as before. For skew angles from 20° to 50°, there is little increase in bearing forces with increasing width. Results for the four-girder series and the corresponding eight-girder series only differ by 10% in this range. Bearing forces are actually greater for longer span lengths. Questionable results are obtained for very sharp skews. Bearing forces increase abruptly for the eight-girder series, and decrease for the four-girder series.

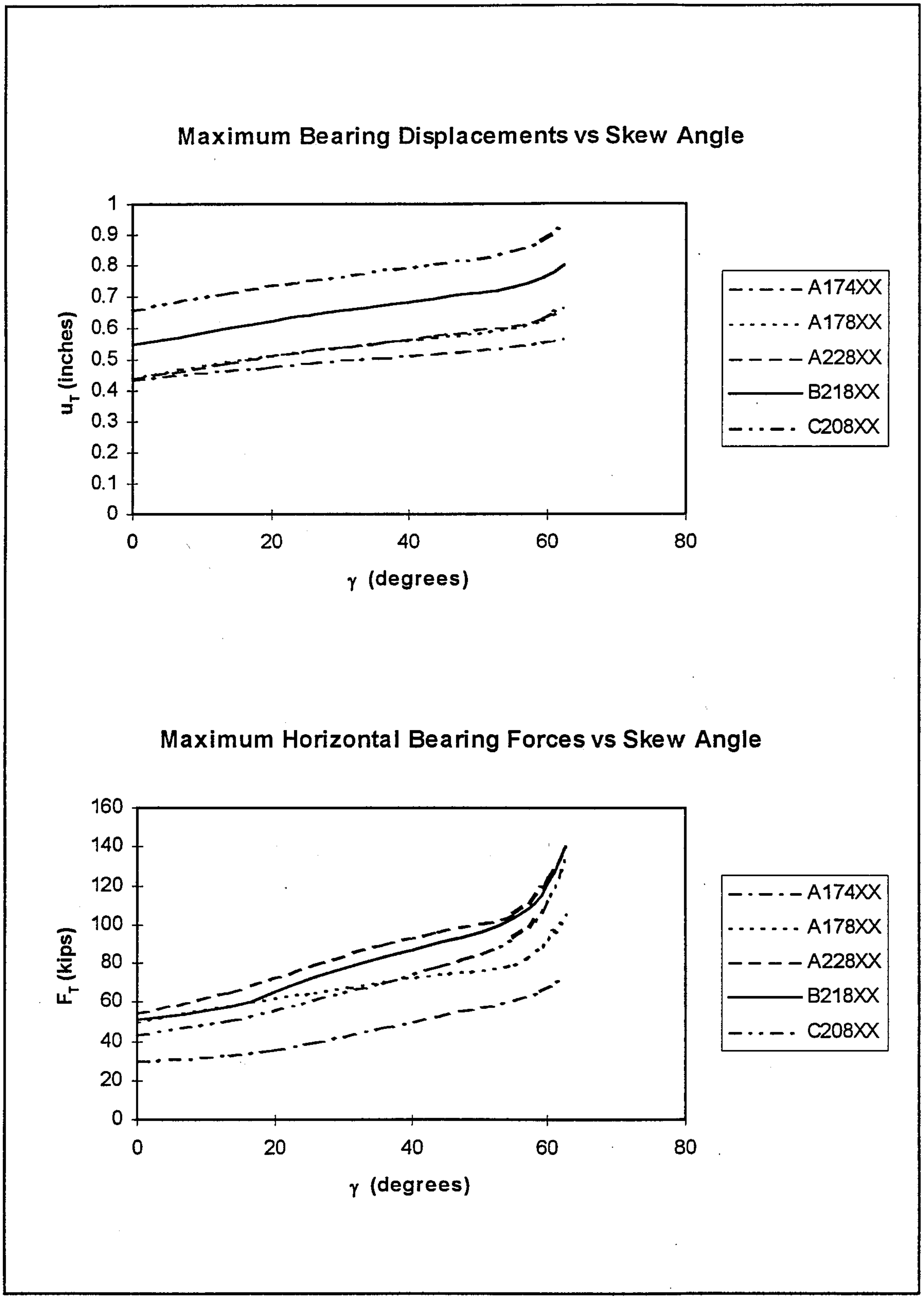
Maximum Bearing Displacements vs Skew Angle

Maximum Horizontal Bearing Forces vs Skew Angle

Figure 5.6: Effect of Skew Angle Under Traditional Constraint Case

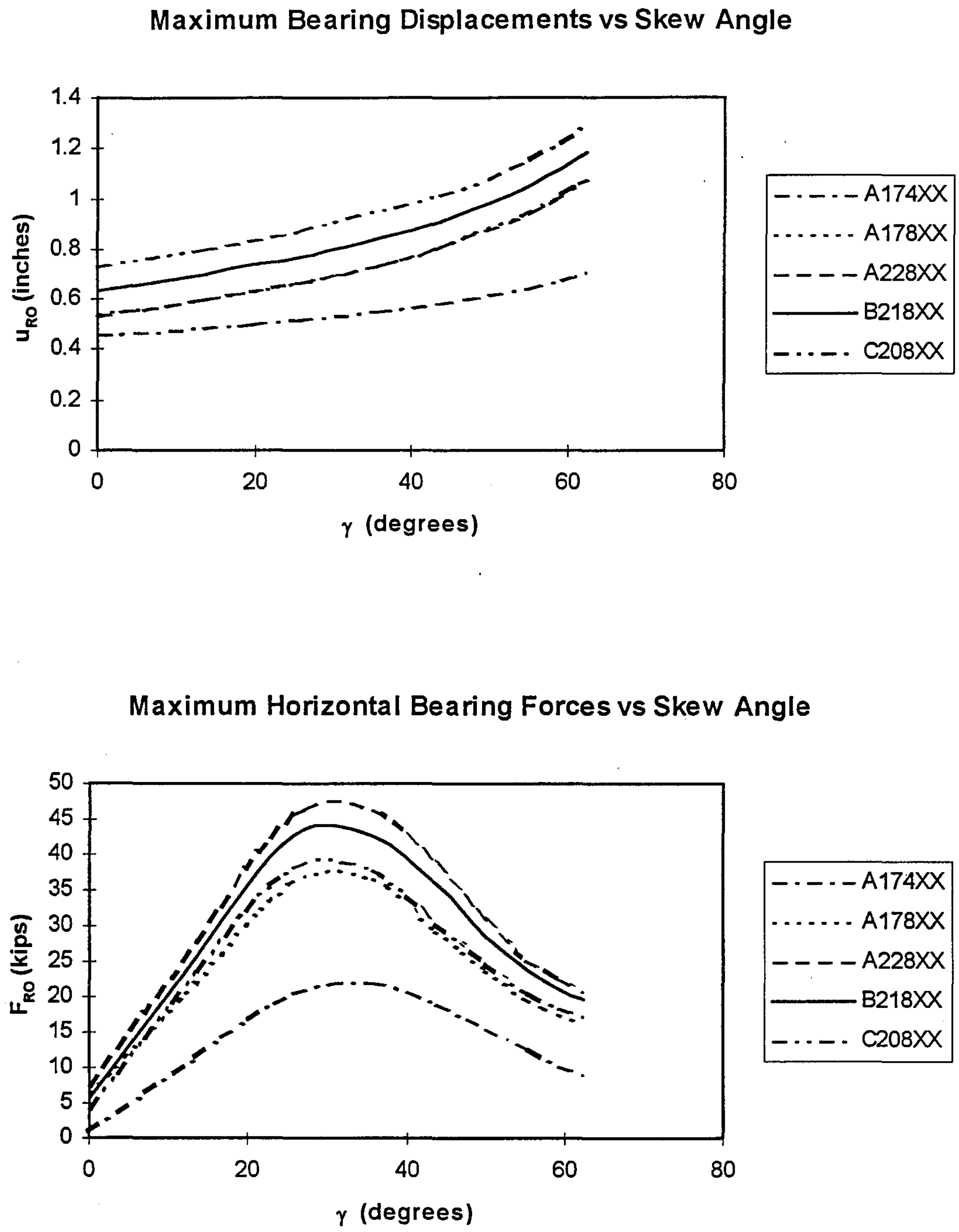

Figure 5.7: Effect of Skew Angle Under Radial from Corner Constraint Case

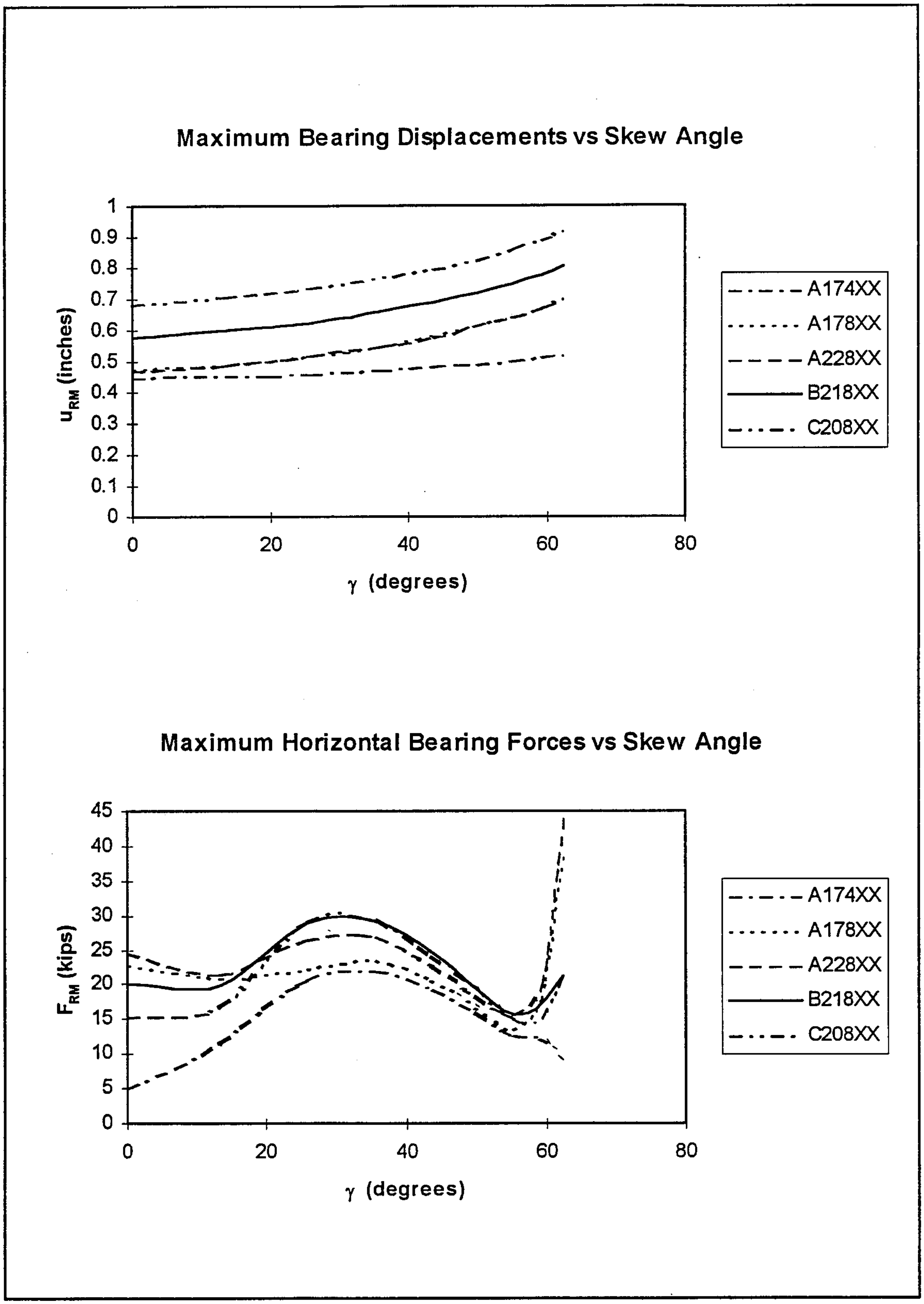

Figure 5.8: Effect of Skew Angle Under Radial from Center Constraint Case

Comparing the bearing forces induced by thermal loading under each constraint case, it is apparent that superior results are achieved for the radial constraint cases. Maximum bearing forces under each constraint case are 140.5, 46.5, and 29.5, respectively (ignoring the sharp rise in bearing forces for very high skew angles under the Radial from Center constraint case). Between the two radial constraint cases, Radial from Corner generally gives better results for skew angles less than 20° and greater than 50°, and Radial from Center gives better results for skew angles in between. Under the Traditional and Radial from Corner constraint cases, maximum bearing force always occurs at the first girder in the acute angle on the fixed end of the bridge. This same location controls under the Radial from Center constraint case for skew angles between 15° and 50°. Maximum bearing force occurs at the first girder at the obtuse angle for lesser skews, and at the fixed bearing for sharper skews. This explains why the envelope values of maximum bearing force do not plot such a smooth curve for this constraint case as for the other two.

Under the Traditional constraint case, bearing forces may be resolved into two components: F_x in the longitudinal direction and F_y in the transverse direction. The longitudinal component would normally be considered equal to zero, and this is indeed the case for an orthogonal bridge. A skewed bridge, on the other hand, experiences disproportionately high expansion along its long diagonal under a temperature gradient, as shown in Figure 5.9a. Thermal deformations of the slab may therefore be considered to be comprised of a uniform expansion component and a distortional component. The distortional component has the effect of lengthening the long diagonal and shortening the short diagonal, thereby exaggerating the skew of the slab. At the end of the bridge, where this type of distortion is restrained, large forces develop in the longitudinal direction of the bridge, as shown in Figure 5.9b. Components of the bearing forces for A228XX are shown in Figure 5.10. The transverse component F_y tapers off gradually with increasing skew, while the longitudinal component F_x increases rapidly with increasing skew.

Although bearing force trends versus skew angle are highly nonlinear, they may nevertheless be well described by rather simple relationships. As linear regression by least squares is the simplest systematic means of determining coefficients for these equations, forms were sought which could be linearized through variable transformation. Bearing forces under the Traditional constraint case are well approximated as exponential with increasing skew, as shown in Figure 5.11. The exponential relationship

$$F = \alpha e^{\beta \tan\gamma} \tag{5.1}$$

may be transformed to a linear relationship by taking the natural logarithm of both sides of the equation:

$$\ln|F| = \ln|\alpha| + \beta\tan\gamma \tag{5.2}$$

Very good correlation was achieved in this manner. All three series have coefficients of determination of 0.97 or better. Bearing forces under the Radial from Corner constraint case may be approximated by a three-part piecewise function, as shown in Figure 5.12. The first two parts are easily quantified, as they are both linear. The third part is fitted to a hyperbola. The basic hyperbolic relationship is given by

$$F = \alpha + \beta \frac{1}{\tan\gamma} \tag{5.3}$$

which is easily linearized by the transformation $x = 1/\tan\gamma$. Very strong correlation is achieved through this approach, with coefficients of determination of 0.99 and better, as shown in the figure.

While the relationships presented here almost perfectly model the observed variation in bearing forces with skew, they have some shortcomings. First, no such relationship could be found to adequately describe bearing force trends for the Radial from Center constraint case. Also, the coefficients α and β of the exponential function for the Traditional constraint case require many terms each for satisfactory accuracy, resulting in a lengthy and complex expression. Finally, the three-part form of the equation for bearing forces under the Radial from Corner constraint case is cumbersome. For these reasons, the design equations of Chapter 6 were not formulated from this approach. The relationships presented here are included strictly as insight into structural behavior.

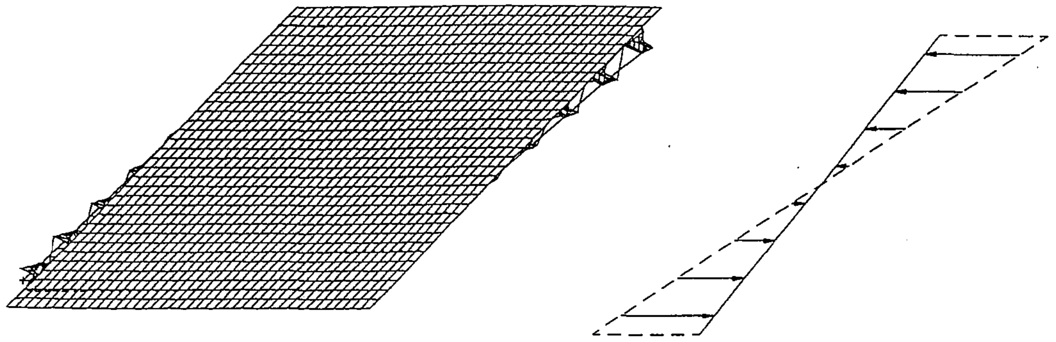

(a) Deformed Shape of Skewed Bridge

(b) Resulting Longitudinal Bearing Forces

Figure 5.9: Distortion Under Traditional Constraint Case

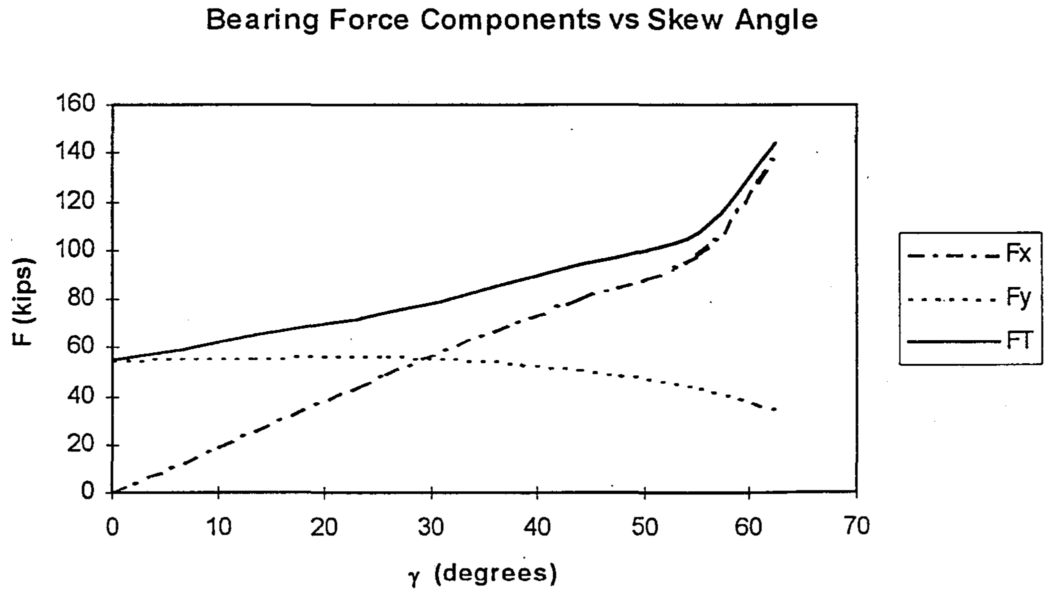

Figure 5.10:Components of Horizontal Bearing Force for a Typical Skewed Bridge

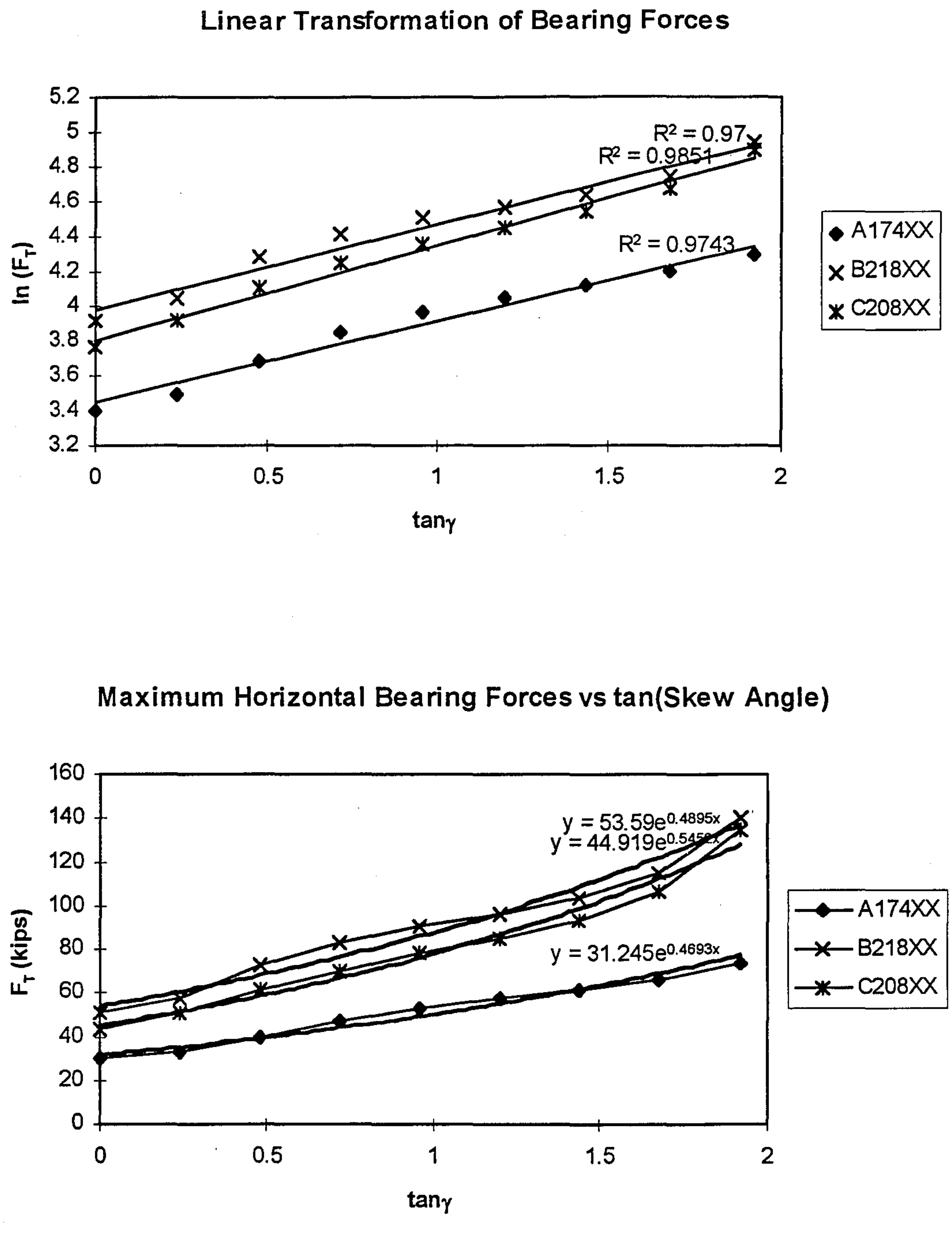

Figure 5.11: Exponential Model for F_T Under Traditional Constraint Case

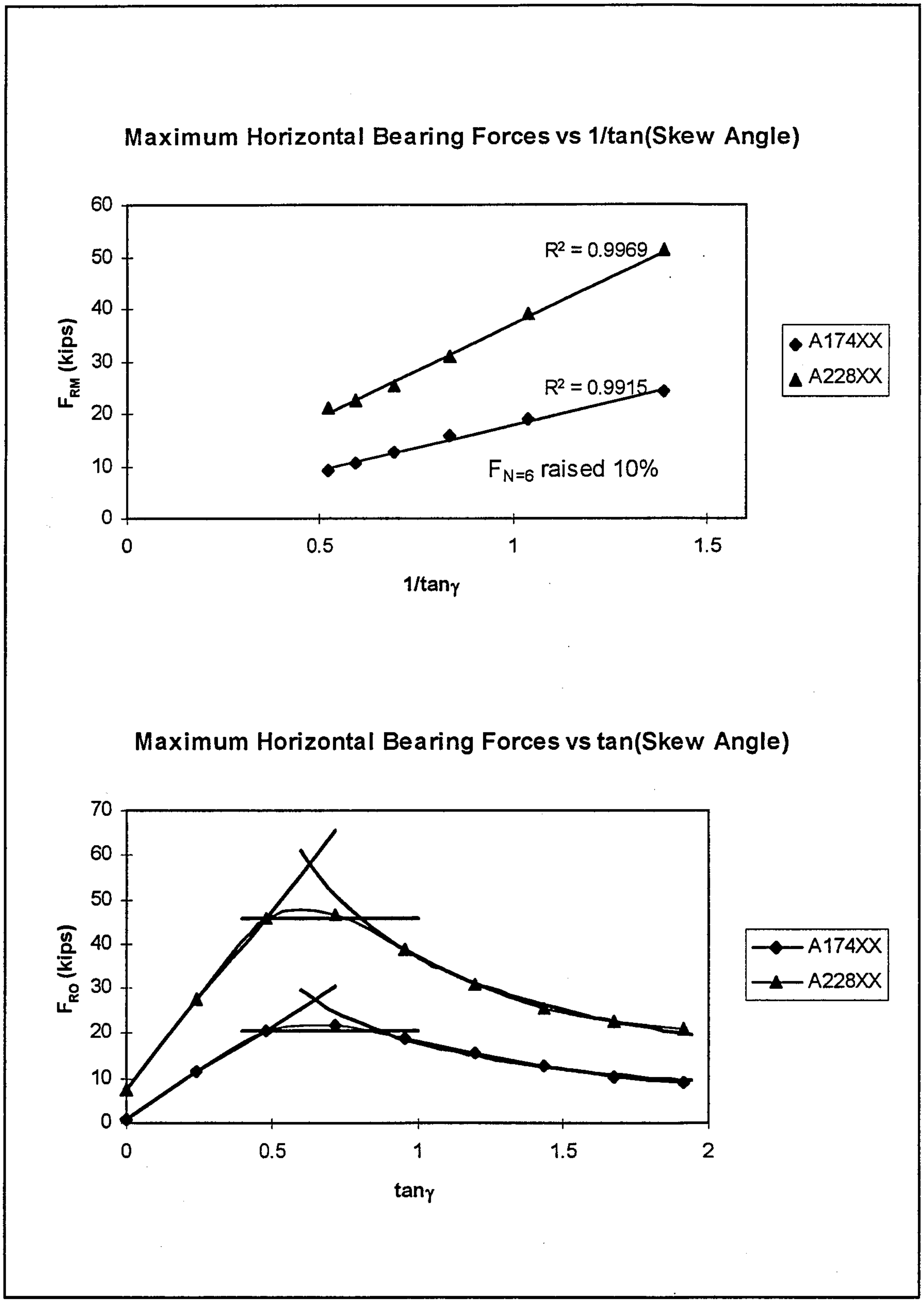

Figure 5.12: Hyperbolic Model for F_{RO} Under Radial from Corner Constraint Case

5.7 Effect of the Bridge Width

Width is naturally expected to be a dominant parameter affecting both displacements and restraint forces at the bearings. This is suggested by field damage reports as well as basic reasoning. Problems with bearing devices resulting from thermal effects almost always occur in relatively wide bridge structures. Five series of models were developed to investigate the effect of the bridge width:

▸ A17X00	An 80' span, L/D = 17 orthogonal series
▸ A17X04	An 80' span, L/D = 17, 25° skew series
▸ A17X08	An 80' span, L/D = 17, 45° skew series
▸ A22X00	An 80' span, L/D = 22 orthogonal series
▸ C20X00	A 120' span, L/D = 20 orthogonal series

In each case, the width was varied from 400" to 1000" using 4, 6, 8, and 10 girders. This corresponds to aspect ratios of 0.25 to 1.00.

The effect of bridge width is plotted in Figures 5.13 through 5.15. Bearing displacements increase linearly with increasing bridge width for all three constraint cases. A17X00 and A22X00 are coincident for each case. Under the Traditional constraint case, displacements for the orthogonal series are unaffected by width. The skewed series exhibit moderately larger displacements for greater widths. Slopes of their displacement trends are approximately equal. Under the Radial from Corner constraint case, all five series exhibit greater displacements with increasing width. The slopes of the displacement trends for the 25° skew and 45° series are 1.7 and 2.4 times those for the corresponding orthogonal series. This is the only constraint case for which A17X08 exhibits greater displacements than C20X00. Displacement trends under the Radial from Center constraint case closely resemble those under the Traditional constraint case, except that they are more sensitive to skew. Slopes for the 25° skew and 45° skew series are 2.0 and 3.3 times those for the corresponding orthogonal series.

Restraint forces at the bearings may also be well approximated as linear with increasing bridge width. The three orthogonal series trace similar responses under all three constraint cases. The 120' span consistently exhibits lesser bearing forces than the 80' spans. Comparing A22X00 with A17X00, the shallower section exhibits 8% greater bearing forces on average. Under the Traditional constraint case, the two skewed series and their corresponding orthogonal series are nearly parallel, suggesting that coupling effects between skew and width are insignificant. In fact, the regression line slopes vary less that 10% from one another. Bearing forces for the 25° skew and 45° skew series are 15 kips and 25 kips greater than those for the corresponding orthogonal series. Under the Radial from Corner constraint case, bearing forces for the orthogonal series are very low. The two skewed series have bearing force magnitudes similar to those under the Traditional constraint case. Bearing forces for the 25° skew series are actually 13% greater than for the 45° skew series. Bearing forces for the two skewed series appear unaffected by width under the Radial from Center constraint case, as both series trace nearly horizontal lines. Again, the 25° skew series exhibits slightly higher bearing forces than the more sharply skewed series.

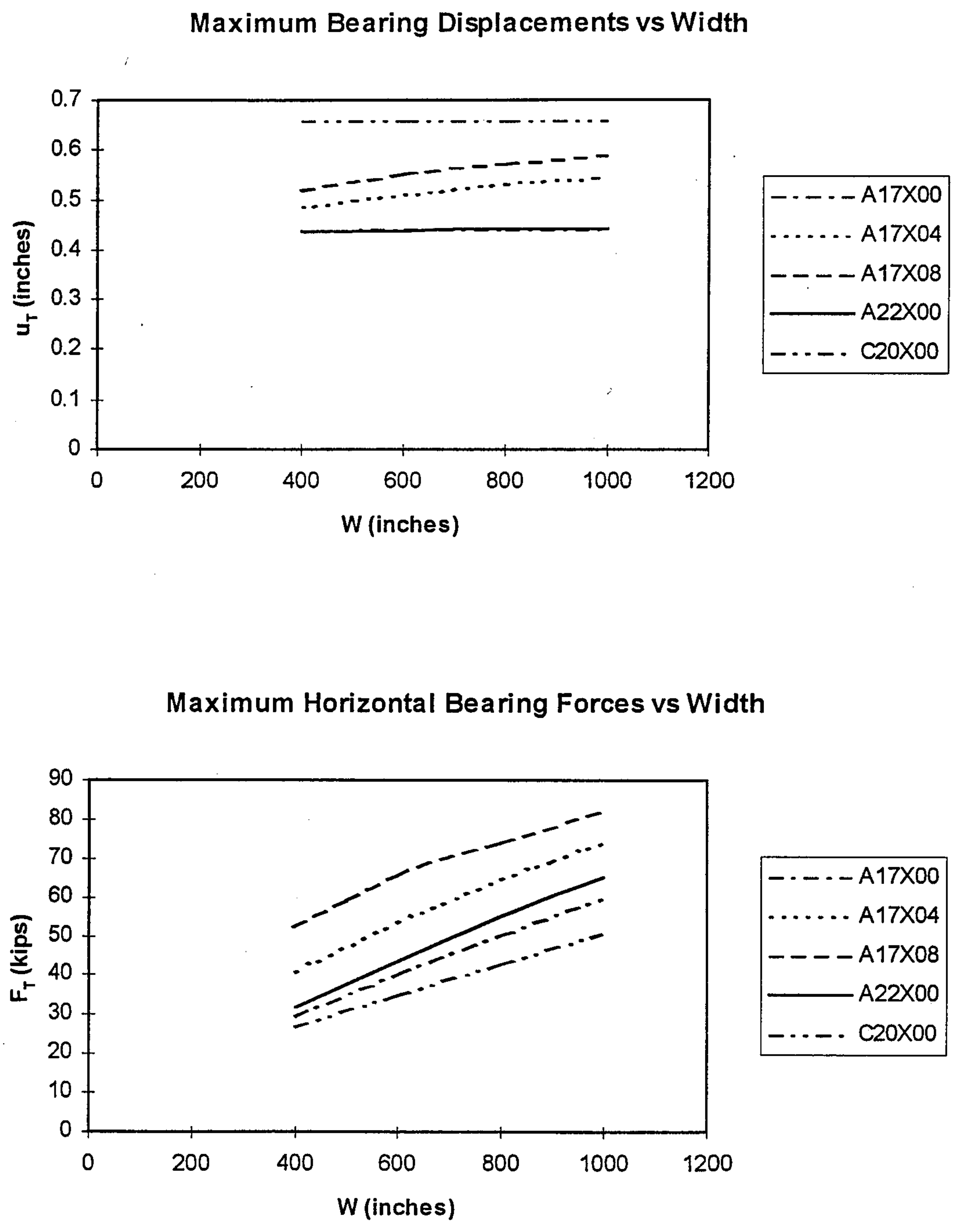

Figure 5.13: Effect of Bridge Width Under Traditional Constraint Case

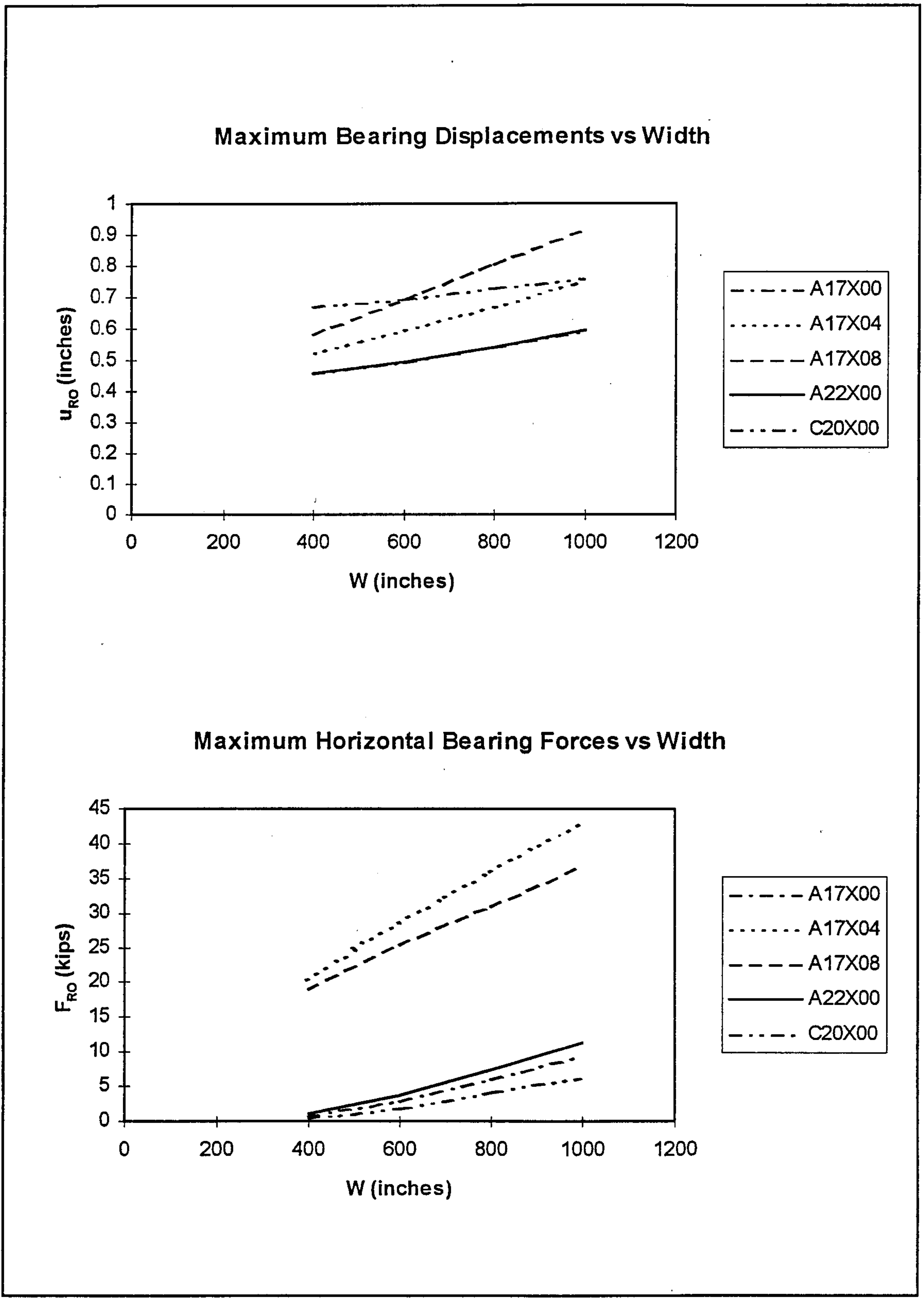

Figure 5.14: Effect of Bridge Width Under Radial from Corner Constraint Case

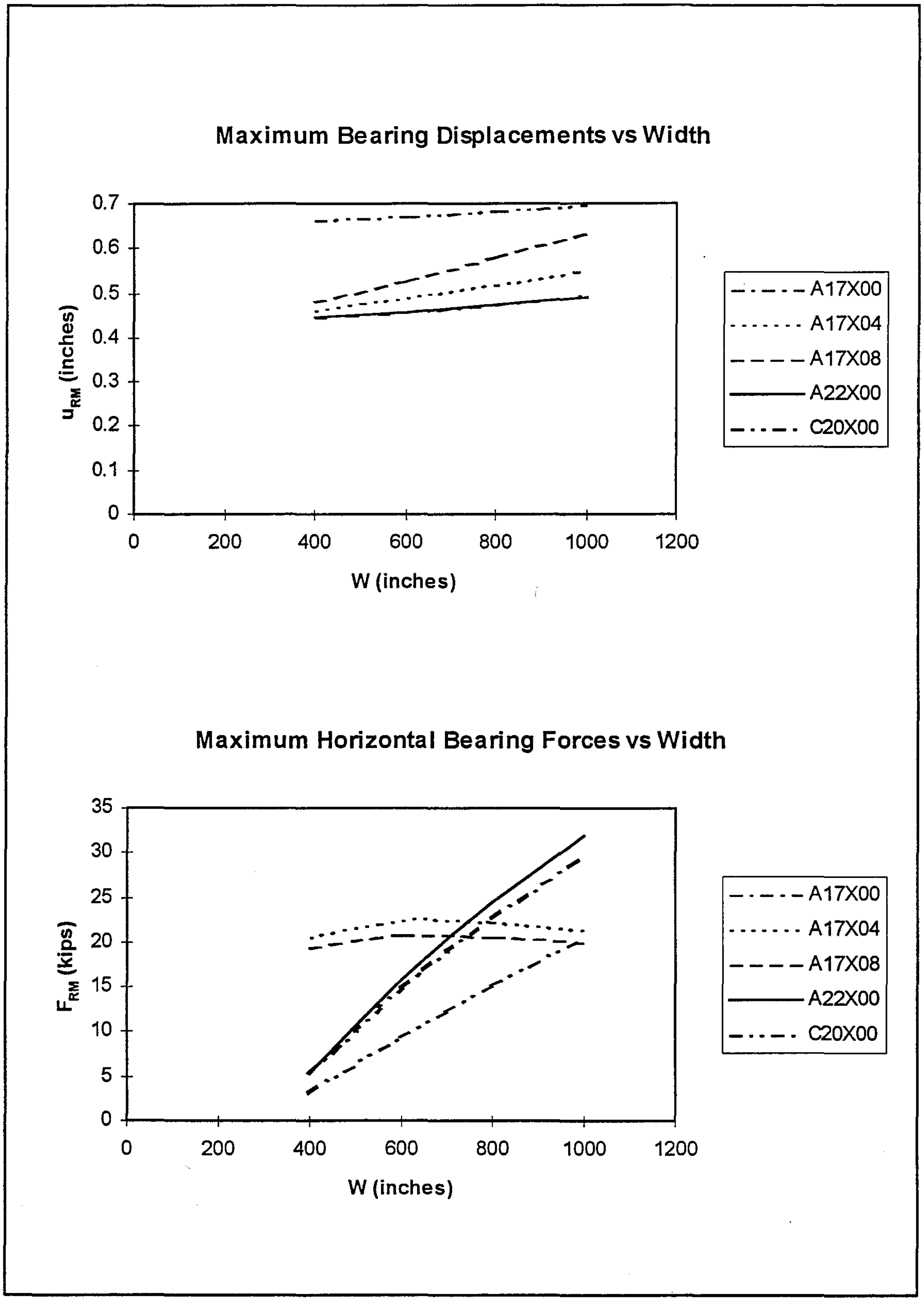

Figure 5.15: Effect of Bridge Width Under Radial from Center Constraint Case

5.8 Effect of the Section Depth

The section depth parameter is the span to depth ratio, L/D. This value is usually 20 to 24 for simple spans, although it can vary outside this range. A shallower section requires heavier flange plates, and thereby results in a stiffer section with respect to axial deformation as well as bending about a vertical axis. Bearing forces are therefore expected to increase with increasing span to depth ratio. Five series of models were tested to investigate the effect of the section depth:

▸ AXX800	An 80' span, eight-girder orthogonal series
▸ AXX808	An 80' span, eight-girder, 45° skew series
▸ CXX400	A 120' span, four-girder orthogonal series
▸ CXX800	A 120' span, eight-girder orthogonal series
▸ CXX808	A 120' span, eight-girder, 45° skew series

The span-to-depth ratio was varied from 17 to 24 for the 80' span series and from 17 to 26 for the 120' span series.

The effect of section depth on structural response is plotted in Figures 5.16 through 5.18. Bearing displacements are totally insensitive to section depth under all constraint cases. In contrast, restraint forces at the bearings do increase with increasing span to depth ratio. As was the case with bearing forces versus bridge width, response trends are linear for all three constraint cases. Section depth is observed to exert a greater influence over models with greater width and skew. Under the Traditional constraint case, displacement trends for the two skewed series are parallel, suggesting little coupling between span length and section depth. Greatest bearing forces occur for AXX808, which has the shortest span length and sharpest skew of the models tested. Bearing forces at the extreme values of span to depth ratio differ by 50% for CXX808.

Response trends under the Radial from Corner constraint case are very similar to those under the Traditional constraint case, except that bearing forces for the orthogonal series are proportionately much lower. Again AXX808 exhibits the greatest bearing forces. Under the Radial from Center constraint case, bearing force trends look much different. Data for AXX800 and CXX808 are coincident. In fact, bearing force trends for all the eight-girder series are approximately parallel. It is also observed once more that orthogonal bridges may exhibit greater bearing forces than similar skewed bridges under this constraint case.

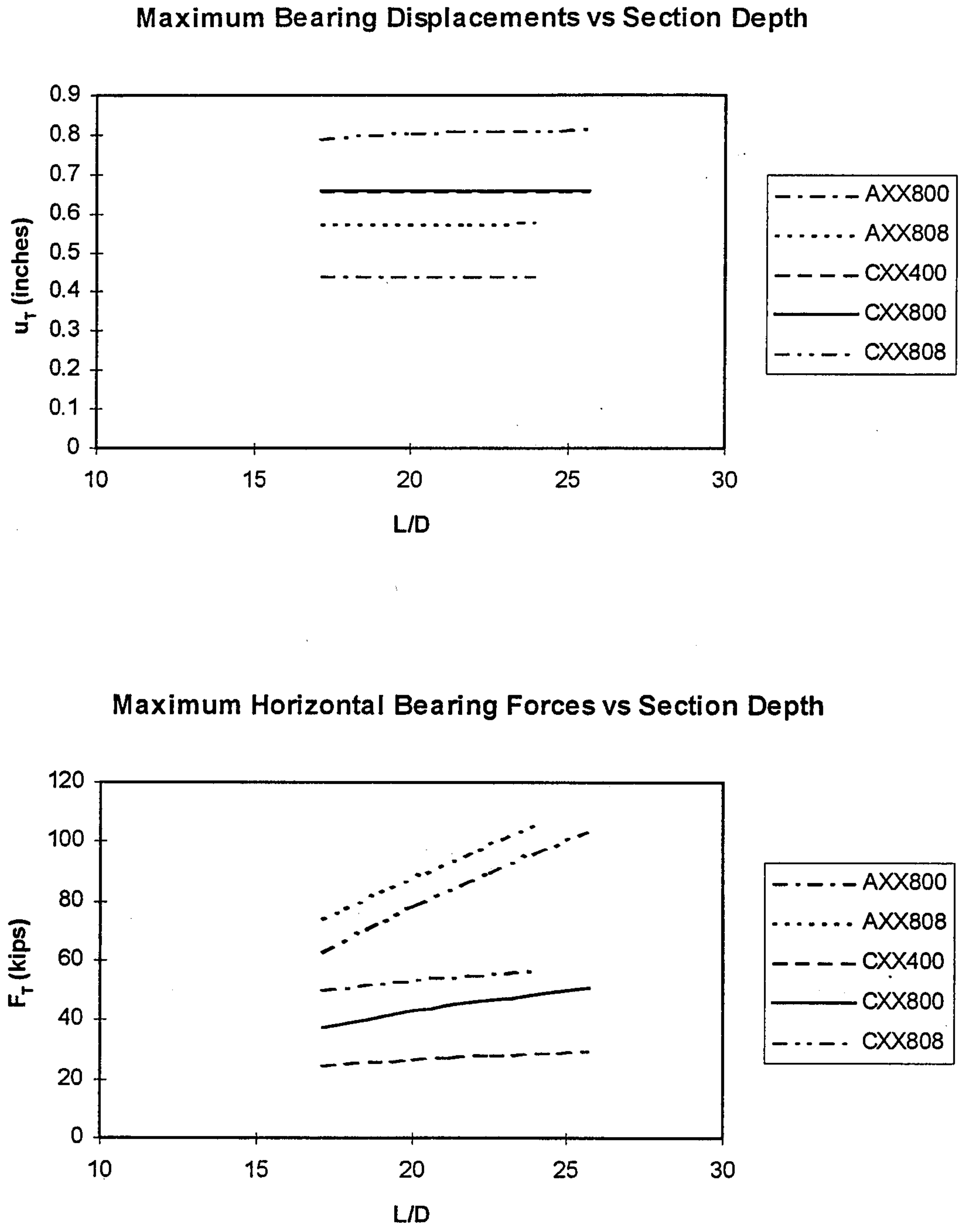

Figure 5.16: Effect of Section Depth Under Traditional Constraint Case

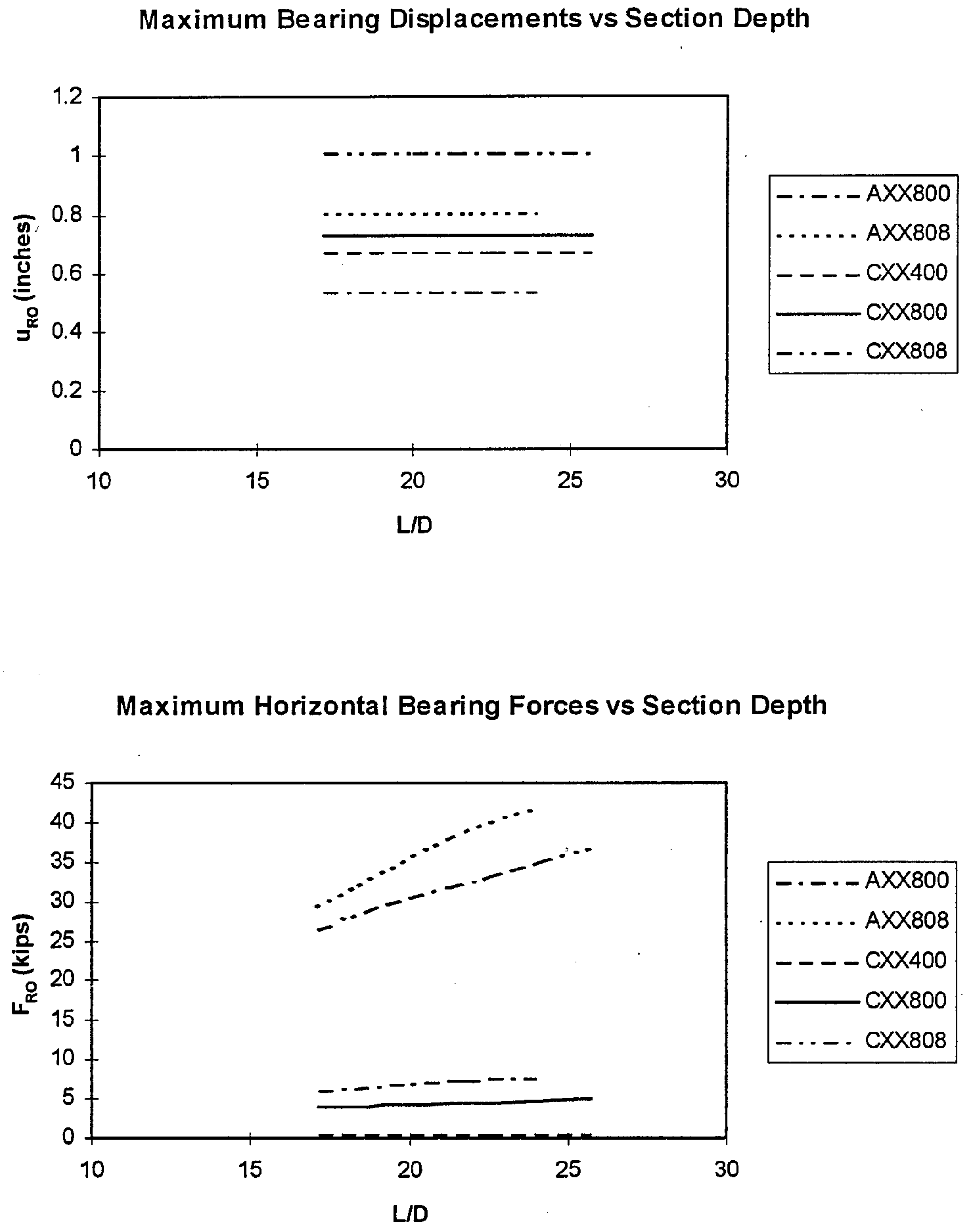

Figure 5.17: Effect of Section Depth Under Radial from Corner Constraint Case

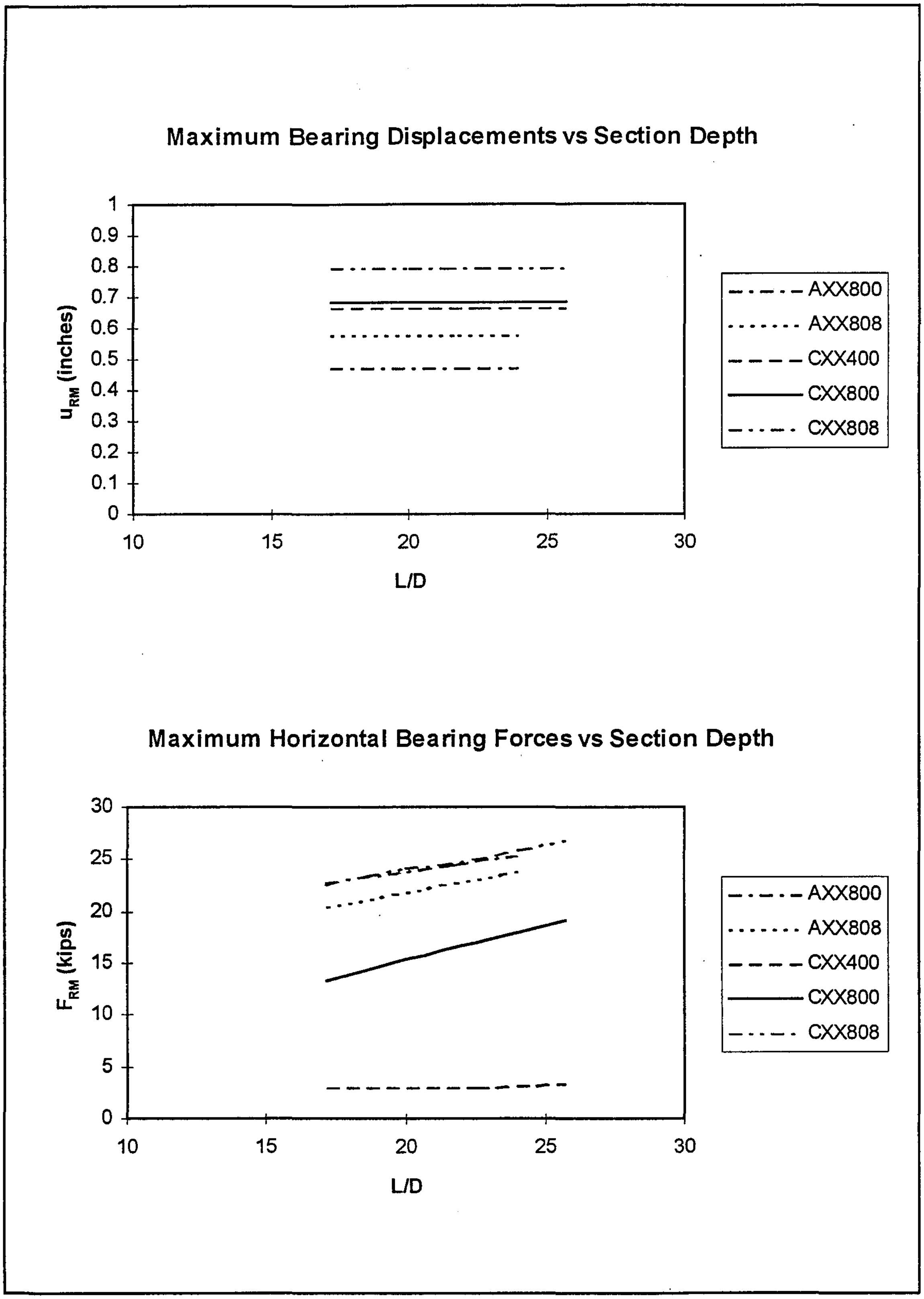

Figure 5.18: Effect of Section Depth Under Radial from Center Constraint Case

CHAPTER 6

DEVELOPMENT OF DESIGN EQUATIONS

6.1 Statistical Basis

Multiple regression analysis may be used to fit experimental data to empirical equations. The general multi-variable regression function has the following form:

$$R = \beta_0 + \beta_1 a_1 + \beta_2 a_2 + \cdots + \beta_n a_n$$

where (6.1)

$$a_i = f_i(x_1, x_2, \ldots, x_k)$$

in which the β_i are coefficients to be determined in the regression analysis, and the a_i are the carriers of the model. The carriers can be any function of the independent variables manipulated in the study. A special form of Equation 6.1 may be used in cases where the dependent variable is linearly related to all of its independent variables. In such cases, the first k carriers are simply the independent variables themselves, and the successive carriers are products of pairs of the independent variables:

$$\begin{aligned} R = \beta_0 + \beta_1 x_1 + \beta_2 x_2 + \cdots + \beta_k x_k + \beta_{k+1} x_1 x_2 + \beta_{k+2} x_1 x_3 + \cdots \\ + \beta_{2k-1} x_1 x_k + \beta_{2k} x_2 x_3 + \cdots + \beta_{3k-3} x_2 x_k + \cdots + \beta_{k+C}\ x_{k-1} x_k \end{aligned} \tag{6.2}$$

This is referred to as the first-order interaction model—*first-order* meaning linear, and *interaction* meaning that coupling effects between the variables may be accounted for.

The coefficients β_i are determined by the method of least squares. The data consists of p ordered sets $(a_{11}, a_{21}, \ldots, a_{n1}, y_1)$, $(a_{12}, a_{22}, \ldots, a_{n2}, y_2)$, $\ldots$, $(a_{1p}, a_{2p}, \ldots, a_{np}, y_p)$, where a_{ij} is the value of the i^{th} carrier associated with the measured value y_j. A measure of error in the model is defined as the sum of the squared deviations between the observed results and the predicted values:

$$f(b_0, b_1, b_2, \ldots, b_n) = \sum_{j=1}^{p} [y_j - (b_0 + b_1 a_{1j} + b_2 a_{2j} + \cdots + b_n a_{nj})]^2 \tag{6.3}$$

The least squares estimates are those values of b_0, b_1, ..., b_n that minimize the error function given by Equation 6.3. Taking partial derivatives of f with respect to each b_i and equating all partials to zero yields the following system of simultaneous linear equations:

$$\begin{array}{llllll}
b_0 p & + b_1 \sum a_{1j} & + b_2 \sum a_{2j} & + \cdots & + b_n \sum a_{nj} & = \sum y_j \\
b_0 \sum a_{1j} & + b_1 \sum a_{1j}^2 & + b_2 \sum a_{1j} a_{2j} & + \cdots & + b_n \sum a_{1j} a_{nj} & = \sum a_{1j} y_j \\
\vdots & & & \vdots & & \vdots \\
b_0 \sum a_{kj} & + b_1 \sum a_{kj} a_{1j} & + b_2 \sum a_{kj} a_{2j} & + \cdots & + b_n \sum a_{kj} a_{nj} & = \sum a_{kj} y_j
\end{array} \tag{6.4}$$

The coefficient estimates β_i^* may then be calculated by Gauss elimination. The asterisk is used to distinguish these least squares approximations from the true values.

The regression functions can contain many terms for relatively few independent variables. Referring to Equation 6.2, for four independent variables, the full first-order interaction model contains 4 + 6 + 1 = 11 carriers. However, the response can usually be described relatively well with only a few carriers, dominant as compared with the others, and the lesser carriers can be eliminated. This is done by a systematic procedure known as the backward elimination method.[8] The *t* ratio is used as a measure of a carrier's dominance in the model, derived from the standardized variable:

$$T_i = \frac{\beta_i^* - \beta_i}{s_{\beta_i^*}} \tag{6.5}$$

where *s* represents estimated standard deviation. This variable has a *t* distribution with $p-(n+1)$ degrees of freedom, so that a $100(1-\alpha)\%$ confidence interval for β_i is given by

$$P\left(-t_{\alpha/2} < T_i < t_{\alpha/2}\right) = 1 - \alpha \tag{6.6}$$

in which $\pm t_{\alpha/2}$ are critical values of the *t* distribution. An α level test of the null hypothesis H_o: $\beta_i = 0$ versus the alternative hypothesis H_a: $\beta_i \neq 0$ is based on Equation 6.6 with β_i assumed equal to zero, in which case T_i is called the *t* ratio. A high absolute *t* ratio means that the interval around $\beta_i = 0$ must extend far in each direction to bound β_i with the specified level of confidence, in other words that H_o should be rejected, and the carrier should be retained in the model.

The elimination is carried out in a stepwise manner. Initially, all carriers are included in the model, and a regression analysis is performed. Coefficient estimates and *t* ratios are calculated for each carrier. The *t* ratios are examined, and the carriers having the smallest absolute *t* ratios are eliminated. Another regression analysis is performed for the reduced model, and again, the lesser carriers are eliminated. The process continues until at some stage, all absolute *t* ratios are suitably large or the model has been reduced to a simple enough form. Appendices D1 and D2 demonstrate the backward elimination method for the Traditional constraint case.

6.2 Equations to Predict Bearing Displacements

In order to use the first-order interaction model given by Equation 6.2, bearing displacements must vary linearly with each independent variable. Figures 5.3 through 5.5 and 5.13 through 5.18 indicate that this holds for span length, bridge width, and section depth. In fact, section depth can be eliminated as a parameter altogether. However, a problem arises when skew angle is considered, as shown in Figures 5.6 through 5.8. Bearing displacements versus skew angle are quite nonlinear for all three constraint cases. This problem was circumvented by employing $\tan\gamma$ as a parameter rather than skew angle itself. Figures 6.1 through 6.3 show that this indeed yields a nearly linear relationship between bearing displacement skew angle.

The equations presented here for bearing displacements were developed exactly in the manner described in the previous section. The substitution of $\tan\gamma$ for skew angle made the first-order interaction model valid. With *L/D* eliminated as a parameter, the full model is given by:

$$u = \beta_0 + \beta_1 L + \beta_2 \tan\gamma + \beta_3 W + \beta_4 L \tan\gamma + \beta_5 L W + \beta_6 W \tan\gamma \tag{6.7}$$

Equation 6.6 served as the starting point in developing design equations for bearing displacements under each constraint case. It was subsequently reduced by the backward elimination procedure. The final form of the equation for each constraint case was selected to balance accuracy versus simplicity. Equations to predict maximum bearing displacements under each constraint case are:

Traditional:

$$u_T = 0.00560L + 0.0001527W\tan\gamma \tag{6.8}$$

Radial from Corner:

$$u_{RO} = 0.00498L + W(0.0001734 + 0.000355\tan\gamma) \tag{6.9}$$

Radial from Center:

$$u_{RM} = 0.00552L + 0.0001664W\tan\gamma \tag{6.10}$$

Figures 6.1 through 6.3 illustrate the degree of fit achieved with these equations. Very close agreement was achieved for all three constraint cases, with coefficients of determination of 0.98 or greater, and root mean square errors of less than 5%. All of these equations were developed using data from all 121 steel bridge models, and are therefore valid over the entire range of the parameters tested. The key carriers affecting maximum bearing displacements were determined to be L, the span length, and $W\tan\gamma$, a term accounting for the combined effect of width and skew. It is noted that an extra term was required to achieve acceptable accuracy for the Radial from Corner constraint case.

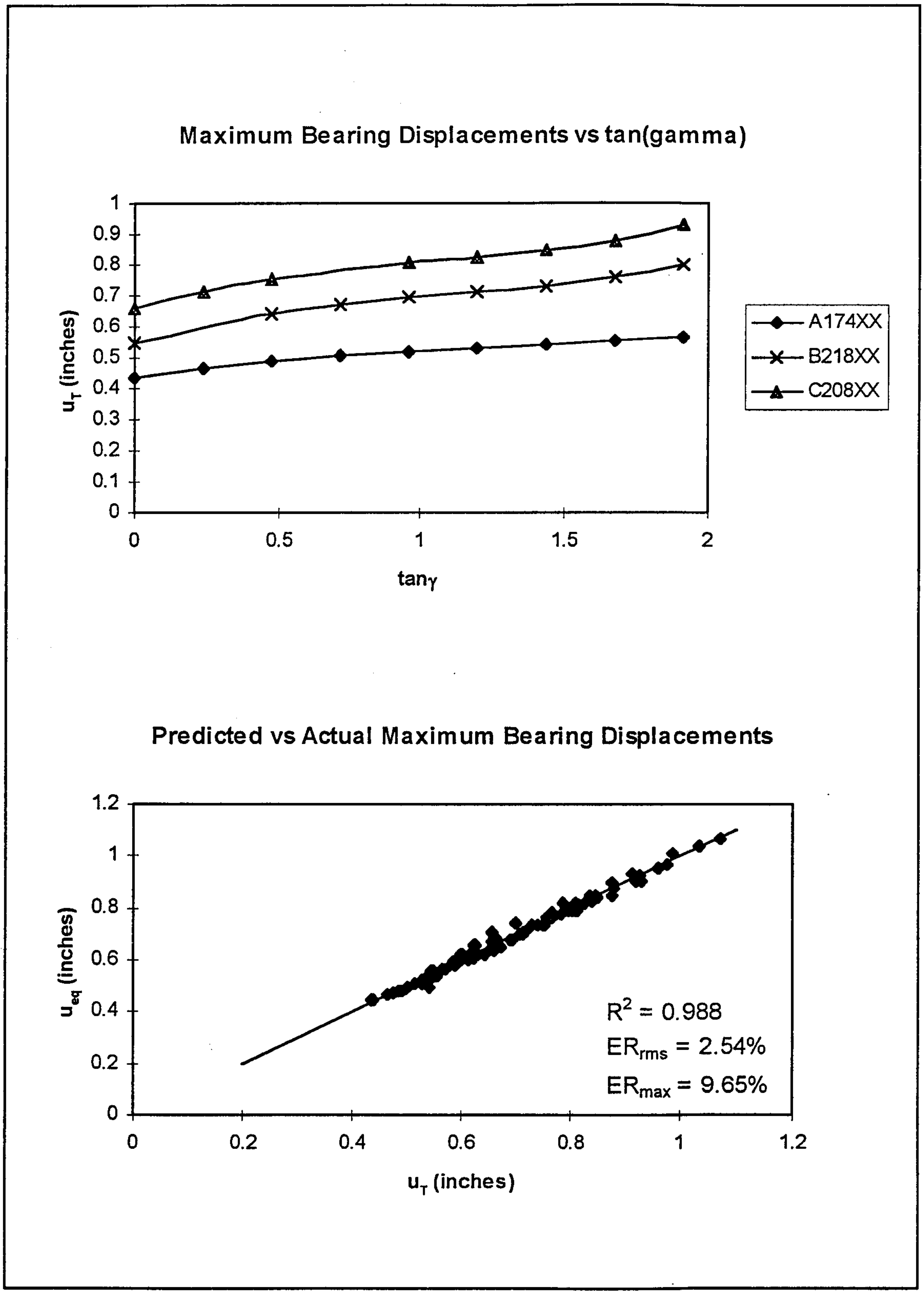

Figure 6.1: Bearing Displacements Under Traditional Constraint Case

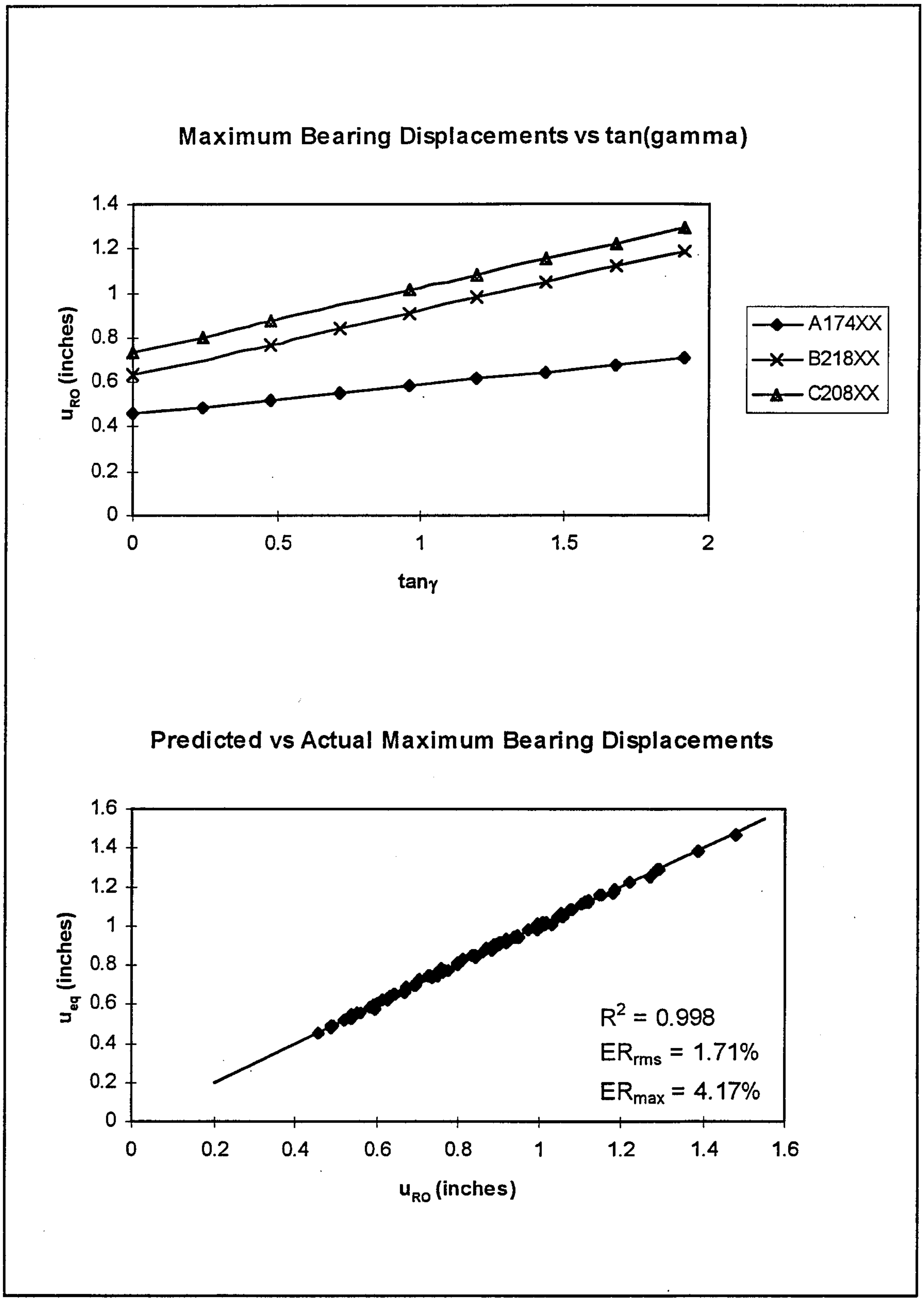

Figure 6.2: Bearing Displacements Under Radial from Corner Constraint Case

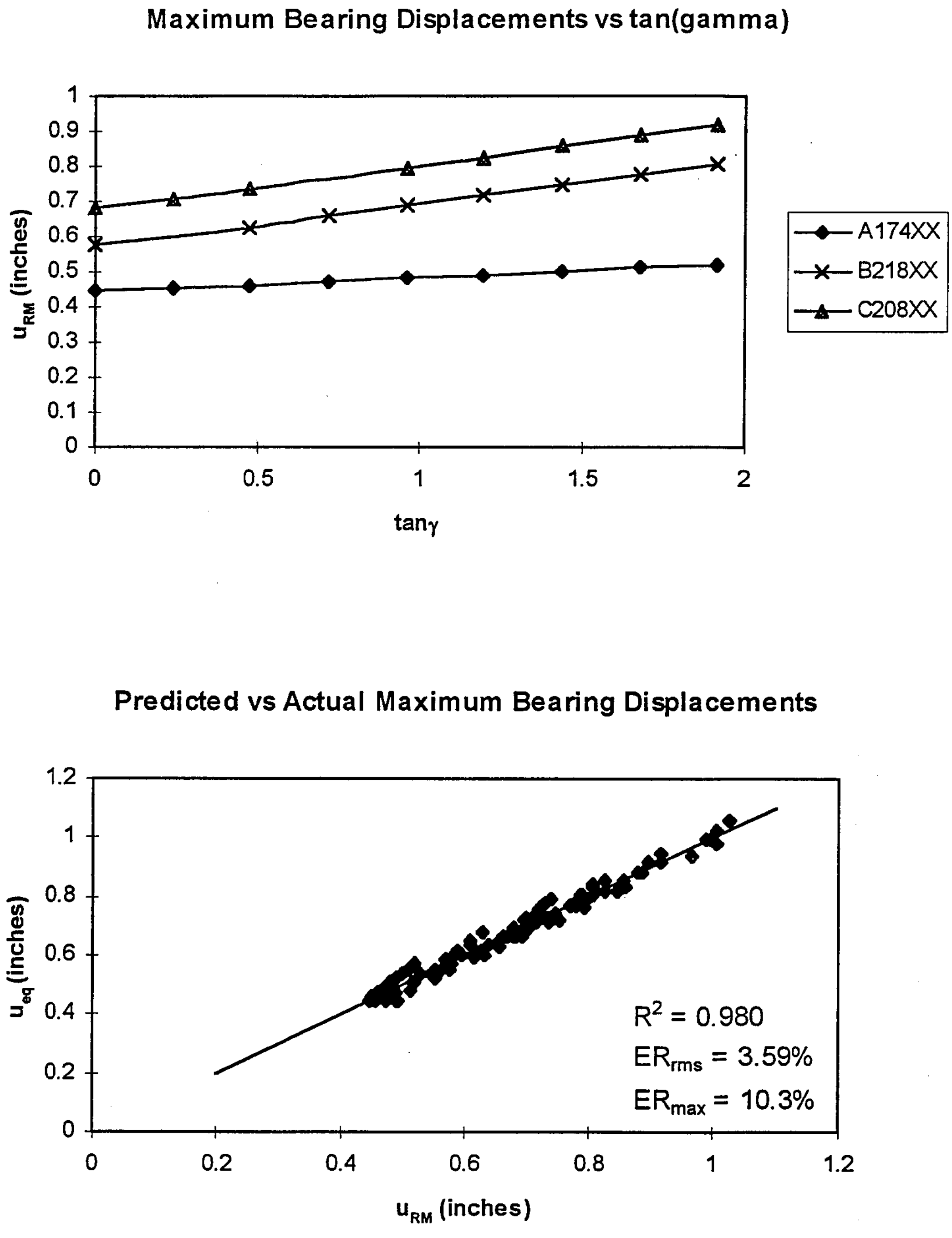
Maximum Bearing Displacements vs tan(gamma)

Predicted vs Actual Maximum Bearing Displacements

Figure 6.3: Bearing Displacements Under Radial from Center Constraint Case

6.3 Equations to Predict Horizontal Bearing Forces

As explained in the previous section, bearing forces must vary linearly with each independent variable in order to apply the first-order interaction model. Figures 5.13 through 5.18 indicate that bearing forces vary linearly with both bridge width and span to depth ratio. Figures 5.3 through 5.5 indicate that bearing forces diminish in an approximately hyperbolic manner with increasing span length. As explained in Section 5.6, this may be handled by introducing *1/L* as a parameter, rendering the relationship linear. As before, skew angle presents a problem, with bearing forces exhibiting highly nonlinear trends for all three constraint cases, as shown in Figures 5.6 through 5.8. In these cases, rather than using a nonlinear functional relationship, such as the exponential and hyperbolic functions shown in the previous chapter, a linear relationship was enforced by employing a function of the skew angle $\psi(\gamma)$ instead of the skew angle itself on the horizontal axis. This ψ-function approach yielded good results, as shown in Figures 6.3 through 6.6.

With response to all parameters linear, equations of the following form were developed through regression analysis for horizontal bearing forces under each constraint case, starting with the full first-order interaction model:

$$\begin{aligned} F = \beta_0 + \beta_1 1/L + \beta_2 \psi + \beta_3 W + \beta_4 L/D + \beta_5 1/L\,\psi + \beta_6 1/L\,W \\ + \beta_7 1/L\,L/D + \beta_8 \psi\,W + \beta_9 \psi\,L/D + \beta_{10} W\,L/D \end{aligned} \qquad (6.11)$$

In the reduction procedure, a slight modification of the backward elimination method was used. The full model was reduced until all carriers had high *t* ratios. Before proceeding with further reduction, triple products of the independent variables were added to the model. Then the reduction process resumed, and a final form was selected. Equations to predict maximum bearing forces under each constraint case are:

Traditional:

$$F_T = -59.3\,\psi/L + 2.88\,W/L + 0.1035\,\psi\,L/D + 0.001577\,W\,L/D$$

where (6.12)

$$\psi = 10(\tan\gamma + \sqrt{\tan\gamma}) + 2.5\tan^3\gamma$$

Radial from Corner:

$$F_{RO} = 0.000399\,W\,L/D + 0.246\,\psi/L\,L/D + 0.00001141\,\psi\,W\,L/D$$

where (6.13)

$$\psi = 0.0001050\gamma^4 - 0.01275\gamma^3 + 0.357\gamma^2 + 2.72\gamma$$

valid for $\gamma > 10°$

Radial from Center:

$$F_{RM} = 25.2\,\psi/L + 0.0334\,\psi\,L/D + 0.000274\,W\,L/D - 1.747\,\psi/L\,L/D$$

where (6.14)

$$\psi = 0.000355\gamma^3 - 0.0631\gamma^2 + 2.82\gamma$$

valid for $10° < \gamma < 55°$

Figures 6.4 through 6.6 illustrate the accuracy of these equations. Coefficients of determination are 0.97 and greater except for the Radial from Center constraint case, and root mean square errors are 10% or less. All parameters tested are determined to significantly affect bearing forces, and no particular parameter can be identified as dominant. The equation for the Traditional constraint case is valid for the entire range of skew angles tested. Equations for the two radial constraint cases have restricted domains. The equation given for the Radial from Corner constraint case may be used for small skew angles, as this gives over-conservative results. The equation given for the Radial from Center constraint case should not be used for skew angles outside of its domain. Maximum bearing forces for small skew angles may be taken as equal to the value calculated for $\gamma = 20°$.

Maximum Horizontal Bearing Forces vs Skew Angle

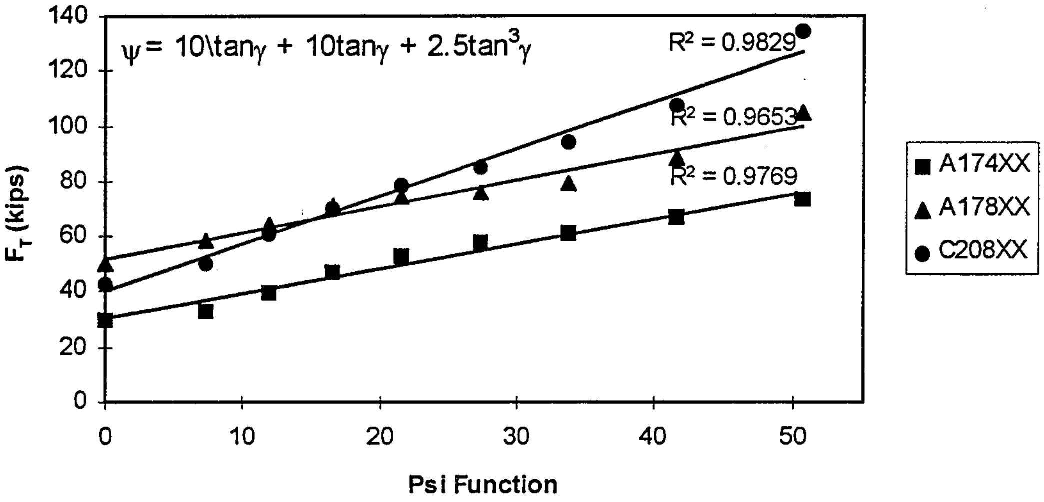

Predicted vs Actual Maximum Horizontal Bearing Forces

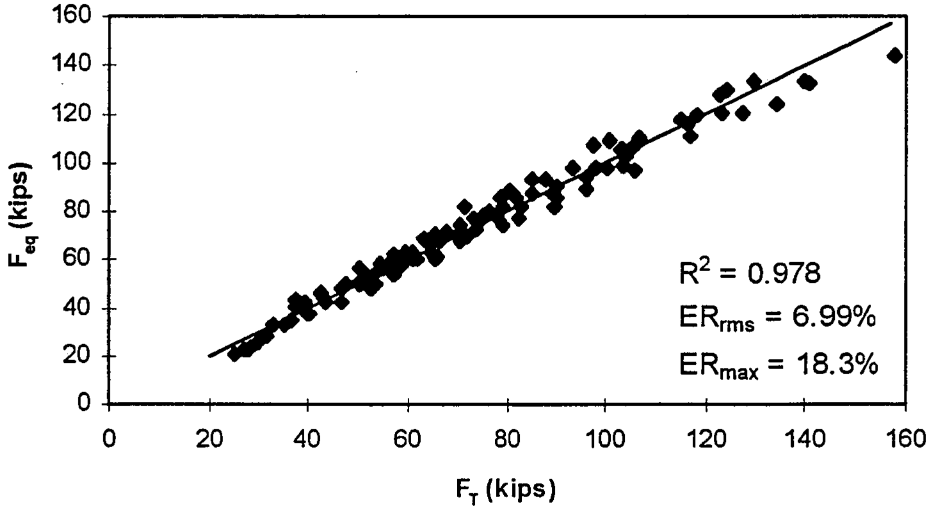

Figure 6.4: Bearing Forces Under Traditional Constraint Case

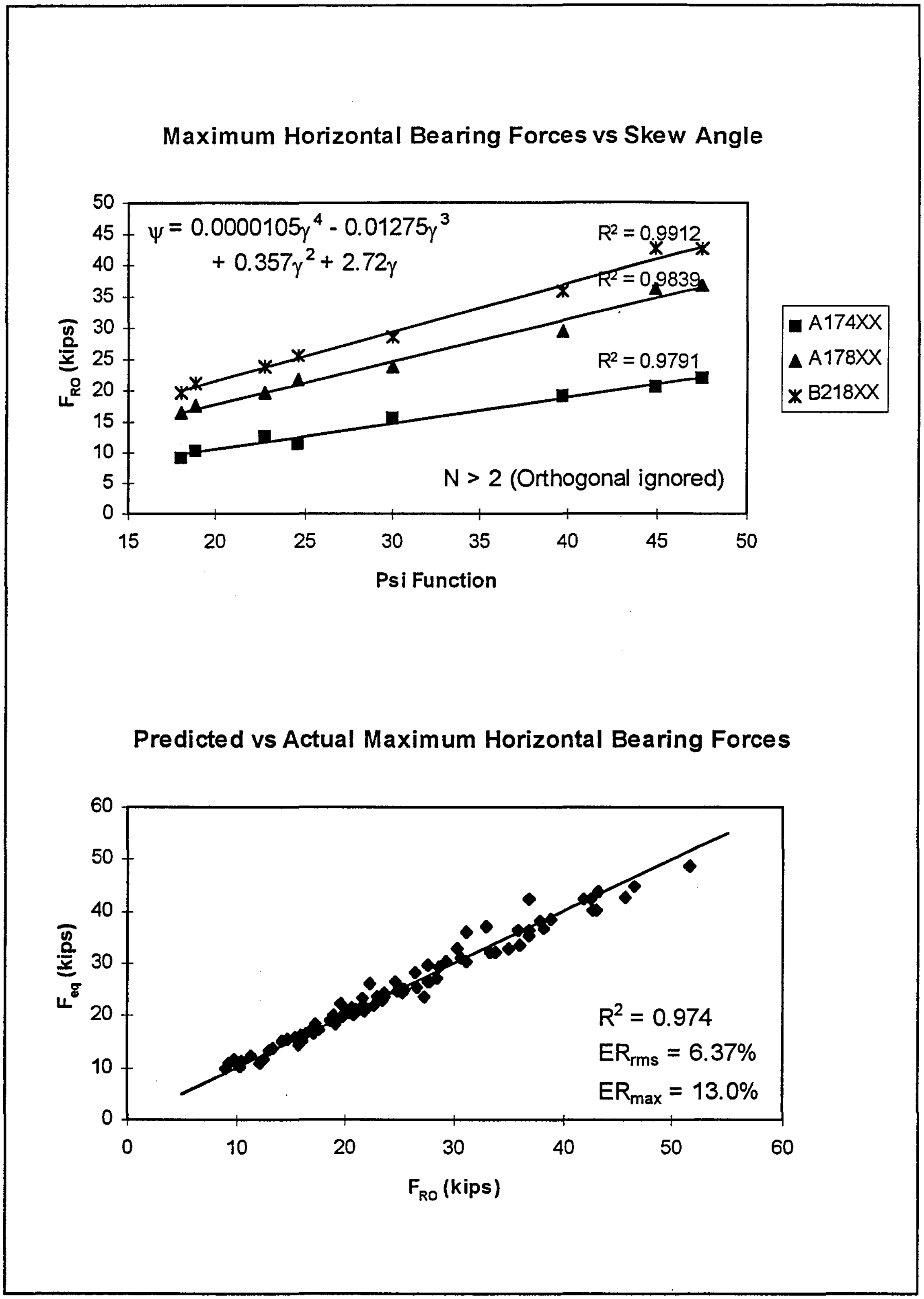

Figure 6.5: Bearing Forces Under Radial from Corner Constraint Case

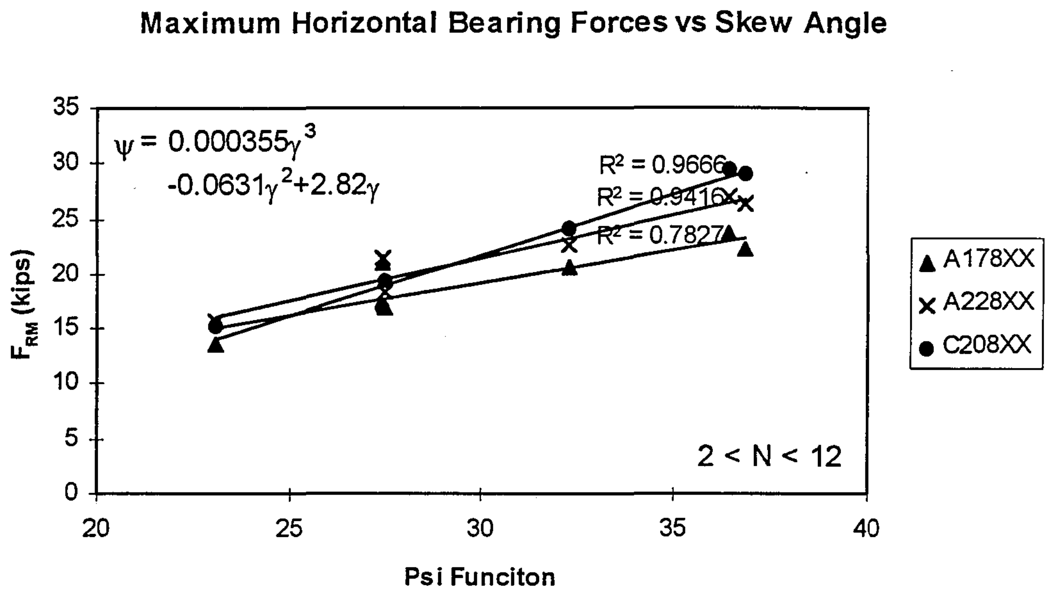
Maximum Horizontal Bearing Forces vs Skew Angle

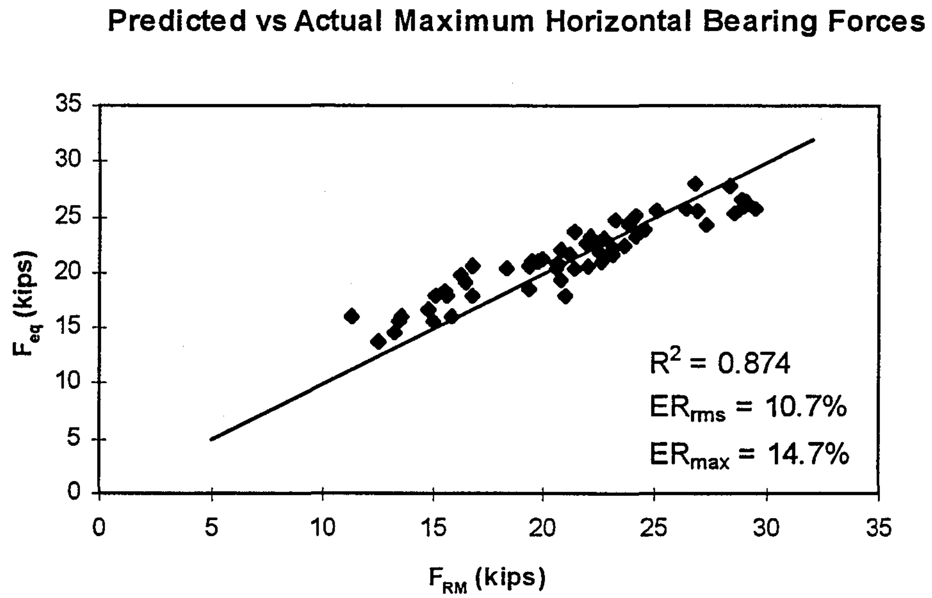
Predicted vs Actual Maximum Horizontal Bearing Forces

Figure 6.6: Bearing Forces Under Radial from Center Constraint Case

6.4 Computational Example

Suppose we are considering a simple span composite steel bridge, or a simply supported segment, with the following parameters:

- $L = 100'$
- $L/D = 20$
- $W = 1000''$ (10 girders spaced at 100")
- $\gamma = 60°$

Initially, we seek to determine the maximum bearing displacement and force magnitudes for the Traditional constraint case. Maximum bearing displacement is determined from Equation 6.8:

$$\begin{aligned} u_T &= 0.00560L + 0.0001527W\tan\gamma \\ &= 0.00560(100) + 0.0001527(1000)\tan 60° \\ &= 0.824\,\text{inches} \end{aligned}$$

Maximum bearing force is determined from Equation 6.12:

$$\psi = 10(\tan\gamma + \sqrt{\tan\gamma}) + 2.5\tan^3\gamma$$

$$\psi = 10(\tan 60° + \sqrt{\tan 60°}) + 2.5\tan^3 60°$$

$$\psi = 43.47$$

$$\begin{aligned} F_T &= -59.3\psi/L + 2.88W/L + 0.1035\psi L/D + 0.001577WL/D \\ &= -59.3(43.47/100) + 2.88(1000/100) \\ &\qquad + 0.1035(43.47)(20) + 0.001577(1000)(20) \\ &= 124.5\,\text{kips} \end{aligned}$$

If we wish to consider one of the radial bearing orientations to avoid the large magnitude of bearing force, the Radial from Corner would be the scheme of choice, since we have a skew angle greater that 55°. Bearing displacement under this constraint case is determined from Equation 6.9:

$$\begin{aligned} u_{RO} &= 0.00498L + W(0.0001734 + 0.000355\tan\gamma) \\ &= 0.00498(100) + 1000(0.0001734 + 0.000355\tan 60^\circ) \\ &= 1.286\,\text{inches} \end{aligned}$$

Maximum bearing force is determined from Equation 6.13:

$$\begin{aligned} \psi &= 0.0001050\gamma^4 - 0.01275\gamma^3 + 0.357\gamma^2 + 2.72\gamma \\ &= 0.0001050(60)^4 - 0.01275(60)^3 + 0.357(60)^2 + 2.72(60) \\ &= 55.2 \end{aligned}$$

$$\begin{aligned} F_{RO} &= 0.000399\,WL/D + 0.246\psi/L\,L/D + 0.00001141\,\psi\,WL/D \\ &= 0.000399(1000)(20) + 0.246(55.2/100)(20) \\ &\qquad + 0.00001141(55.2)(1000)(20) \\ &= 23.3\,\text{kips} \end{aligned}$$

If we select the Radial from Corner bearing orientation, the AASHTO Design Specifications[1] requires that the bearings allow for movement in each direction equal to twice the amount of contraction plus one inch, or 2(1.286) + 1 = 3.57 inches. Further, they must be capable of resisting either the designated horizontal design load or 10% of the vertical design load applied horizontally in any direction, whichever is greater.

CHAPTER 7

CONCRETE BRIDGE THERMAL RESPONSE

7.1 Hypothetical Bridge Designs

Hypothetical concrete bridges were developed to evaluate the effect of the test parameters, and to compare response magnitudes with those determined for similar steel bridges. The bridge sections consisted of prestressed AASHTO I-girders composite with a cast-in-place concrete deck. Two basic designs were selected using a PCI design chart:[20]

- AASHTO Type III girders spanning 60'
- AASHTO Type IV girders spanning 80'

Prestress forces required for the HS20-44 truck loading with impact are 470 kips for the 60' span and 725 kips for the 80' span. Girder spacing and slab thickness were the same as for the steel bridges to allow direct comparison of the analysis results. Eight-inch cast-in-place diaphragms were used for both designs. These were placed at 20' intervals as was done for the steel bridges. For each basic design, width and skew were varied as described for the steel bridges. Materials used were 5000 psi compressive strength concrete for the girders, and 4000 psi concrete for the deck. Table 7.1 gives physical properties of the girder and deck concrete. The slightly lower coefficient of thermal expansion α_{pc} for the girder is suggested for higher strength concrete.[14] Elastic moduli

Table 7.1: Properties of Concrete Bridge Materials

Property	Units	Girder			Deck		
Elastic Modulus	psi	E_{pc}	=	4,000,000	E_c	=	3,600,000
Poisson's Ratio	N/A	ν_{pc}	=	0.20	ν_c	=	0.18
Weight Density	lb/ft³	ρ_{pc}	=	150	ρ_c	=	150
Thermal Expansivity	in/in/°F	α_{pc}	=	0.0000055	α_c	=	0.0000060
Compressive Strength	psi	f_{pc}'	=	5000	f_c'	=	4000

and Poisson's ratios were calculated by the same empirical formulas given in Section 4.1.

7.2 Finite Element Models

The finite element models were prepared much in the same manner as before. Figure 7.1 shows a typical finite element model. As the AASHTO girders do not have pronounced flanges like the thin-walled steel I-sections, the whole girder was modeled as a single plate of varying thickness, meshed with CQUAD4 quadrilateral shell elements. NASTRAN allows the CQUAD4 elements to have linearly varying thickness over area

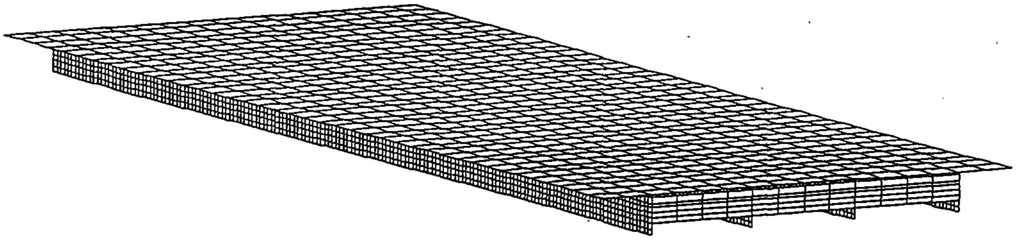

Figure 7.1: Typical Finite Element Model

of the element. The girders were divided into separate elements through the depth at changes in thickness, except that the thin central portion of the web was divided into thirds to maintain an approximately uniform element division. The diaphragms and deck were also meshed with CQUAD4 elements. Four elements were used across the width to maintain moderate aspect ratios. Rigid link elements joined the deck to the girders at every node along the span.

7.3 Temperature Loading

The temperature loadings used for the concrete bridges was adapted from the AASHTO Guide Specifications for Concrete Bridges[14] and the New Zealand Ministry of Works Specifications. These loadings were intended to represent actual temperatures a concrete bridges would experience if subjected to the same environmental conditions which produce the assumed temperature distributions in the steel bridges. According to the AASHTO Guide Specifications, under ambient temperatures which correspond to mean temperatures of 0° and 120° for steel bridges, a concrete bridge will experience

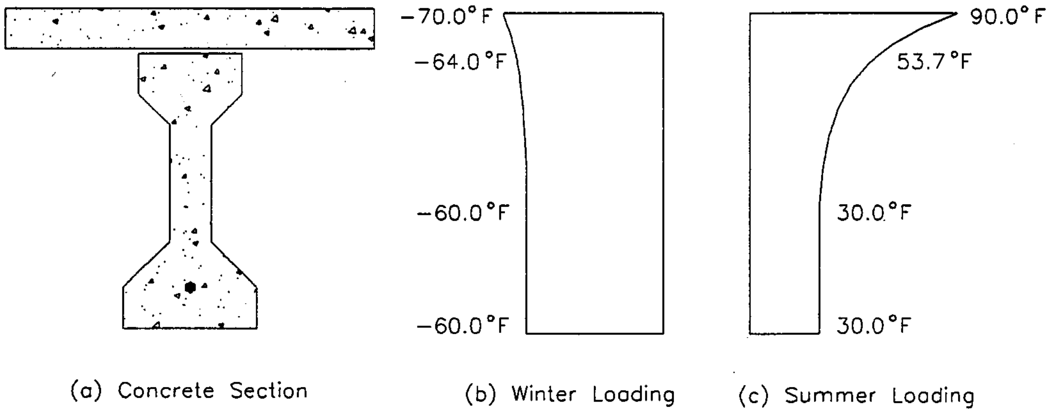

Figure 7.2: Temperature Loading for Concrete Bridge Models

mean temperatures of 10° and 100°, respectively. This means that for the same setting temperature of 70°F, the concrete bridge will experience a temperature rise of +30°F in the summer and a temperature fall of -60°F in the winter. The magnitude of the positive gradient is based on the fact that for deck surfaces of the same type under equal intensity of solar radiation and hours of sunlight, maximum surface temperatures should be equal for any bridge section. As the maximum surface temperature was taken to be +90°F for the steel bridges, a concrete bridge would realize this same value if both were plain concrete wearing surfaces. The New Zealand fifth-order curve with T_{max} = 90°F - 30°F = 60°F was used to define the temperature gradient between the constant temperature in the lower part of the section and the maximum temperature at the surface. The negative gradient also used the New Zealand fifth-order curve with T_{max} = -10°. The total temperature loadings are shown in Figure 7.2.

7.4 Concrete Bridge Response

A set of twenty bridge models was used to investigate structural response of concrete bridges. The same nomenclature system is used here as was developed for the steel bridge models. The sections *CS6* and *CS8* are the AASHTO Types III and IV, respectively. Four series of models were tested in this study:

▸	CS66XX	A 60' span, six-girder series (AASHTO III)
▸	CS84XX	An 80' span, four-girder series (AASHTO IV)
▸	CS86XX	An 80' span, six-girder series (AASHTO IV)
▸	CS88XX	An 80' span, eight-girder series (AASHTO IV)

As before, skew angle was varied from 0° to 63°.

Structural response with increasing skew angle is plotted in Figures 7.3 through 7.5. Bearing displacement trends have identical shapes to those for the steel bridges, only at lesser magnitudes. Displacements do increase with increasing skew angle. For the two radial constraint cases, displacements increase more sharply toward the higher end of the range. It is also observed that displacements increase with longer span lengths and greater widths. The greatest displacements under each constraint case are 0.4958, 0.8730, and 0.5532, respectively.

Bearing force trends also have similar shapes to those for the steel bridges. It is observed, however, that bearing forces increase much faster with increasing skew for the concrete bridges. Again, greatest bearing forces occur under the Traditional constraint case. Bearing forces under the two radial constraint cases are comparatively much higher than for the steel bridges. Larger bearing forces occur for shorter span lengths and greater widths, as before.

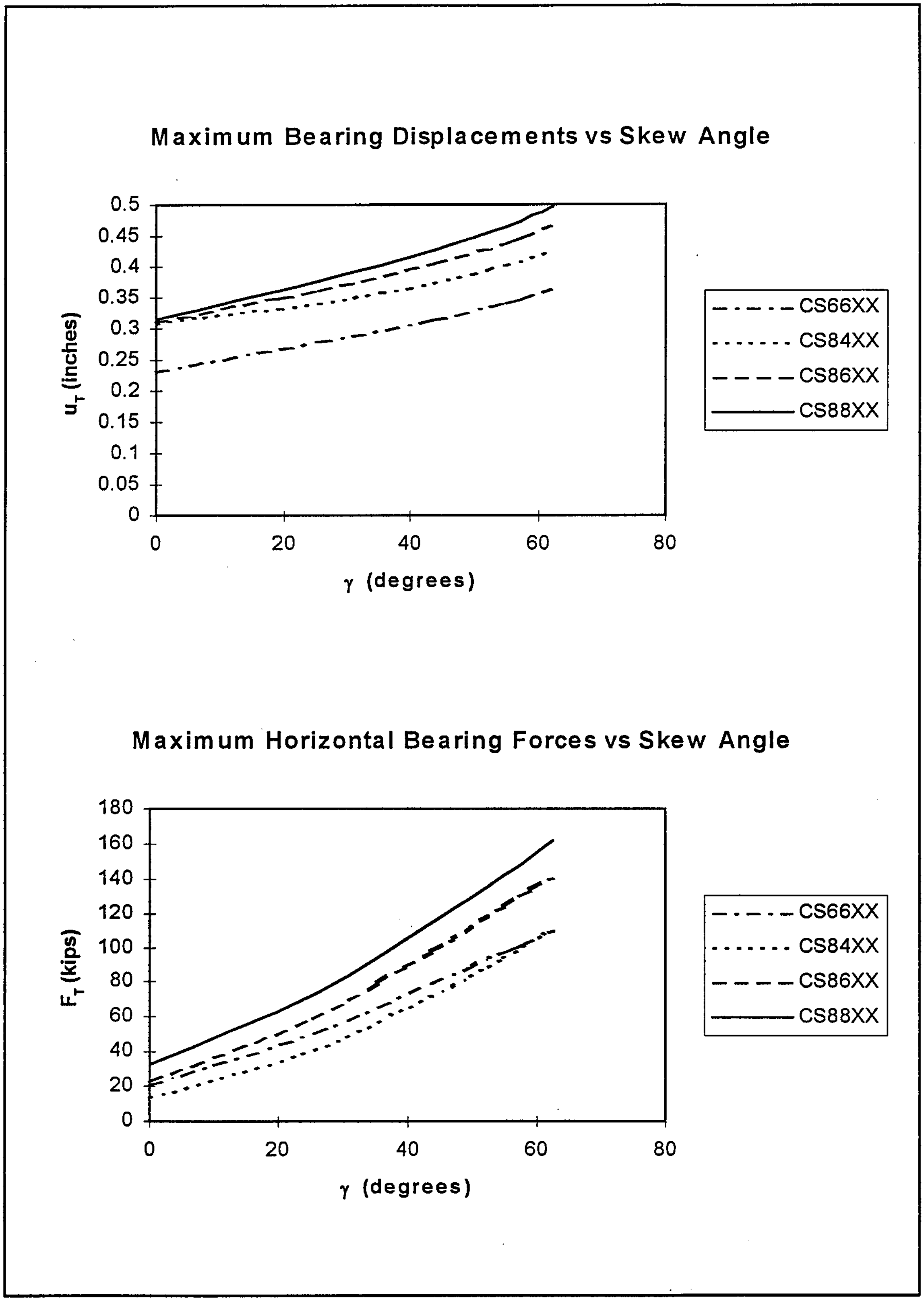

Maximum Bearing Displacements vs Skew Angle

Maximum Horizontal Bearing Forces vs Skew Angle

Figure 7.3: Concrete Bridge Response Under Traditional Constraint Case

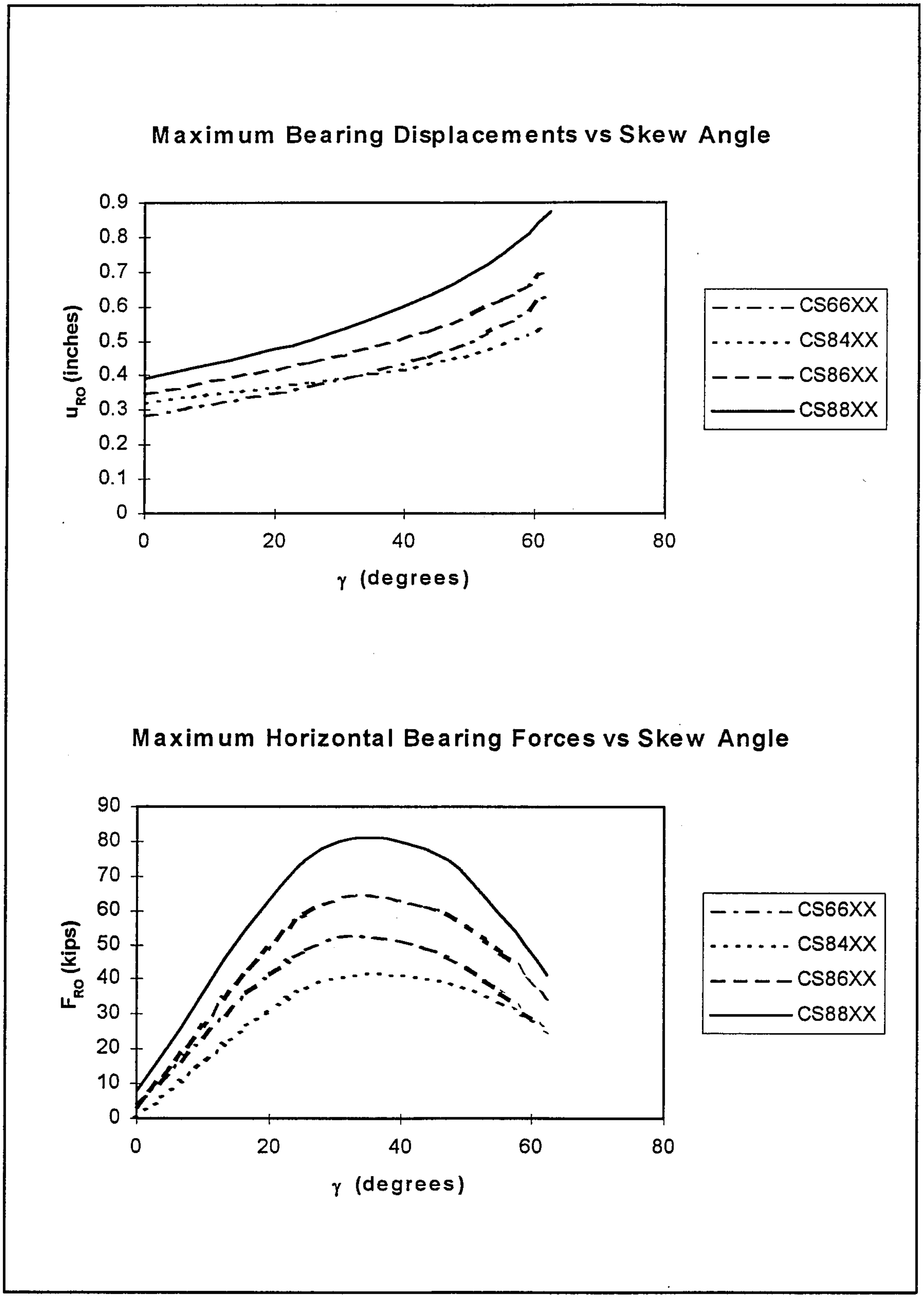

Figure 7.4: Concrete Bridge Response Under Radial from Corner Constraint Case

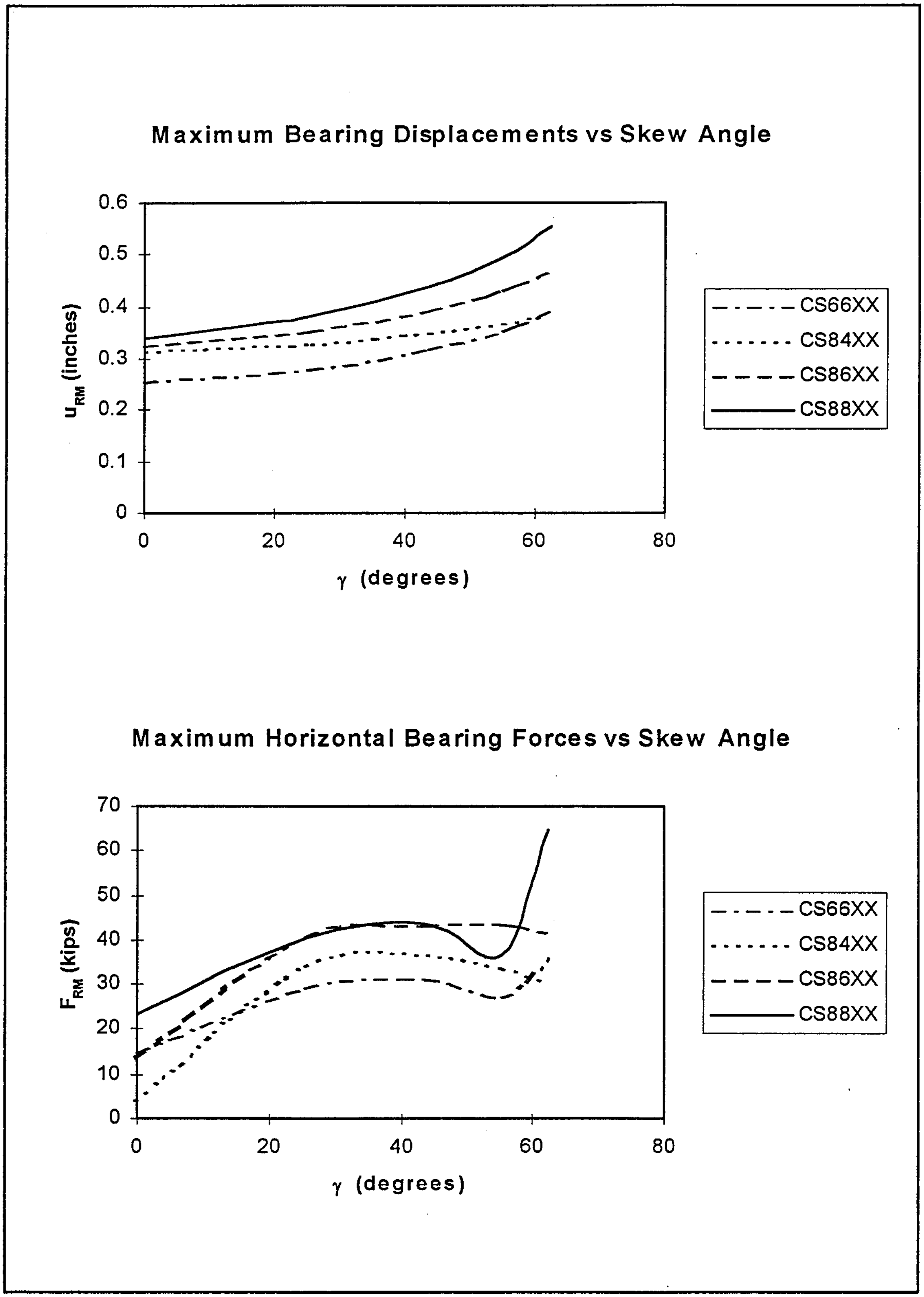
Maximum Bearing Displacements vs Skew Angle

Maximum Horizontal Bearing Forces vs Skew Angle

Figure 7.5: Concrete Bridge Response Under Radial from Center Constraint Case

7.5 Comparison with Steel Bridge Response

Table 7.2 contains sample comparison data of maximum bearing displacements and forces for steel and concrete bridges. The values given for steel bridges are those predicted by the design equations presented in Chapter 6. The ratio of concrete bridge to steel bridge response is also tabulated. The following inferences can be made by examining the "Ratio" column of the table:

1.) Very strong correlation exists between maximum bearing displacements for the steel and concrete bridges.

2.) Maximum bearing displacements for a concrete bridge may be well approximated as 75% of those calculated by the design equations given for steel bridges.

3.) Bearing forces are consistently higher for the concrete bridges than for the steel bridges. This is especially true for the two radial constraint cases, where the ratio can be as high as 3 or 4.

4.) Bearing forces for concrete bridges increase much more rapidly with increasing skew than for similar steel bridges under all three constraint cases.

Table 7.2: Comparison of Steel and Concrete Bridge Thermal Responses

		Model	Steel	Concrete	Ratio
Maximum Bearing Displacements (inches)	Traditional Constraint Case	CS6604	0.3800	0.2782	0.73
		CS6608	0.4240	0.3144	0.74
		CS6612	0.4679	0.3422	0.73
		CS8804	0.5066	0.3762	0.74
		CS8808	0.5653	0.4258	0.75
		CS8812	0.6239	0.4642	0.74
	Radial from Corner Constraint Case	CS6604	0.5051	0.3690	0.73
		CS6608	0.6073	0.4576	0.75
		CS6612	0.7096	0.5456	0.77
		CS8804	0.6734	0.5047	0.75
		CS8808	0.8098	0.6281	0.78
		CS8812	0.9461	0.7511	0.79
	Radial from Center Constraint Case	CS6604	0.3791	0.2793	0.74
		CS6608	0.4270	0.3170	0.74
		CS6612	0.4750	0.3544	0.75
		CS8804	0.5055	0.3828	0.76
		CS8808	0.5694	0.4390	0.77
		CS8812	0.6333	0.4950	0.78
Maximum Bearing Forces (kips)	Traditional Constraint Case	CS6604	46.67	67.22	1.44
		CS6608	50.68	105.28	2.08
		CS6612	55.80	130.24	2.33
		CS8804	58.67	97.16	1.66
		CS8808	66.95	152.21	2.27
		CS8812	77.50	189.56	2.45
	Radial from Corner Constraint Case	CS6604	23.31	64.68	2.77
		CS6608	20.95	65.71	3.14
		CS6612	13.40	48.01	3.58
		CS8804	30.43	99.85	3.28
		CS8808	27.42	103.71	3.78
		CS8812	17.83	77.83	4.36
	Radial from Center Constraint Case	CS6604	19.83	38.98	1.97
		CS6608	17.67	41.81	2.37
		CS6612	13.27	36.21	2.73
		CS8804	21.58	53.68	2.49
		CS8808	19.34	58.39	3.02
		CS8812	14.80	49.12	3.32

CHAPTER 8

CONCLUSIONS

Having accomplished the objectives stated in the Introduction, some of the more important conclusions are highlighted here:

1.) The empirical equations developed through multiple linear regression analysis proved capable of predicting displacement and restraint force at the bearings with considerable accuracy.

2.) While the Traditional bearing orientation may be preferred for some narrow bridges with slight skews, bearing forces are substantially reduced for the radial bearing orientations.

3.) Skewed bridges exhibit large bearing forces in the longitudinal direction under the Traditional constraint case, which may explain the observed tendency for these bridges to rotate on their supports.

4.) The Traditional and Radial from Center constraint cases yield roughly equal magnitudes of bearing displacement. Displacements under the Radial from Corner constraint case range from 5 to 10% higher for orthogonal bridges to 35% higher for skews near 65°.

5.) The Radial from Corner constraint case performs best for skews less than 20° and greater than 55°. The Radial from Center constraint case is better suited for intermediate values of skew angle.

6.) Under the Traditional and the Radial from Corner constraint cases, maximum bearing force always occurs at the first girder in the acute angle of the fixed end of the bridge. This is not always the case for the Radial from Center constraint case.

7.) Bearing displacements increase linearly with increasing span length. Span length is not coupled with any of the other geometric parameters with regard to bearing displacements.

8.) Bearing forces decrease in inverse proportion to span length. In some cases, bearing forces diminish by 20% or more when span length is doubled from 80' to 160'.

9.) Bearing displacements increase parabolically with increasing skew angle. This trend appears linear when plotted against tangent of skew angle. Under the Traditional and Radial from Center constraint cases, bearing displacement for a bridge skewed at 60° may be 40% higher than for a similar orthogonal bridge. Under the Radial from Corner constraint case, bearing displacement may be 100% higher.

10.) Bearing forces increase exponentially with increasing skew angle under the Traditional constraint case. Under the Radial from Corner constraint case, bearing forces trace a bell-shaped pattern with maximum values occurring near 30° skew. Wider bridges may experience very high bearing forces under the Radial from Center constraint case for skew angles less than 20° or greater than 55°.

11.) Bearing displacements and forces increase linearly with bridge width, although not in direct proportion.

12.) Under the Traditional constraint case, bearing forces increase by a constant amount for all widths with increasing skew. Under the two radial constraint cases, significant coupling is evident between width and skew.

13.) Bearing displacements are not affected by section depth. Bearing forces sometimes differ by 50% for the extreme span to depth ratios of 17 and 26.

14.) Bearing displacements for a concrete bridge may be well approximated as 75% of those which would be expected for a similar steel bridge.

15.) Bearing forces are consistently higher for the concrete bridges than for the steel bridges. This is especially true for the two radial constraint cases, where the ratio can be as high as 3 or 4.

16.) Bearing forces for concrete bridges increase much more rapidly with increasing skew than for similar steel bridges under all three constraint cases.

As suggested areas for future research into thermal effects on highway bridges, the author suggests the following:

1.) Parametric studies of curved bridges similar to those presented here for skewed bridges.

2.) A study of multi-span bridges to include the flexibility of tall piers used as the fixed point of support.

3.) A study to incorporate the effect of girder spacing and slab thickness on the thermal response of composite steel bridges.

4.) Non-linear analysis accounting for the effects of friction in the bearings.

BIBLIOGRAPHY

1. *AASHTO LRFD Bridge Design Specifications, 1st Edition*, The American Association of State Highway and Transportation Officials, Washington, D.C., 1994.

2. *AASHTO Standard Specifications for Highway Bridges, 15th Edition,* The American Association of State Highway and Transportation Officials, Washington, D.C., 1992.

3. Barber, E. S., "Calculation of Maximum Pavement Temperatures from Weather Reports," *Highway Research Board Bulletin 168*, 1957.

4. Berwanger, C., "Thermal Stresses in Composite Beams," *Journal of the Institute of Structural Engineers*, April 1974.

5. Branco, Fernando A. and Mendes, Pedro A., "Thermal Actions for Concrete Bridge Design," *Journal of Structural Engineering*, ASCE, Volume 119, Number 8, August, 1993.

6. Churchward, Allan and Sokal, Yehuda J., "Prediction of Temperatures in Concrete Bridges," *Journal of the Structural Division*, ASCE, Volume 107, Number ST11, November, 1981

7. Cook, Robert D., Malkus, and Plesha, *Concepts and Applications in Finite Element Analysis, 3rd Edition*, John Wiley and Sons, Inc., New York, NY, 1989.

8. Devore, Jay L., *Probability and Statistics for Engineering and the Sciences, 3rd Edition*, Brooks/Cole Publishing Company, Pacific Grove, California, 1991.

9. Elbadry, Mamdouh M. and Ghali, Amin, "Temperature Variations in Concrete Bridges," *Journal of Structural Engineering*, ASCE, Volume 109, Number 10, October, 1983.

10. Emanuel, Jack H. and Lewis, A. M., "Abutment-Thermal Interaction of Composite Bridge," *Journal of the Structural Division*, ASCE, Volume 107, Number ST11, November, 1981.

11. Gatewood, B. E., *Thermal Stresses*, McGraw-Hill Publications in Aeronautical Science, New York, 1957.

12. Hoffman, P. C., McClure, R. M., and West, H. H., "Temperature Study of an Experimental Segmental Concrete Bridge," *PCI Journal*, March-April 1983.

13. Hunt, Bruce and Cooke, Nigel, "Thermal Calculations for Bridge Design," *Journal of the Structural Division*, ASCE, Volume 101, Number ST9, September, 1975.

14. Imbsen, R. A., Vandershaf, Shcamber, and Nutt, "Thermal Effects in Concrete Bridge Superstructures," *Transportation Research Record 276*, September 1985.

15. Kennedy, John B. and Soliman, Mohamed H., "Temperature Distribution in Composite Bridges," *Journal of Structural Engineering*, ASCE, Volume 113, Number 3, March, 1987.

16. Lee, David J., *Bridge Bearings and Expansion Joints*, E & FN Spon Publications, New York, New York, 1994.

17. MacNeal, Richard H., *Finite Elements: Their Design and Performance*, Marcel Dekker, Inc., New York, New York, 1994.

18. Moorty, Shashi and Roeder, Charles W., "Temperature-Dependent Bridge Movements," *Journal of Structural Engineering*, ASCE, Volume 118, Number 4, April, 1992.

19. *MSC/NASTRAN Reference Manual*, Version 68, Volume I, II, III, The MacNeal-Schwendler Corporation, Los Angeles, California, 1994.

20. Naaman, Antoine E., "A Computer Program for Selection and Design of Simple Span Prestressed Concrete Highway Girders," *PCI Journal*, Volume 17, Number 1, January-February 1972.

21. *NASTRAN Theoretical Manual*, Richard H. MacNeal editor, The MacNeal-Schwendler Corporation, Los Angeles, California, December 1972.

22. Pentas, Herodotos A., Avent, R. Richard, Gopu, Vijaya, K. A., and Rebello, Keith J., "Field Study of Bridge Temperatures in Composite Bridges," *Transportation Research Record 1460*, 1994.

23. Pentas, Herodotos A., Avent, R. Richard, Gopu, Vijaya, K. A., and Rebello, Keith J., "Field Study of Longitudinal Movements in Composite Bridges," *Transportation Research Record 1476*, 1995.

24. Potgieter, Izak C. and Gamble, William L., "Nonlinear Temperature Distributions in Bridges at Different Locations in the United States," *PCI Journal*, July-August 1989.

25. *Precast Segmental Box Girder Bridge Manual*, Prestressed Concrete Institute, Chicago, Illinois and Post-Tensioning Institute, Phoenix, Arizona, 1978.

26. Radolli, M. and Green, R., "Thermal Stresses in Concrete Bridge Superstructures Under Summer Conditions," *Transportation Research Board 547*, 1975.

27. "Room for Improvement," *Engineering News-Record*, Volume 164, Number 5, February 4, 1960.

28. Steward, C.F., "Annual Movement Study of Bridge Deck Expansion Joints," *R&D Report No. 2-69*, California Division of Highways, June 1969.

29. Thepchatri, T., Johnson, C. P., and Matlock, H., "Prediction of Temperature and Stresses in Highway Bridges by a Numerical Procedure Using Daily Weather Reports," *Research Report 23-1*, Center for Highway Research, University of Texas at Austin, February, 1977.

30. *USS Highway Structures Design Handbook*, Volume II, AISC Marketing, Inc., American Institute of Steel Construction, 1986.

31. Will, K. M., Johnson, C. P., and Matlock, H., "Analytical and Experimental Investigation of the Thermal Response of Highway Bridges," *Research Report 23-2*, Center for Highway Research, University of Texas at Austin, February, 1977.

32. Zuk, William, "Thermal and Shrinkage Stresses in Composite Beams," *ACI Journal*, Volume 58, Number 3, September 1961.

33. Zuk, William, "Thermal Behavior of Composite Bridges - Insulated and Uninsulated," *Highway Research Record*, Number 76, 1965.

APPENDIX A

I-Girder Cross-Sectional Dimensions for Steel Bridge Designs

Section ID	Top Flange		Web		Bottom Flange		
	b_f	t_c	h_w	t_w	b_f	t_1	t_2
A17	12	5/8	48	3/8	12	9/16	1
A22	12	5/8	36	5/16	12	1	1 5/8
A24	12	5/8	32	5/16	12	1	1 7/8
B21	12	5/8	48	3/8	12	1	1 5/8
C17	12	5/8	76	1/2	12	9/16	1
C18	12	5/8	72	1/2	12	5/8	1 1/8
C20	12	5/8	64	7/16	12	7/8	1 1/2
C21	12	5/8	60	7/16	12	1	1 3/4
C23	12	3/4	56	3/8	12	1 1/8	2
C26	12	1	48	3/8	12	1 3/8	2 3/8
D25	18	15/16	60	7/16	18	7/8	1 1/2
E24	18	15/16	72	1/2	18	1	1 5/8
F24	18	15/16	84	9/16	18	1	1 3/4

APPENDIX B

Steel Bridge Model Geometric Parameters

Model ID	Section ID	Span Length	Span to Depth Ratio	Number of Girders	Skew Angle
VS1-1-1	A22	80'	21.82	4	0°
VS1-1-2	B21	100'	21.43	4	0°
VS1-1-3	C21	120'	21.18	4	0°
VS1-1-4	D25	140'	24.71	4	0°
VS1-1-5	E24	160'	24.00	4	0°
VS1-1-6	F24	180'	23.48	4	0°
VS1-2-1	A22	80'	21.82	4	25°
VS1-2-2	B21	100'	21.43	4	25°
VS1-2-3	C21	120'	21.18	4	25°
VS1-2-4	D25	140'	24.71	4	25°
VS1-2-5	E24	160'	24.00	4	25°
VS1-2-6	F24	180'	23.48	4	25°
VS1-3-1	A22	80'	21.82	4	45°
VS1-3-2	B21	100'	21.43	4	45°
VS1-3-3	C21	120'	21.18	4	45°
VS1-3-4	D25	140'	24.71	4	45°
VS1-3-5	E24	160'	24.00	4	45°
VS1-3-6	F24	180'	23.48	4	45°
VS1-4-1	A22	80'	21.82	6	0°
VS1-4-2	B21	100'	21.43	6	0°
VS1-4-3	C21	120'	21.18	6	0°
VS1-4-4	D25	140'	24.71	6	0°

Model ID	Section ID	Span Length	Span to Depth Ratio	Number of Girders	Skew Angle
VS1-4-5	E24	160'	24.00	6	0°
VS1-4-6	F24	180'	23.48	6	0°
VS2-1-1	A17	80'	17.14	4	0°
VS2-1-2	A17	80'	17.14	4	13°
VS2-1-3	A17	80'	17.14	4	25°
VS2-1-4	A17	80'	17.14	4	35°
VS2-1-5	A17	80'	17.14	4	45°
VS2-1-6	A17	80'	17.14	4	50°
VS2-1-7	A17	80'	17.14	4	55°
VS2-1-8	A17	80'	17.14	4	60°
VS2-1-9	A17	80'	17.14	4	63°
VS2-2-1	A17	80'	17.14	8	0°
VS2-2-2	A17	80'	17.14	8	13°
VS2-2-3	A17	80'	17.14	8	25°
VS2-2-4	A17	80'	17.14	8	35°
VS2-2-5	A17	80'	17.14	8	45°
VS2-2-6	A17	80'	17.14	8	50°
VS2-2-7	A17	80'	17.14	8	55°
VS2-2-8	A17	80'	17.14	8	60°
VS2-2-9	A17	80'	17.14	8	63°
VS2-3-1	A22	80'	21.82	8	0°
VS2-3-2	A22	80'	21.82	8	13°
VS2-3-3	A22	80'	21.82	8	25°
VS2-3-4	A22	80'	21.82	8	35°
VS2-3-5	A22	80'	21.82	8	45°
VS2-3-6	A22	80'	21.82	8	50°
VS2-3-7	A22	80'	21.82	8	55°
VS2-3-8	A22	80'	21.82	8	60°

Model ID	Section ID	Span Length	Span to Depth Ratio	Number of Girders	Skew Angle
VS2-3-9	A22	80'	21.82	8	63°
VS2-4-1	B21	100'	21.43	8	0°
VS2-4-2	B21	100'	21.43	8	13°
VS2-4-3	B21	100'	21.43	8	25°
VS2-4-4	B21	100'	21.43	8	35°
VS2-4-5	B21	100'	21.43	8	45°
VS2-4-6	B21	100'	21.43	8	50°
VS2-4-7	B21	100'	21.43	8	55°
VS2-4-8	B21	100'	21.43	8	60°
VS2-4-9	B21	100'	21.43	8	63°
VS2-5-1	C20	120'	20.00	8	0°
VS2-5-2	C20	120'	20.00	8	13°
VS2-5-3	C20	120'	20.00	8	25°
VS2-5-4	C20	120'	20.00	8	35°
VS2-5-5	C20	120'	20.00	8	45°
VS2-5-6	C20	120'	20.00	8	50°
VS2-5-7	C20	120'	20.00	8	55°
VS2-5-8	C20	120'	20.00	8	60°
VS2-5-9	C20	120'	20.00	8	63°
VS3-1-1	A17	80'	17.14	6	0°
VS3-1-2	A17	80'	17.14	10	0°
VS3-2-1	A17	80'	17.14	6	25°
VS3-2-2	A17	80'	17.14	10	25°
VS3-3-1	A17	80'	17.14	6	45°
VS3-3-2	A17	80'	17.14	10	45°
VS3-4-1	A22	80'	21.82	10	0°
VS3-5-1	C20	120'	20.00	4	0°
VS3-5-2	C20	120'	20.00	6	0°

Model ID	Section ID	Span Length	Span to Depth Ratio	Number of Girders	Skew Angle
VS3-5-3	C20	120'	20.00	10	0°
VS4-1-1	A24	80'	24.00	8	0°
VS4-2-1	A24	80'	24.00	8	45°
VS4-3-1	C17	120'	17.14	4	0°
VS4-3-2	C23	120'	22.50	4	0°
VS4-3-3	C26	120'	25.71	4	0°
VS4-4-1	C17	120'	17.14	8	0°
VS4-4-2	C23	120'	22.50	8	0°
VS4-4-3	C26	120'	25.71	8	0°
VS4-5-1	C17	120'	17.14	8	45°
VS4-5-2	C23	120'	22.50	8	45°
VS4-5-3	C26	120'	25.71	8	45°
FSA-1-1	A17	80'	17.14	10	63°
FSA-1-2	A17	80'	17.14	6	63°
FSA-1-3	A22	80'	21.82	10	13°
FSA-1-4	A22	80'	21.82	10	60°
FSA-1-5	A22	80'	21.82	6	13°
FSA-1-6	A22	80'	21.82	6	60°
FSA-2-1	B21	100'	21.43	10	13°
FSA-2-2	B21	100'	21.43	10	25°
FSA-2-3	B21	100'	21.43	10	45°
FSA-2-4	B21	100'	21.43	10	60°
FSA-2-5	B21	100'	21.43	4	25°
FSA-2-6	B21	100'	21.43	4	55°
FSA-2-7	B21	100'	21.43	4	63°
FSA-2-8	B21	100'	21.43	6	13°
FSA-2-9	B21	100'	21.43	6	25°
FSA-2-10	B21	100'	21.43	6	60°

Model ID	Section ID	Span Length	Span to Depth Ratio	Number of Girders	Skew Angle
FSA-2-11	B21	100'	21.43	6	63°
FSA-3-1	C18	120'	18.00	10	45°
FSA-3-2	C18	120'	18.00	4	55°
FSA-3-3	C18	120'	18.00	6	55°
FSA-3-4	C18	120'	18.00	8	0°
FSA-3-5	C18	120'	18.00	8	25°
FSA-3-6	C18	120'	18.00	8	45°
FSA-3-7	C18	120'	18.00	8	55°
FSA-3-8	C18	120'	18.00	8	63°
FSA-3-9	C21	120'	21.18	10	60°
FSA-3-10	C21	120'	21.18	10	63°
FSA-3-11	C21	120'	21.18	4	60°
FSA-3-12	C21	120'	21.18	4	63°
FSA-3-13	C21	120'	21.18	6	60°
FSA-3-14	C21	120'	21.18	6	63°

APPENDIX C

Concrete Bridge Model Geometric Parameters

Model ID	Section ID	Span Length	Span to Depth Ratio	Number of Girders	Skew Angle
CS1-1-1	AASHTO III	60'	13.58	6	0°
CS1-1-2	AASHTO III	60'	13.58	6	25°
CS1-1-3	AASHTO III	60'	13.58	6	45°
CS1-1-4	AASHTO III	60'	13.58	6	55°
CS1-1-5	AASHTO III	60'	13.58	6	63°
CS2-1-1	AASHTO IV	80'	15.48	4	0°
CS2-1-2	AASHTO IV	80'	15.48	4	25°
CS2-1-3	AASHTO IV	80'	15.48	4	45°
CS2-1-4	AASHTO IV	80'	15.48	4	55°
CS2-1-5	AASHTO IV	80'	15.48	4	63°
CS2-2-1	AASHTO IV	80'	15.48	6	0°
CS2-2-2	AASHTO IV	80'	15.48	6	25°
CS2-2-3	AASHTO IV	80'	15.48	6	45°
CS2-2-4	AASHTO IV	80'	15.48	6	55°
CS2-2-5	AASHTO IV	80'	15.48	6	63°
CS2-3-1	AASHTO IV	80'	15.48	8	0°
CS2-3-2	AASHTO IV	80'	15.48	8	25°
CS2-3-3	AASHTO IV	80'	15.48	8	45°
CS2-3-4	AASHTO IV	80'	15.48	8	55°
CS2-3-5	AASHTO IV	80'	15.48	8	63°

APPENDIX D1

Regression Example: Bearing Displacements Under Traditional Constraint Case

		REGRESSION		
Dependent Variable:	u			
		Parameter	Standard	T for H0:
Variable	Mean	Estimate	Error	parameter=0
Intercept		0.04	0.02	1.99
L	105.13	0.01	0.00	33.27
tan(gam)	0.80	-0.02	0.01	-1.73
W	664.96	-0.00	0.00	-0.35 x
Ltan(gam)	81.60	0.00	0.00	5.59
LW	68547.01	0.00	0.00	1.22 x
Wtan(gam)	549.74	0.00	0.00	12.81
		Sum of	Mean	
Source	DF	Squares	Square	F-Value
Model	6.00	2.61	0.43	2523.79
Error	110.00	0.02	0.00	
Total	116.00	2.63		
Dependent Mean	0.67			
Root Mean Sq Error	0.01			
Coefficient of Variation	1.95			
R-Square	0.99			
Adjusted R-Square	0.99			
		REGRESSION		
Dependent Variable:	u			
		Parameter	Standard	T for H0:

Variable	Mean	Estimate	Error	parameter=0
Intercept		0.04	0.01	5.05
L	105.13	0.01	0.00	76.14
tan(gam)	0.80	-0.04	0.01	-3.61 x
Ltan(gam)	81.60	0.00	0.00	6.23
Wtan(gam)	549.74	0.00	0.00	22.60
		Sum of	Mean	
Source	DF	Squares	Square	F-Value
Model	4.00	2.61	0.65	3626.34
Error	112.00	0.02	0.00	
Total	116.00	2.63		
Dependent Mean	0.67			
Root Mean Sq Error	0.01			
Coefficient of Variation	1.99			
R-Square	0.99			
Adjusted R-Square	0.99			
		REGRESSION		
Dependent Variable:	u			
		Parameter	Standard	T for H0:
Variable	Mean	Estimate	Error	parameter=0
Intercept		0.02	0.01	3.40
L	105.13	0.01	0.00	94.57
Ltan(gam)	81.60	0.00	0.00	6.34 x
Wtan(gam)	549.74	0.00	0.00	22.29
		Sum of	Mean	
Source	DF	Squares	Square	F-Value
Model	3.00	2.60	0.87	4366.73
Error	113.00	0.02	0.00	
Total	116.00	2.63		
Dependent Mean	0.67			

Root Mean Sq Error	0.01			
Coefficient of Variation	2.09			
R-Square	0.99			
Adjusted R-Square	0.99			
		REGRESSION		
Dependent Variable:	u			
		Parameter	Standard	T for H0:
Variable	Mean	Estimate	Error	parameter=0
Intercept		0.01	0.01	1.36
L	105.13	0.01	0.00	91.80
Wtan(gam)	549.74	0.00	0.00	51.59
		Sum of	Mean	
Source	DF	Squares	Square	F-Value
Model	2.00	2.60	1.30	4859.66
Error	114.00	0.03	0.00	
Total	116.00	2.63		
Dependent Mean	0.67			
Root Mean Sq Error	0.02			
Coefficient of Variation	2.43			
R-Square	0.99			
Adjusted R-Square	0.99			

APPENDIX D2

Regression Example: Bearing Forces Under Traditional Constraint Case

		REGRESSION		
Dependent Variable:	F			
		Parameter	Standard	T for H0:
Variable	Mean	Estimate	Error	parameter=0
Intercept		-7.31	27.12	-0.27
(1/L)	0.01	3660.18	2004.18	1.83
psi	21.04	-0.50	0.29	-1.71 x
W	696.30	-0.05	0.03	-1.90
(L/D)	20.10	0.48	1.16	0.42 x
(1/L)psi	0.22	-68.12	12.35	-5.52
(1/L)W	7.29	2.75	1.11	2.47
(1/L)(L/D)	0.21	-147.93	91.63	-1.61 x
psiW	14822.95	0.00	0.00	5.06
psi(L/D)	419.37	0.11	0.01	10.36
W(L/D)	14017.98	0.00	0.00	3.68
		Sum of	Mean	
Source	DF	Squares	Square	F-Value
Model	10.00	94946.75	9494.67	631.97
Error	97.00	1457.33	15.02	
Total	107.00	96404.08		
Dependent Mean	73.54			
Root Mean Sq Error	3.88			
Coefficient of Variation	5.27			
R-Square	0.98			
Adjusted R-Square	0.98			
		REGRESSION		

Dependent Variable:	F			
		Parameter	Standard	T for H0:
Variable	Mean	Estimate	Error	parameter=0
Intercept		-4.08	8.19	-0.50
(1/L)	0.01	1291.53	762.42	1.69 x
W	696.30	-0.02	0.01	-1.86 x
(1/L)psi	0.22	-77.89	9.43	-8.26
(1/L)W	7.29	2.26	1.01	2.23
psiW	14822.95	0.00	0.00	4.71
psi(L/D)	419.37	0.10	0.01	18.32
W(L/D)	14017.98	0.00	0.00	8.67
		Sum of	Mean	
Source	DF	Squares	Square	F-Value
Model	7.00	94848.63	13549.80	871.12
Error	100.00	1555.45	15.55	
Total	107.00	96404.08		
Dependent Mean	73.54			
Root Mean Sq Error	3.94			
Coefficient of Variation	5.36			
R-Square	0.98			
Adjusted R-Square	0.98			
		REGRESSION		
Dependent Variable:	F			
		Parameter	Standard	T for H0:
Variable	Mean	Estimate	Error	parameter=0
Intercept		3.43	1.93	1.77
(1/L)psi	0.22	-64.49	10.10	-6.38
(1/L)W	7.29	2.80	0.38	7.39
psiW	14822.95	0.00	0.00	1.99 x
psi(L/D)	419.37	0.10	0.01	17.50
W(L/D)	14017.98	0.00	0.00	6.24

		Sum of	Mean	
Source	DF	Squares	Square	F-Value
Model	5.00	94373.59	18874.72	948.16
Error	102.00	2030.49	19.91	
Total	107.00	96404.08		
Dependent Mean	73.54			
Root Mean Sq Error	4.46			
Coefficient of Variation	6.07			
R-Square	0.98			
Adjusted R-Square	0.98			
		REGRESSION		
Dependent Variable:	F			
		Parameter	Standard	T for H0:
Variable	Mean	Estimate	Error	parameter=0
Intercept		1.10	1.56	0.71
(1/L)psi	0.22	-60.11	10.00	-6.01
(1/L)W	7.29	2.87	0.38	7.49
psi(L/D)	419.37	0.10	0.01	19.91
W(L/D)	14017.98	0.00	0.00	7.10
		Sum of	Mean	
Source	DF	Squares	Square	F-Value
Model	4.00	94295.04	23573.76	1151.28
Error	103.00	2109.03	20.48	
Total	107.00	96404.08		
Dependent Mean	73.54			
Root Mean Sq Error	4.53			
Coefficient of Variation	6.15			
R-Square	0.98			
Adjusted R-Square	0.98			

******************** Higher-Order Terms Added ********************				
		REGRESSION		
Dependent Variable:	F			
		Parameter	Standard	T for H0:
Variable	Mean	Estimate	Error	parameter=0
Intercept		7.42	2.01	3.69
(1/L)psi	0.22	-56.99	22.70	-2.51 x
(1/L)W	7.29	3.02	0.36	8.30
psi(L/D)	419.37	0.06	0.01	5.01
W(L/D)	14017.98	0.00	0.00	4.57
psi(1/L)W	154.87	-0.07	0.03	-2.52
psi(1/L)(L/D)	4.37	2.93	0.91	3.23
psiW(L/D)	296294.73	0.00	0.00	3.77
		Sum of	Mean	
Source	DF	Squares	Square	F-Value
Model	7.00	94783.30	13540.47	835.43
Error	100.00	1620.78	16.21	
Total	107.00	96404.08		
Dependent Mean	73.54			
Root Mean Sq Error	4.03			
Coefficient of Variation	5.47			
R-Square	0.98			
Adjusted R-Square	0.98			
		REGRESSION		
Dependent Variable:	F			
		Parameter	Standard	T for H0:
Variable	Mean	Estimate	Error	parameter=0
Intercept		6.05	1.99	3.05
(1/L)W	7.29	3.04	0.37	8.14
psi(L/D)	419.37	0.04	0.01	4.25

W(L/D)	14017.98	0.00	0.00	4.87
psi(1/L)W	154.87	-0.13	0.02	-6.41
psi(1/L)(L/D)	4.37	1.84	0.82	2.25 x
psiW(L/D)	296294.73	0.00	0.00	7.16
		Sum of	Mean	
Source	DF	Squares	Square	F-Value
Model	6.00	94681.14	15780.19	925.05
Error	101.00	1722.94	17.06	
Total	107.00	96404.08		
Dependent Mean	73.54			
Root Mean Sq Error	4.13			
Coefficient of Variation	5.62			
R-Square	0.98			
Adjusted R-Square	0.98			
		REGRESSION		
Dependent Variable:	F			
		Parameter	Standard	T for H0:
Variable	Mean	Estimate	Error	parameter=0
Intercept		5.28	1.99	2.65
(1/L)W	7.29	3.06	0.38	8.04
psi(L/D)	419.37	0.06	0.00	15.17
W(L/D)	14017.98	0.00	0.00	5.00 x
psi(1/L)W	154.87	-0.10	0.01	-6.95
psiW(L/D)	296294.73	0.00	0.00	7.48
		Sum of	Mean	
Source	DF	Squares	Square	F-Value
Model	5.00	94594.58	18918.92	1066.44
Error	102.00	1809.50	17.74	
Total	107.00	96404.08		
Dependent Mean	73.54			
Root Mean Sq Error	4.21			

Coefficient of Variation	5.73			
R-Square	0.98			
Adjusted R-Square	0.98			
		REGRESSION		
Dependent Variable:	F			
		Parameter	Standard	T for H0:
Variable	Mean	Estimate	Error	parameter=0
Intercept		9.96	1.95	5.10
(1/L)W	7.29	4.56	0.26	17.65
psi(L/D)	419.37	0.05	0.00	12.90
psi(1/L)W	154.87	-0.14	0.01	-12.94
psiW(L/D)	296294.73	0.00	0.00	15.68
		Sum of	Mean	
Source	DF	Squares	Square	F-Value
Model	4.00	94151.69	23537.92	1076.37
Error	103.00	2252.38	21.87	
Total	107.00	96404.08		
Dependent Mean	73.54			
Root Mean Sq Error	4.68			
Coefficient of Variation	6.36			
R-Square	0.98			
Adjusted R-Square	0.98			